MASS ABLATION RATES AND THE ARGON SPECTROSCOPY OF LASER PRODUCED PLASMAS

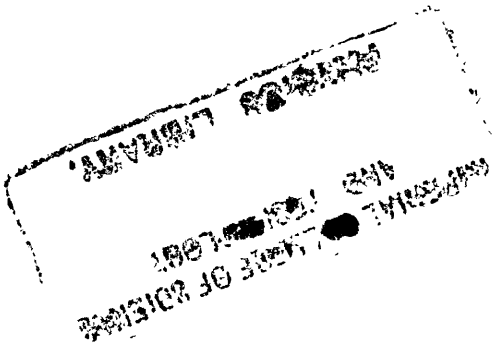
THESIS PRESENTED ON APPLICATION FOR THE DEGREE OF

DOCTOR OF PHILOSOPHY
AND
DIPLOMA OF IMPERIAL COLLEGE

BY

STEPHEN ALAN VEATS BSc

IMPERIAL COLLEGE OF SCIENCE AND TECHNOLOGY
LONDON SW7 2AZ.



ABSTRACT

The thesis contains work in two closely related areas of physics, the first describes the measurement of the mass ablation rate due to laser irradiation of a planar target and the second the spectroscopy of argon filled microballoons imploded using a laser.

The measurement of the mass ablation rate was carried out using time resolved X-ray spectroscopy and produced the first results at three laser wavelengths using a consistent method, for intensities from 10^{13} W cm^{-2} to 10^{15} W cm^{-2}.

These results are compared to those obtained by other methods of measurement and some theoretical models. Scalings of ablation pressure with laser intensity and wavelength are derived and show the advantage of using shorter laser wavelengths. The analysis indicates the limitations of using small laser spots due to edge effects.

The spectroscopy section covers the diagnosis of the core parameters of an imploded argon filled microballoon and details of the construction of a miniature X-ray crystal spectrometer used in the recording of the spectra.

Three methods of diagnosis using the argon spectra are employed: the measurement of the Stark broadening of a series of spectral lines, the ratio of the dielectronic satellites spectrally adjacent to the Ar XVIII 1s - 2p transition and a self consistent fit to the Ar XVII $1s^2$ - 1s2p and its intercombination line. A consistent fit is obtained.

The spectra have also been compared favourably with a collisional-radiative ionisation model pertaining to the imploded core.

FOR MY PARENTS

CONTENTS

		Page
TITLE PAGE		1
ABSTRACT		2
DEDICATION		3
CONTENTS		4
LIST OF TABLES		9
LIST OF FIGURES		10
CHAPTER 1	GENERAL INTRODUCTION TO LASER PRODUCED PLASMAS	13
1.1	INTRODUCTION	14
1.2	INERTIALLY CONFINED FUSION	14
1.3	LASERS IN LASER FUSION	16
1.4	PLASMA WAVES	18
1.4.1	DISPERSION RELATIONS	18
1.4.2	LANDAU DAMPING	20
1.4.3	PARTICLE TRAPPING	21
1.4.4	WAVE BREAKING	21
1.5	ABSORPTION PROCESSES	21
1.5.1	COLLISIONAL ABSORPTION	22
1.5.2	PARAMETRIC INSTABILITIES	23
1.5.3	RESONANT ABSORPTION	24
1.6	ENERGY TRANSPORT	26
1.6.1	THERMAL CONDUCTION BY ELECTRONS	26
1.6.2	HOT ELECTRONS	28
CHAPTER 2	PRESSURE IN INERTIAL FUSION TARGETS	30
2.1	INTRODUCTION	31
2.2	PLASMA PRESSURE	31

CONTENTS (Cont'd)

		Page
2.2.1	GENERAL HEAT WAVE MODEL	31
2.2.2	CHAPMAN JOUGUET DEFLAGRATION	33
2.2.3	SELF REGULATING ABLATION IN PLANE GEOMETRY	34
2.2.4	HEAT TRANSPORT TO SUPER-CRITICAL DENSITIES	36
2.2.5	HOT ELECTRON PREHEAT PRESSURE	37
2.3	SHOCK WAVES	39
2.4	EQUATIONS OF STATE	42
2.5	RAYLEIGH TAYLOR INSTABILITIES	44
2.6	THE THESIS WORK	45
CHAPTER 3	PREVIOUS EXPERIMENTAL WORK	46
3.1	INTRODUCTION	47
3.2	EXPLODING PUSHERS	47
3.2.1	THEORETICAL MODELS	47
3.2.2	EXPERIMENTAL OBSERVATIONS	48
3.3	ABLATIVE PUSHERS	50
3.3.1	SCALING OF ABLATIVE IMPLOSIONS WITH LASER PARAMETERS	50
3.3.2	METHODS OF ABLATION PRESSURE MEASUREMENT	52
3.3.2.1	RECOIL METHODS	52
3.3.2.2	FARADAY CUP MEASUREMENTS	53
3.3.2.3	SHOCK WAVE PROPAGATION	53
3.3.2.4	X-RAY SPECTROSCOPY	53
3.3.3	EXPERIMENTAL OBSERVATIONS	54
3.3.4	COMPILATION OF PREVIOUS RESULTS	55
CHAPTER 4	THE DETERMINATION OF MASS ABLATION RATE BY TIME RESOLVED X-RAY SPECTROSCOPY	57
4.1	INTRODUCTION	58
4.2	PRINCIPLE OF MEASUREMENT	59
4.3	EXPERIMENTAL DETAILS	62

CONTENTS (Cont'd)

		Page
4.3.1	LASER BEAM CHARACTERISTICS	62
4.3.2	TARGETS	65
4.3.3	DIAGNOSTICS	67
4.3.3.1	AREA MASS DENSITY	67
4.3.3.2	BURNTHROUGH TIME	67
4.3.3.3	LASER ENERGY	69
4.3.3.4	PULSE DURATION AND TIME HISTORY	69
4.3.3.5	FOCAL SPOT SIZE	69
4.3.3.6	TIME INTEGRATED SPECTROSCOPY	71
4.3.3.7	FARADAY CUPS	71
CHAPTER 5	MASS ABLATION RATES: RESULTS AND DISCUSSIONS	73
5.1	INTRODUCTION	74
5.2	BRIEF HISTORY OF EXPERIMENTS	74
5.3	MEASUREMENT ANALYSIS	78
5.3.1	TARGETS	78
5.3.2	LASER ENERGY	78
5.3.3	SPOT SIZE	78
5.3.4	BURN DELAY	83
5.3.5	CORRECTION FACTOR	84
5.4	DISCUSSION	87
5.4.1	LATERAL ENERGY TRANSPORT	89
5.4.2	EXPERIMENTAL REPRESENTATION	95
5.4.3	PRESSURE MEASUREMENT	99
5.5	WAVELENGTH SCALING	102
5.6	CONCLUSIONS	106
CHAPTER 6	PLASMA SPECTROSCOPY	107
6.1	INTRODUCTION	108
6.2	EMISSION AND ABSORPTION PROCESSES	108
6.3	IONISATION MODELS	108
6.3.1	LOCAL THERMODYNAMIC EQUILIBRIUM	109
6.3.2	CORONAL EQUILIBRIUM	110
6.3.3	COLLISIONAL RADIATIVE REGION	111

CONTENTS (Cont'd)

		Page
6.4	LINE INTENSITIES	112
6.5	ENVIRONMENTAL EFFECTS	113
6.5.1	DOPPLER BROADENING	114
6.5.2	STARK BROADENING	114
6.5.3	RADIATIVE TRANSFER	114
CHAPTER 7	THE DESIGN OF THE Mk.IV MINIATURE X-RAY SPECTROMETER	117
7.1	INTRODUCTION	118
7.2	DIAGNOSTIC DEVELOPMENT	118
7.3	BRAGG REFLECTION	118
7.4	TYPES OF SPECTROMETERS	119
7.5	THE FLAT CRYSTAL SPECTROMETER	119
7.6	THE Mk.IV MINIATURE X-RAY SPECTROMETER	121
7.7	FILM	127
7.8	PROBLEMS OF THE Mk.IV SPECTROMETER IN USE	128
CHAPTER 8	EXPERIMENTAL DETERMINATION OF PLASMA PARAMETERS USING ARGON SPECTRA	129
8.1	INTRODUCTION	130
8.2	EXPERIMENTAL METHOD	130
8.2.1	X-RAY PINHOLE CAMERA	132
8.2.2	MINIATURE X-RAY CRYSTAL SPECTROMETER	133
8.2.3	METHODS OF ANALYSIS	134
8.2.3.1	THEORETICAL LINE PROFILES	134
8.2.3.2	EXPERIMENTAL PROFILES	135
8.2,3.3	FITTING ROUTINE	136
8.3	RESULTS	139
8.3.1	INTRODUCTION	139
8.3.2	ANALYSIS	139
8.3.2.1	SELF-CONSISTENT FIT TO A SERIES	140

CONTENTS (Cont'd)

		Page
8.3.2.2	SELF-CONSISTENT FIT TO Ar XVII $1s^2$-1s2p GROUP	143
8.3.2.3	DIELECTRONIC SATELLITE RATIO	144
8.4	COMPARISON WITH IONISATION MODEL	147
8.5	CONCLUSIONS	148
REFERENCES		149
ACKNOWLEDGEMENTS		160

LIST OF TABLES

Table	Title	Page
5-1	1.05 μm MASS ABLATION RATE: EXPERIMENTAL DATA	75
5-2	0.53 μm MASS ABLATION RATE: EXPERIMENTAL DATA	76
5-3	0.35 μm MASS ABLATION RATE: EXPERIMENTAL DATA	77
5-4	PARAMETERS I_o, ϕ_o WHEN LATERAL ENERGY TRANSPORT IS NEGLIGIBLE. THE EXPONENT (x + 2y - 1) SHOWS INCREASING ENERGY INTO LATERAL TRANSPORT FOR $\phi < \phi_o$ OR $I > I_o$	93
5-5	PROPORTIONALITY CONSTANTS n_x AND v_x ASSUMING SCALING SIMILAR TO THE SPHERICAL ABLATION EXPERIMENTS (112)	96
5-6	ABLATION PARAMETERS AT $I_a = 10^{15}$ W cm^{-2}	98
5-7	ABLATION PRESSURE DEFINED BY K AND Z FOR THE LIMITING CASES (SEE TEXT)	100
5-8	ABLATION PRESSURE (Mb) CALCULATED FROM TABLE 5-7 AND FIG. 5.9 FOR VALUES $I = 10^{14}$ W cm^{-2} AND $I\lambda^2 = 10^{14}$ W cm^{-2} μm^2	102
7-1	SPECTROMETER SPECIFICATIONS	125
7-2	DEVELOPING TIMES IN KODAK DX 80	128

LIST OF FIGURES

Fig.	Title	Page
1.1	STRUCTURE OF A LASER PRODUCED PLASMA FOR 1 μm RADIATION (24)	17
1.2	THE MECHANISM OF RESONANT ABSORPTION (33)	25
2.1	A DISCONTINUOUS WAVE FRONT. THE EQUATION OF STATE HOLDS FOR BOTH SIDES WHICH ARE CONNECTED BY THE CONSERVATION EQUATIONS	32
2.2	THE SHOCK HUGONIOT (SEE TEXT)	41
3.1	DENSITY OBSERVATIONS IN EXPLODING PUSHER TARGETS (24)	50
3.2	ABLATION PRESSURE OBSERVATIONS WITH SIMPLE ANALYTIC MODELS (EQUATION NUMBERS IN BRACKETS) (24)	55
4.1	METHOD OF BURN-TIME MEASUREMENT SHOWING THE DELAY OF THE SILICON EMISSION WITH RESPECT TO THE ALUMINIUM EMISSION	59
4.2	SCHEMATIC DIAGRAM OF THE PLANE TARGET MASS ABLATION RATE EXPERIMENT	60
4.3	1.05 μm NEAR FIELD SPATIAL BEAM PROFILE	63
4.4	0.35 μm NEAR FIELD SPATIAL BEAM PROFILE	65
4.5	TYPICAL STREAK OF A SILICON MONOXIDE ON ALUMINIUM TARGET (THE Si XIII $1s^2$-1s2p IS COINCIDENT WITH THE Al XII $1s^2$-1s3p)	66
4.6	TYPICAL STREAK OF AN ALUMINIUM ON GLASS TARGET	68
4.7	OPTICAL MULTI-CHANNEL ANALYSER PICTURE OF THE 1.05 μm LASER PULSE	70
4.8	FARADAY CUP SIGNAL	72
5.1	1.05 μm X-RAY PINHOLE PICTURES (a) TIGHT FOCUS (b) 200 μm DIAMETER	79
5.2	0.53 μm X-RAY PINHOLE PICTURES (a) TIGHT FOCUS (b) 200 μm DIAMETER	80
5.3	0.35 μm X-RAY PINHOLE PICTURES (a) TIGHT FOCUS (b) 200 μm DIAMETER	81
5.4	1.05 μm; LENS DEFOCUS AGAINST MEASURED PINHOLE PICTURE SIZE	82
5.5	0.53 μm; LENS DEFOCUS AGAINST MEASURED PINHOLE PICTURE SIZE	83
5.6	COMPARISON OF THE X-RAY CONTINUUM AND LASER PULSE TIME PROFILES	85
5.7	LASER PULSE SHAPES AND TRAPEZOIDAL FITS (a) 1.05 μm (b) 0.53 μm (c) 0.35 μm	86

LIST OF FIGURES (Cont'd)

Fig.	Title	Page
5.8	CALCULATED CORRECTION FACTOR AGAINST BURN TIME	86
5.9	ABSORPTION FRACTION AGAINST INCIDENT IRRADIANCE FOR THE THREE LASER WAVELENGTHS	87
5.10	MASS ABLATION RATES AGAINST INCIDENT IRRADIANCE FOR THE THREE LASER WAVELENGTHS	88
5.11	MASS ABLATION RATES AGAINST ABSORBED IRRADIANCE FOR THE THREE LASER WAVELENGTHS	89
5.12	ION VELOCITY (AT THE PEAK OF THE DISTRIBUTION) AGAINST ABSORBED IRRADIANCE (a) 1.05 μm (b) 0.53 μm (c) 0.35 μm	90
5.13	RELATIVE MASS AGAINST ABSORBED IRRADIANCE (a) 1.05 μm (b) 0.53 μm (c) 0.35 μm	91
5.14	REPRESENTATION OF PLANAR ABLATION WITH FOCAL SPOT AND OUTER ANNULUS	95
5.15	1.05 μm ABLATION PRESSURE RESULTS (1) PRESENT RESULTS (2) ION EMISSION AND RECOIL MOMENTUM MEASUREMENTS (SEE FIG. 3.2)..	103
5.16	0.53 μm ABLATION PRESSURE RESULTS (1) PRESENT RESULTS (2) SPHERICAL PRESSURE MEASUREMENTS (14)	104
5.17	0.35 μm ABLATION PRESSURE RESULTS (1) PRESENT RESULTS (2) $P_{\infty \ell}$ INFERRED FROM MASS ABLATION DATA (116)	105
6.1	COLLISIONAL RADIATIVE EQUILIBRIUM FOR SILICON AT T_e = 540 eV	112
7.1	SCHEMATIC OF A FLAT CRYSTAL SPECTROMETER	120
7.2	SCHEMATIC OF A SPACE RESOLVING SPECTROMETER	121
7.3	ELEVATION OF THE RUTHERFORD SIX BEAM TARGET CHAMBER	122
7.4	LASER BEAM PROFILES IN THE SPECTROMETER PLANE (AXIS UNITS ARE THE DISTANCE FROM THE PLASMA TO THE PLANE)	123
7.5	Mk.I MINIATURE X-RAY CRYSTAL SPECTROMETER	124
7.6	Mk.IV MINIATURE X-RAY CRYSTAL SPECTROMETER	124
7.7	TYPICAL SPECTRA FROM THE Mk.IV SPECTROMETER	126
7.8	CHARACTERISTIC EXPOSURE CURVES FOR KODIREX (102) AND INDUSTREX C	127

LIST OF FIGURES (Cont'd)

Fig.	Title	Page
8.1	RELATIVE BEAM DIRECTIONS IN THE RUTHERFORD SIX BEAM TARGET CHAMBER	131
8.2	FOCUSING OF THE LASER BEAMS; 1 TARGET DIAMETER BEYOND THE TARGET CENTRE	131
8.3	PINHOLE PHOTOGRAPH AND DENSITOMETER TRACING OF AN IMPLODED ARGON-FILLED GLASS MICROBALLOON	132
8.4	EMISSION SPECTRUM OF A SIX BEAM IMPLOSION OF AN ARGON-FILLED GLASS MICROBALLOON	133
8.5	THEORETICAL STARK BROADENED LINE PROFILE OF AN AN Ar XVIII 1s-2p TRANSITION	135
8.6	IDEALISED LINES OF BEST FIT FOR SEVERAL SPECTRAL LINES FROM THE SAME SERIES IN n_e, n_1 PARAMETER SPACE	138
8.7	A TYPICAL BEST FIT FOR THE Ar XVII $1s^2$-1s3p TRANSITION	141
8.8	LINES OF BEST FIT IN n_e, n_1 PARAMETER SPACE FOR SHOT 131	142
8.9	DIAGNOSIS OF THE Ar XVII 1^1S_0-2^1P_1, 1^1S_0-2^3P_1 AND 1^1S_0-2^1S_0 BLEND IN SHOT 131	145
8.10	DENSITOMETER TRACE OF THE Ar XVIII 1s-2p RESONANCE LINE AND SATELLITES	146
8.11	INTENSITY RATIO OF THE TRIPLET TO SINGLET DIELECTRONIC SATELLITES SPECTRALLY ADJACENT TO THE Ar XVIII 1s-2p TRANSITION (153) (a) WITHOUT INNER SHELL EXCITATION (b) WITH INNER SHELL EXCITATION (N_M/N_H = 0.25). THE MEASURED EXPERIMENTAL VALUE FROM SHOT 131 IS ALSO INDICATED.	147

CHAPTER ONE

GENERAL INTRODUCTION TO LASER PRODUCED PLASMAS

		Page
1.1	INTRODUCTION	14
1.2	INERTIALLY CONFINED FUSION	14
1.3	LASERS IN LASER FUSION	16
1.4	PLASMA WAVES	18
1.4.1	DISPERSION RELATIONS	18
1.4.2	LANDAU DAMPING	20
1.4.3	PARTICLE TRAPPING	21
1.4.4	WAVE BREAKING	21
1.5	ABSORPTION PROCESSES	21
1.5.1	COLLISIONAL ABSORPTION	22
1.5.2	PARAMETRIC INSTABILITIES	23
1.5.3	RESONANT ABSORPTION	24
1.6	ENERGY TRANSPORT	26
1.6.1	THERMAL CONDUCTION BY ELECTRONS	26
1.6.2	HOT ELECTRONS	28

1.1 INTRODUCTION

With the advent of the laser in 1958 (1) came the realisation that this device could be used to heat small amounts of matter to temperatures where fusion reactions (2,3) might be significant. It was further proposed that for a suitable laser-target system nuclear fusion might be possible as an economic power source (4,5,6). A lot of effort has been spent in this direction enabling the technology of high power pulsed lasers to develop dramatically. This in turn has lead to a greater understanding of the plasma processes involved and more reproducible conditions at higher densities and temperatures.

These laser produced plasmas have also benefited other branches of physics such as spectroscopy by providing intense sources of soft X-rays of short duration and small source size (7,8,9,10) and can be used for the study of highly stripped atoms (11). Attempts have been made to use the laser produced plasma as a medium for an X-ray laser (12,13,14). Laser fusion can also produce a pulsed neutron source (7).

1.2 INERTIALLY CONFINED FUSION (ICF)

The criteria for a breakeven thermonuclear burn was given by Lawson (15) as

$$n\,\tau \sim 10^{14}\ \mathrm{cm^{-3}\ s} \qquad 1.1$$

where

n - the particle density

τ - the confinement time.

In magnetically confined plasmas the containment time is maximised by holding a pressure balance using a magnetic container or self induced magnetic fields utilising currents in the plasma to achieve a pinch effect (16). For a brief history

of magnetic confinement see reference 17. An alternative to magnetic confinement is inertial confinement where the plasma containment time is determined by its inertia. The characteristic expansion speed is the sound speed, C_A, so a sphere (radius, r_p) decreases its density by half in

$$\tau = \frac{r_p}{4C_A} \qquad 1.2$$

The burn rate during this time is determined by the fusion cross section (in this case for a deuterium-tritium (DT) interaction) times the particle velocity averaged over velocity space $< \sigma v >$ so the fraction consumed, ϕ, is

$$n_D \phi = n_D n_T < \sigma v > \frac{r_p}{4C_A} \qquad 1.3$$

where:

n_D - the particle density of deuterium

n_T - the particle density of tritium

but $\frac{< \sigma v >}{C_A}$ is approximately constant in the 10-50 kev temperature range (18) and this expression reduces to

$$\phi \sim \frac{\rho r_p}{6 + \rho r_p} \qquad 1.4$$

where ρ is the mass density (units are c.g.s). The parameter ρr_p is the equivalent in inertial confinement of the Lawson parameter $n\tau$ as the confinement time is proportional to the pellet radius (Equation 1.2). For a ϕ of 30% $\rho r_p \sim 3$ gm cm^{-2}. Increased yields can be obtained by propagation of the fusion burn front away from the central ignition region if the ρr_p product is greater than about 0.3 gm cm^{-2} (18).

A manageable explosion e.g. ~100 MJ can be obtained from about 0.3 mg of DT requiring a density in an inertial configuration of ~300 gm/cm^3 with a ρr_p of 3 gm/cm^2 (30% burn fraction). For more practicable smaller targets densities of the order of 10^3 gm/cm^3 will be required with pressures of the order of 10^3 Mbar.

Recent work (unpublished) from the Lawrence Livermore Laboratory on unspecified targets with a 0.6 ns 7 kJ laser pulse from Shiva achieved a ρr_p value of 4×10^{-2} gm cm^{-2}, a factor of 100 down on the value required for a 30% burn efficiency.

1.3 LASERS IN LASER FUSION

The pulsed laser in these experiments is used as a method of obtaining a high grade energy source from low grade electrical energy at efficiencies of ~0.1% (19) and power levels of the order of 10^{12} W (19). It provides a driver which can be readily modified to suit experimental requirements for beam intensity, polarization, pulse length and shape, and to some extent wavelength.

Glass lasers specific for plasma and fusion applications began to be developed in the late 1960s and with the introduction of such techniques as Q-switching (20) (1961) and later mode locking (21) (1964) enabled short pulse lengths and high power to be obtained.

The details of laser operations are given in several books and papers (e.g. 22,23) and will not be gone into here. More details of the laser beams used for the work will be given in the relevant experimental chapters (4 and 8).

When a laser is focussed to give high irradiance then a dense plasma is formed very quickly due to the large electric fields ~10^7 Vm^{-1} (inherent in the electromagnetic waves) stripping electrons from the atoms within a few oscillations of

the field. The rapid oscillation of these free electrons can also cause ionisation in a cascade process and a plasma of density greater than the critical density can be formed. The laser interaction with this plasma can then be via plasma waves. Figure 1.1 (24) shows, in a qualitative manner, the sort of temperature and density profiles which are established at the surface of a solid target.

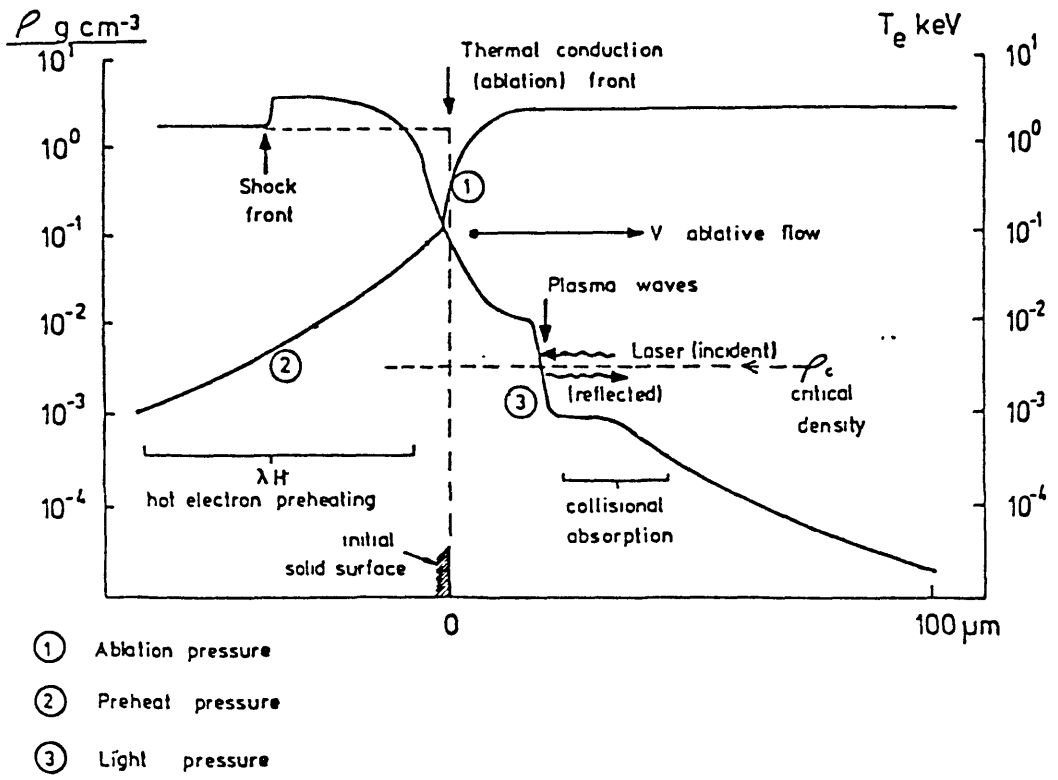


Fig. 1.1 STRUCTURE OF A LASER PRODUCED PLASMA FOR 1 μm IRRADIATION (24)

1.4 PLASMA WAVES

1.4.1 DISPERSION RELATIONS

For an electromagnetic wave varying as $\exp(\omega t - \underline{k} \cdot \underline{r})$ where:

ω - the angular frequency of the wave oscillations

t - the time

$\underline{k}$ - the wave propagation vector

$\underline{r}$ - the observation vector.

we get from Maxwells equations (25)

$$\underline{k} \times (\underline{k} \times \underline{E}) + \left(\frac{\omega}{c_L}\right)^2 \underline{\varepsilon} \cdot \underline{E} = 0 \qquad 1.5$$

where:

$\underline{E}$ - the electric field vector

c_L - the speed of light

ε - the dielectric constant (in general this is a tensor).

For transverse waves in a cold collisionless plasma (stationary ions) this reduces to

$$k^2 c_L^2 = \omega^2 - \omega_{pe}^2 \qquad 1.6$$

where:

$$\omega_{pe} = \left(\frac{n_e e^2}{m_e \varepsilon_o}\right)^{0.5} \qquad 1.7$$

is the electron plasma frequency with:

n_e - the electron density

m_e - the electron mass

ε_o - the permitivity of free space.

From the reduced dispersion relation (equation 1.6) propogation is only possible for

$$\omega > \omega_{pe} \tag{1.8}$$

In the situation of an increasing density gradient an incoming electromagnetic wave will be reflected when $\omega = \omega_{pe}$. For longitudinal waves in a cold plasma the only oscillation which are allowed are at the plasma frequency as

$$\underline{k} \times \underline{E} = 0 \tag{1.9}$$

so

$$\varepsilon = 0 \tag{1.10}$$

and the wave cannot propogate.

In a warm multi-species plasma the dielectric constant for electron plasma waves (Langmuir waves) (26) for high frequencies (i.e. ignoring ion contribution) is

$$\varepsilon(k,\omega) = 1 - \frac{\omega_{pe}^2}{\omega^2}\left[\left(1 + \frac{3}{2y_e^2}\right) - 2i\pi^{0.5}\ y_e^3\ \exp(-y_e^2)\right] \tag{1.11}$$

$\sqrt{2}\ y_e$ being the ratio between the phase velocity and thermal velocity of the electrons. The dispersion relation is given by equating expression 1.11 to zero. For large y_e, light damping, the imaginary part can be neglected and it gives

$$\omega = \omega_{pe}\ (1 + 3k^2\ \lambda_D^2)^{0.5} \tag{1.12}$$

where λ_D is the Debeye length

$$\lambda_D = \left(\frac{k_B T_e\ \varepsilon_0}{n_e\ e^2}\right)^{0.5} \tag{1.13}$$

where:

k_B - Boltzmann's constant

T_e - the electron temperature

e - the electron charge.

At lower frequencies the ion waves dominate. Defining the ion plasma frequency of

$$\omega_{pi}^2 = \frac{Zm_e}{m_i} \omega_{pe}^2 \qquad 1.14$$

The single ion species dispersion relation becomes

$$\omega_{ia}^2 = \frac{Z\, k_B\, T_e}{m_i} \quad \frac{k^2}{1 + k^2\, \lambda_D^2} \qquad 1.15$$

where:

ω_{ia} - the ion acoustic frequency

m_i - the ion mass.

This is essentially acoustic with a velocity

$$v_{ia} = \left(\frac{\gamma_e\, k_B\, T_e + \gamma_i\, k_B\, T_i}{m_i} \right)^{0.5} \qquad 1.16$$

where:

γ_e - the ratio of specific heats for the electrons

γ_i - the ratio of specific heats for the ions.

1.4.2 LANDAU DAMPING

The electron plasma waves are subject to Landau damping where particles travelling with a velocity slightly less than the phase velocity of the wave are accelerated and those of velocity higher than the wave phase velocity are decelerated by the waves electric field (27). If the velocity distribution is Maxwellian the wave will lose energy to the particles and so will be damped. If the slope of the particle velocity distribution is reversed (e.g. if there is a bump on the high energy tail) the wave may be amplified.

1.4.3 PARTICLE TRAPPING

For a large amplitude wave a particle travelling near the phase velocity may be trapped by the wave and carried along with it quivering at a velocity

$$v_e^2 = \frac{4eE_o}{m_e k} = 4\, v_E\, v_p \qquad 1.17$$

where:

E_o = the peak electric field

v_p = the phase velocity of the wave

$v_E = \frac{eE_o}{m_e \omega}$

is the maximum velocity obtained by the trapped electron quivering in the electric field of the wave. Very high energy particles can be produced in this way and can be a cause of target preheat.

The theory for this trapping, put forward by O'Neil (28) has been confirmed by computer simulations (29,30).

1.4.4 WAVE BREAKING

Another process for removing energy from large amplitude waves is wave breaking. This arises if the quiver velocity is greater than the phase velocity of the wave. The particles then became disordered and the wave is thus destroyed (31).

The importance of these effects depend on η, the ratio of quiver velocity to thermal velocity. For $\eta < 0.7$ Landau damping occurs, for $0.7 < \eta < 2$ to 5 trapping, and for $\eta > 6$ wave breaking.

1.5 ABSORPTION PROCESSES

There are three main types of absorption of the laser radiation by the plasma

a) collisional absorption

b) absorption by parametric instabilities, and

c) resonant absorption.

1.5.1 COLLISIONAL ABSORPTION

When an electron collides with an ion it is able to absorb a photon from the surrounding radiation field, this is known as linear inverse Bremsstrahlung and is an important process in the absorption of laser light in a plasma. The absorption coefficient (K_a) is (32)

$$K_a = \frac{\omega_{pe}^2}{c_L\ \omega\tau\ (\omega^2 - \omega_{pe}^2)^{0.5}}\ cm^{-1} \qquad 1.18$$

where τ is the electron-ion collision time

$$\tau = \frac{2.4 \times 10^4\ (k_B\ T_e)^{1.5}}{n_e Z}\ s \qquad 1.19$$

From Equation 1.18 the absorption is maximised near the critical density surface where $\omega \sim \omega_{pe}$ and T_e is low (see Fig. 1.1). For $k_B T_e \sim 500$ eV, $Z = 10$ and $\omega_e = \frac{\omega_{pe}}{2}$ the absorption length is about 25 μm. It can also be seen that the maximum absorption coefficient will be greater for shorter laser wavelength at at constant ω/ω_{pe} for the density is related to the plasma frequency by Equation 1.7 and gives the critical density as

$$n_{ec} = 10^{21}\ \lambda^{-2}\ cm^{-3} \qquad 1.20$$

where

λ is the laser wavelength in μm.

Collisional absorption is more effective for shallow density gradients and low irradiances due to the temperature dependence.

An estimate can be obtained of the amount of radiation absorbed by this process by integrating the absorption coefficient over the laser path length (z). For a linear density gradient in an isothermal plasma

$$I_R = I_o \exp\left(-2 \int_{n_e=0}^{n_e=n_{ec}} K_a(z)dz\right) \qquad 1.21$$

if $n_e = 0$ at $z = 0$ and $n_e = n_{ec}$ at $z = \ell$

$$I_R = I_o \exp -\frac{32}{15} \cdot \frac{\ell\, \upsilon(\ell)}{c} \qquad 1.22$$

where $\upsilon(\ell)$ is the collision frequency at $z = \ell$ and is given by

$$\upsilon_{ei} = 2 \times 10^{-5} \frac{n_e Z}{T_e^{1.5}} \qquad 1.23$$

(33) e.g. for $k_B T_e$ = 1000 eV, Z = 6, ℓ = 10 μm with a 1μm laser the reflected to incident intensity ratio (I_R/I_o) is 56% i.e. an absorption of 44%. For smaller scale lengths the absorption fraction drops e.g. for ℓ = 3 μm, I_R/I_o is 84%.

The theory of linear inverse Bremsstrahlung assumes that the radiation field does not perturb the electron velocity distribution. At high laser irradiances this is probably not valid as in these cases the electron motion is likely to be dominated by the radiation field rather than thermal (collision) processes.

1.5.2 PARAMETRIC INSTABILITIES

There are several processes (25,5) causing an electromagnetic wave to couple to other plasma modes stimulating their growth out of the noise. In the case of laser plasma interactions the main driver is the laser electromagnetic wave and the driven modes can be other transverse waves or longitudinal electron plasma or ion acoustic waves. There is also the possibility that some of these modes may themselves act as drivers for other resonances.

The main instabilities are:

$t \rightarrow e + i$	the parametric instability	(29)
$t \rightarrow t' + i$	stimulated Brillouin scattering	(34)

$t \rightarrow t' + e$ stimulated Raman scattering (34)

$t \rightarrow e + e$ the two plasmon instability (35)

where:

t and t' - electromagnetic waves

e - an electron plasma wave

i - an ion acoustic wave.

The first and fourth of these can absorb laser energy reasonably efficiently under certain conditions whilst the second and third can backscatter a large fraction of the driver power.

All these instabilities have threshold intensities for the driver below which the modes will not grow (25).

1.5.3 RESONANT ABSORPTION

Resonance absorption (36,37) occurs at high irradiances ($I\lambda^2 > 10^{15}$ W cm^{-2} μm^2) for light obliquely incident on a plasma density gradient with p polarization (i.e. E vector parallel to the plane of incidence). A linear plasma gradient refracts an electromagnetic wave which will follow a curved path reaching a turning point of

$$n_e = n_{ec} \cos^2 \theta \qquad 1.24$$

where

θ - the angle of incidence of the light beam (see Fig. 1.2).

The E field component normal to the target surface effectively tunnels into regions of higher density where it will be resonant with the plasma electrons and will drive large amplitude electron plasma waves. These will be damped by Landau damping and collisionless wave breaking and hence will produce a high energy

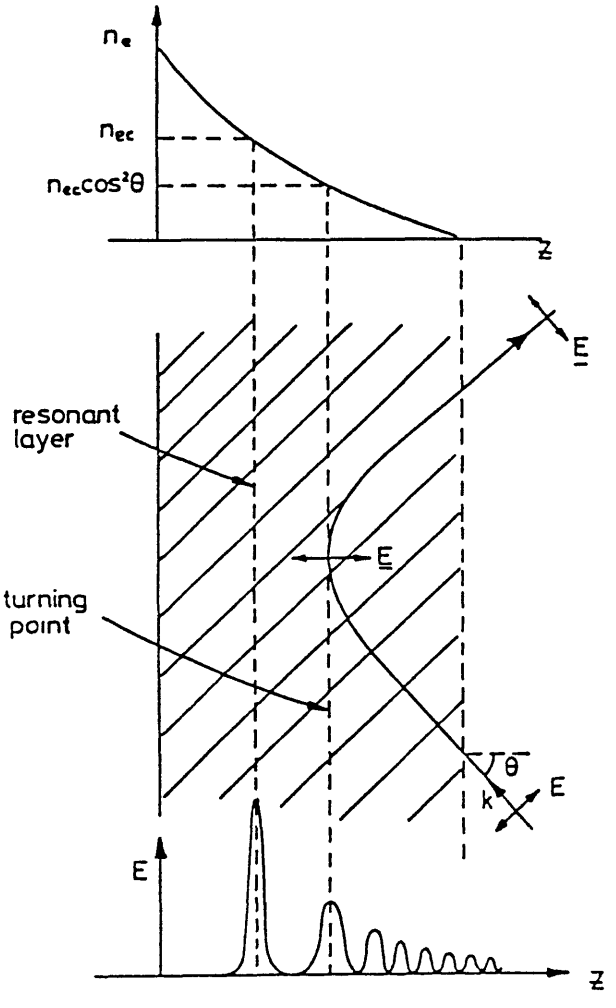


Fig. 1.2 THE MECHANISM OF RESONANT ABSORPTION (33)

component to the electron velocity distribution. These super-thermal electrons can have energies of about

$$< 0.5\ m_e\ v^2 > \ = \ E\ e\ \ell \qquad 1.25$$

and penetrate the target to large distances (~10 μm). A large fraction of the laser energy (as much as 50%) can be absorbed in this way. In the experiments described in this thesis the laser beam is focussed by a low f number lens and some of the rays are striking the target from an appreciable angle (especially on plane targets). For high $I\lambda^2$ values resonant absorption is important.

1.6 ENERGY TRANSPORT

1.6.1 THERMAL CONDUCTION BY ELECTRONS

Absorption of the laser light transfers energy principally to the electrons at sub-critical density. For the thermal electrons a diffusion process carries the energy to other parts of the system in particular to densities greater than critical.

In the case of a classical heat conduction model the heat flux is determined by

$$\rho\, C \frac{\partial T_e}{\partial t} = - \nabla \circ \underline{S} \qquad 1.26$$

and

$$\underline{S} = -K \nabla T_e \qquad 1.27$$

where:

ρ - the density

C - the specific heat

$\underline{S}$ - the heat flux function

K - the thermal conductivity calculated by Spitzer and Harm (38,39) as

$$K = \frac{20\left(\frac{2}{\pi}\right)^{0.5} (k_B T_e)^{2.5}\ k\ \delta\ \varepsilon}{m_e^{0.5}\ e^4\ Z\ \ln \Lambda} \text{ erg s}^{-1} \text{ deg}^{-1} \text{ cm} \qquad 1.28$$

the parameters $\ln \Lambda$, k, δ and ε are given by Spitzer (39). Combining 1.26 and 1.27

$$\frac{\partial T_e}{\partial t} = D_T \nabla^2 T_e \qquad 1.29$$

where

D_T - the coefficient of thermal diffusivity.

$$D_T = \frac{K}{\rho C} \propto T_e^{2.5}\ \rho^{-1} \qquad 1.30$$

This thermal diffusion leads to an almost constant temperature in the sub-critical region where the diffusivity is high with a steep thermal front in the super-critical plasma (see Fig. 1.1).

This classical diffusion of cold electrons is altered by the fact that the particles are charged. For a Maxwellian distribution the energy transport distribution function

$$S(v) = f(v_x, v_y, v_z)0.5\ m_e (v_x^2 + v_y^2 + v_z^2)\ v_x \qquad 1.31$$

is a maximum for particles with an energy of 3 kT_e. To maintain charge neutrality the flow of these hot electrons must be countered by a drift in the opposite direction of cooler electrons thus producing a distorted velocity distribution. This gives an effective heat conductivity of

$$K_{EFF} = \alpha K \qquad 1.32$$

where

α = 0.4 for a Lorentz gas.

For a plasma there is a correction factor of $\delta(T_e,Z)$ which is less than, but of the order of unity and has been tabulated by Spitzer (39).

The diffusion model as calculated by Spitzer will break down if $\frac{\lambda}{L} > 0.02$, where λ is the electron mean free path and L is the temperature gradient scale length (40).

The skewed velocity distribution will peak at a value of

$$v_D = 0.3\ V_{et} \frac{\lambda}{L} \qquad 1.33$$

the drift velocity of the return current. V_{et} is the electron thermal velocity. The phase velocity of the ion acoustic waves is

$$v_{ia} = \left(\frac{ZkT_e + kT_i}{m_i}\right)^{0.5} \qquad 1.34$$

but if $ZT_e >> T_i$, v_{ia} can be much greater than the mean ion thermal velocity so no appreciable Landau damping can occur and if $v_{ia} < v_D$ then the slope of the distribution function is negative and there will be unstable growth of ion acoustic waves giving rise to plasma turbulence. Using 1.33 and 1.34 the criteria for this if $ZT_e >> T_i$ is

$$\frac{\lambda}{L} > 3\left(\frac{m_e Z}{m_i}\right)^{0.5} \qquad 1.35$$

The growth of turbulence with an amplitude $\frac{\delta n}{n}$ causes increased electron scattering and hence inhibited conductivity by a factor (41).

$$R_T = 2 \times 10^{-3}\left(\frac{n}{\delta n}\right)^2 \qquad 1.36$$

Since this threshold is exceeded in typical laser plasmas this could be an important mechanism in inhibiting conductivity.

However the low numbers of particles in a Debeye sphere, and hence the large inter-particle scattering frequency, reduces the importance of turbulence in laser plasmas.

Conductivity can also be decreased by magnetic fields transverse to the heat flow by a factor

$$R_m = \frac{1}{(1+\omega^2\ \tau^2)} \qquad 1.37$$

where

ω - the electron gyrofrequency

τ - the electron - ion collision time.

1.6.2 HOT ELECTRONS

The diffusion model does not apply to 'hot' electrons as their mean free path is much greater than their diffusion scale length and they are able to penetrate tens of microns into the

solid material having energies of about three times the mean thermal energy. Deposition of the energy into the cold solid causes 'hot electron preheat' which is undesirable for efficient target compression (see Chapter 2).

Computational studies (42,43,36) show that for high enough $I\lambda^2$ values the X-ray spectrum shows a double Maxwellian structure and can be characterised by two temperatures, one for the thermal (cold) electrons, T_C, and one for the fast (hot) electrons, T_H.

The thermal emission occurs as part of the radiative recombination processes of the cold electrons whilst that produced by the hot electrons is due to Bremsstrahlung (see Chapter 6).

Other evidence for fast electron comes from the detection of fast ions accelerated in the electric field created by the fast electrons.

All of the various models proposed to describes the production of fast electron give a general scaling of $T_H \propto (I\lambda^2)^{\delta}$. The mechanism is probably wave breaking of the plasmons produced at critical density by resonant absorption (44). Reference 42 gives the hot electron temperature as

$$T_H = 14\ (I\lambda^2)^{0.33}\ T_C^{0.33}\ \text{keV} \qquad 1.38$$

It included self consistent steepening of the density gradient by the ponderomotive force (45) and showed absorption fraction of the laser energy of about 30% and giving the two temperature X-ray spectrum observed (46), these agree well with experimental results (e.g. 47).

The hot electrons have a mean free path of the order of 10's of microns and so can deposit a significant amount of energy ahead of the thermal and shock fronts preheating the target and reducing the efficiency of hydrodynamic processes (e.g. compression).

CHAPTER TWO

PRESSURE IN INERTIAL FUSION TARGETS

		Page
2.1	INTRODUCTION	31
2.2	PLASMA PRESSURE	31
2.2.1	GENERAL HEAT WAVE MODEL	31
2.2.2	CHAPMAN JOUGUET DEFLAGRATION	33
2.2.3	SELF REGULATING ABLATION IN PLANE GEOMETRY	34
2.2.4	HEAT TRANSPORT TO SUPERCRITICAL DENSITIES	36
2.2.5	HOT ELECTRON PREHEAT PRESSURE	37
2.3	SHOCK WAVES	39
2.4	EQUATIONS OF STATE	42
2.5	RAYLEIGH TAYLOR INSTABILITIES	44
2.6	THE THESIS WORK	45

2.1 INTRODUCTION

This chapter will largely deal with hydrodynamics in laser irradiated targets. There are three types of pressure to be considered:

a) light (radiation) pressure (see Chapter 1, Ref. 45)

b) ablation pressure, and

c) the hot electron preheat pressure.

The ablation pressure is the pressure driving the outward flow of the hot plasma. This will be greatest where the product of ρ and T_e is greatest and because this occurs at densities higher than n_{ec} it can be reduced by inhibition of thermal conduction. This pressure also drives a shock front into the solid material. The hot electron preheat pressure is exerted where the hot electrons deposit their energy in the cold dense target material and is the dominant pressure in 'exploding pusher' compressions.

2.2 PLASMA PRESSURE

Although analysis of the effects of these pressures generally requires the use of complex computer codes, it is useful to look at some simple analytic models which indicate the scaling of the pressures (in particular the ablation pressure and hot electron pressure) with parameters such as laser intensity, wavelength and target material.

2.2.1 GENERAL HEAT WAVE MODEL

A steady state ablation front can be viewed in the first instance as a discontinuity over which the equations of conservation of mass, momentum and energy can be applied. In the frame of reference of the front (see Fig. 2.1)

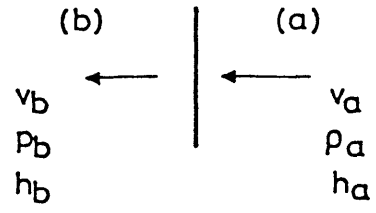


Fig. 2.1 A DISCONTINUOUS WAVE FRONT. THE EQUATION OF STATE HOLDS FOR BOTH SIDES WHICH ARE CONNECTED BY THE CONSERVATION EQUATIONS

$$\rho_a v_a = \rho_b v_b \qquad 2.1$$

$$P_a + \rho_a v_a^2 = P_b + \rho_b v_b^2 \qquad 2.2$$

$$0.5 v_a^2 + h_a + \frac{W}{\rho_a v_a} = 0.5 v_b^2 + h_b \qquad 2.3$$

where:

ρ - the density
v - the velocity relative to the front
P - the pressure
W - the laser power absorbed per unit area
h - the enthalpy
a - signifies the region ahead of the wave
b - the region behind it.

There are two 'fronts' to be considered, the ablation or burn front, the velocity of which can be obtained by equating enthalpy flux to the absorbed energy

$$v = \frac{W}{\rho_a h_b} \qquad 2.4$$

and the shock or acoustic front with a velocity given by:

$$v_s = \left(\frac{P_b}{\rho_a}\right)^{0.5} \qquad 2.5$$

In the case of ablation by laser irradiation there is a subsonic ablation (24) where $v_s > v$ so that the shock front propagates into the target ahead of the ablation front. The limiting case where $v_s = v$ is termed the Chapman Jouguet deflagration.

The effect of the shock wave travelling ahead of the burn wave is to produce a compressed region between the two. To link them we need to know an equation of state of the form

$$h = \left(\frac{\gamma}{\gamma-1}\right)\frac{P}{\rho} \qquad 2.6$$

where:

γ - the ratio of specific heats.

For a solution we need another equation relating the ablation parameters and the laser intensity, a 'heating' law containing the physics of the laser absorption.

2.2.2 CHAPMAN JOUGUET DEFLAGRATION

This was used by Fauquinon and Floux (48) to describe ablation from a plane target. The essential feature is that the flow behind the burn wave is sonic i.e.

$$v_b = \left(\frac{\gamma_b P_b}{\rho_b}\right)^{0.5} \qquad 2.7$$

and that the heating law is simplified by specifying that $\rho_b = \rho_c$, the critical density. So by combination with equations 2.1, 2.2 and 2.3 with the assumptions that

$$\gamma_a = \gamma_b \qquad 2.8$$

$$\rho_c << \rho_a \qquad 2.9$$

and $$h_a + 0.5\ v_a^2 << \frac{W}{\rho_a\ v_a} \qquad 2.10$$

we get

$$W = \frac{P_b^{1.5}}{\rho_c^{0.5}} \gamma^{0.5} \left(\frac{\gamma}{2} + \frac{\gamma}{\gamma-1}\right) \qquad 2.11$$

The laser power goes into increased kinetic energy and enthalpy. This gives for the specific mass ablation rate, $\dot{m}$, the velocity at a large distance from the plasma, v, and the pressure, P (48,24)

$$\dot{m} = 0.8 \times 10^5 (\lambda\ \mu m)^{-1.33} \left(\frac{I_a\ (W\ cm^{-2})}{10^{13}}\right)^{0.33} gm\ cm^{-2}\ s^{-1} \qquad 2.12$$

$$v = 4.1 \times 10^7 (\lambda\ \mu m)^{0.66} \left(\frac{I_a\ (W\ cm^{-2})}{10^{13}}\right)^{0.33} cm\ s^{-1} \qquad 2.13$$

$$P = 3.2 (\lambda\ \mu m)^{-0.66} \left(\frac{I_a\ (W\ cm^{-2})}{10^{13}}\right)^{0.66} M\ Bar \qquad 2.14$$

The temperature can be found by relating the specific enthalpy $(\frac{3}{2}\frac{kT}{m_p})$ to the pressure and density through the equation of state.

$$kT_b\ (kev) = 0.7 (\lambda\ \mu m)^{1.33} \left(\frac{I\ (W\ cm^{-2})}{10^{13}}\right)^{0.66} \qquad 2.15$$

This idealised model may not represent well situations when the subcritical absorption is high or low when energy transport is needed to conduct energy to the ablation front at densities well above critical density.

There are a number of variant models which give general agreement. Some of these are presented below.

2.2.3 SELF REGULATING ABLATION IN PLANE GEOMETRY

Where inverse Bremsstrahlung is the dominant absorption mechanism a useful device is that of self regulation where the flow of plasma from a surface regulates itself by varying the absorption of the incoming radiation (49). The scale length (ℓ) and absorption coefficient (K) satisfy a relationship of the kind (50)

$$K\ell \sim 1 \qquad 2.16$$

Applying this concept to plane ablation, time and intensity dependent pressure are produced (51,52)

$$\rho_b \sim I^{0.25}\ t^{-0.375} \qquad 2.17$$

$$T_b \sim I^{0.5}\ t^{0.25} \qquad 2.18$$

$$P_b \sim I^{0.75}\ t^{-0.125} \qquad 2.19$$

This leads to a pressure (53) acting on the solid

$$P_a = 1.3\ Z^{-0.563}\ A^{0.438}\ (\lambda\ \mu m)^{-0.25}\ (t_{ns})^{-0.125} \left(\frac{I_a\ (W\ cm^{-2})}{10^{13}}\right)^{0.75} \qquad 2.20$$

The time dependence arises from the assumption of planar flow which gives an increase in scale length with time. Other work (54,55) takes this into account by assuming spherical flow to give a fixed scale length. The resulting scaling laws are thus time independent

$$\rho_b \sim I^{0.33} \qquad 2.21$$

$$T_b \sim I^{0.44} \qquad 2.22$$

$$P_b \sim I^{0.778} \qquad 2.23$$

giving quantitative expressions (49,24) for the mass ablation rate, asymtopic velocity and pressure

$$\dot{m} = 0.53 \times 10^5\ (\lambda\ \mu m)^{-0.444} \left(\frac{ZL\ \mu m}{100}\right)^{-0.222} \left(\frac{I_a\ (W\ cm^{-2})}{10^{13}}\right)^{0.556}\ gm\ cm^{-2}\ s^{-1} \qquad 2.24$$

$$v = 3.6 \times 10^7\ (\lambda\ \mu m)^{0.222} \left(\frac{ZL\ \mu m}{100}\right)^{0.111} \left(\frac{I_a\ (W\ cm^{-2})}{10^{13}}\right)^{0.222}\ cm\ s^{-1} \qquad 2.25$$

$$P = 1.8\ (\lambda\ \mu m)^{-0.222} \left(\frac{ZL\ \mu m}{100}\right)^{-0.111} \left(\frac{I_a\ (W\ cm^{-2})}{10^{13}}\right)^{0.778}\ M\ bar \qquad 2.26$$

where L is the scale length (focal spot dimension or spherical target radius).

These models assume inverse Bremsstrahlung absorption and have ρ_b varying with I. They thus become invalid if ρ_b is greater than critical density, as is usual leading to an increased ablation pressure as the temperature is approximately constant.

2.2.4 HEAT TRANSPORT TO SUPERCRITICAL DENSITIES

A treatment of electron thermal conduction in spherical geometry has been formulated by Max, McKee and Mead (56) where the use of a flux limit (40), f, simplifies the equations. In this model the radius r_c at which $\rho = \rho_c$ is a function of I and λ so that the reference area where the simple equalities are evaluated is variable. If

$$I_a = \frac{W}{4\pi r^2} \qquad 2.27$$

where

W - the laser power

r - the radius for that absorbed intensity

and

$$\dot{m} = \frac{\dot{M}}{4\pi r^2} \qquad 2.28$$

where $\dot{M}$ is the total mass ablation rate from the target, then

$$\dot{m} = 0.77 \times 10^5 \, (\lambda\ \mu m)^{-0.82} \left(\frac{r\ \mu m}{100}\right)^{-0.11} \left(\frac{I_a\ (W\ cm^{-2})}{10^{13}}\right) gm\ cm^{-2}\ s^{-1} \qquad 2.29$$

$$v = 5.3 \times 10^7 \, (\lambda\ \mu m)^{0.41} \left(\frac{r\ \mu m}{100}\right)^{0.055} \left(\frac{I_a\ (W\ cm^{-2})}{10^{13}}\right)^{0.26} cm\ s^{-1} \qquad 2.30$$

$$P = 1.6 \, (\lambda\ \mu m)^{-0.99} \left(\frac{Zr\ \mu m}{100}\right)^{0.07} \left(\frac{I_a\ (W\ cm^{-2})}{10^{13}}\right)^{0.57} M\ Bar \qquad 2.31$$

for a value of f = 0.03

If the intensity and mass ablation rate are linked to the critical density surface at radius r_c

$$I_a = \frac{W}{4\pi r_c^2} \qquad 2.32$$

$$\dot{m} = \frac{\dot{M}}{4\pi r_c^2} \qquad 2.33$$

then the scaling relationship became

$$\dot{m} \propto \lambda^{-1.3}\ r^{0.01}\ I_a{}^{0.33} \qquad 2.34$$

$$v \propto \lambda^{0.66}\ r^{0.002}\ I_a{}^{0.33} \qquad 2.35$$

$$P \propto \lambda^{-0.43}\ r^{0.005}\ I_a{}^{0.73} \qquad 2.36$$

The scaling of $\dot{m}$ and v are characteristic of sonic density deflagration.

This type of model has the limitations of representing an energy dump at the critical density and so does not include absorption in the underdense region or hot electron preheat.

2.2.5 HOT ELECTRON PREHEAT PRESSURE

The range of hot electrons (kT_H ~ 10 keV at $I\lambda^2 \sim 10^{15}$ W cm^{-2} μm^2) can be of the order of 10 μm so a considerable amount of energy can be deposited in cold material at close to solid density. Compared with the thermal burn front the time taken to establish an ablative flow for hot electrons is much longer as the scale length is longer, the temperature of the heated material lower and the inertial response of the solid material much slower.

The energy deposition profile falls off with distance from the surface with an observed scale length λ_H of (47)

$$\lambda_H = \frac{3 \times 10^{-3}}{\rho_a} \left(\frac{I\ \lambda^2\ (W\ cm^{-2})\ \mu m^2}{2 \times 10^{15}} \right)^{0.8} cm \qquad 2.37$$

If about one half of the absorbed energy goes into hot electron preheat we get

$$P_H(t) = 230 \left(\frac{I_a\ (W\ cm^{-2})}{2 \times 10^{15}} \right)^{0.2} (\lambda\ \mu m)^{-1.6} \left(\frac{t_{ps}}{100} \right) M\ bar \qquad 2.38$$

Note that the pressure is time dependent but it will be limited by expansion or by removal of the heated layer by normal ablation which will occur in

$$t = \frac{\lambda_H}{v}$$

$$= 1.45 \times 10^{-8}\ (\lambda\ \mu m)^{2.6} \left(\frac{I_a\ (W\ cm^{-2})}{10^{16}} \right)^{0.47} s \qquad 2.39$$

This is generally long compared with the time taken for a hot electron self regulating system to be established. We can obtain this by equating the self regulating ablation pressure to the transient preheat pressure giving (24)

$$t = 2 \times 10^{-10} \left(\frac{r_c\ (\mu m)}{100} \right)^{-0.143} (\lambda\ \mu m)^{1.6} \left(\frac{I_a (W\ cm^{-2})}{10^{16}} \right)^{0.66} s \qquad 2.40$$

This is generally shorter than the cut off due to normal ablation. The ratio between these times will be greater than predicted as the energy going into normal ablation is lessened by the hot electron production so the burn velocity (v) is smaller. Thermal conduction inhibition will also reduce the burn depth.

A maximum pressure, limited by expansion, has been shown (31) by the analysis of the dynamic response of a uniformly heated sphere. Though a solution only exists for a sphere it can be approximated by assuming that the pressure saturates at a time t_e where

$$\int_o^{t_e} C(t)\, dt = \lambda_H \qquad 2.41$$

and C is the sound speed, and that the heat input to the material creates a pressure

$$P(t) = \frac{I\, t}{\lambda_H} \qquad 2.42$$

Then for preheating caused by one-quarter of the incident intensity (I)

$$P_H = 1100\, \rho_a^{0.33} \left(\frac{I\ (W\ cm^{-2})}{10^{16}}\right)^{0.66} M\ bar \qquad 2.43$$

and

$$t_e = 3.6 \times 10^{-10}\, \rho_a^{0.66} \left(\frac{I\ (W\ cm^{-2})}{10^{16}}\right)^{0.47} (\lambda\ \mu m)^{1.6}\ s \qquad 2.44$$

If this time is short compared with the pulse length, which will be true at low intensities, then there is no appreciable difference as far as the ablation processes are concerned, between the thermal and hot electrons.

2.3 SHOCK WAVES

With a sudden compression an acoustic disturbance is created which takes the form of a discontinuity, a shock wave. This is formed because the sound velocity is increased as the compression takes place so the peak of the wave till tend to

overtake the foot. In the opposite case of rarefaction the peak will tend to travel slower than the foot and the disturbance will spread out.

The shock wave can be described in a similar manner to the pressure wave (see Section 2.2 1) except that the power input is zero (Rankine Hugoniot solutions (57)).

As previously, the frame of reference will be taken as having a stationary wave front with an intake velocity v_a exhaust velocity v_b (see Fig. 2.1). In the lab frame the velocity of material behind the shock will just be

$$u_b = v_a - v_b \tag{2.45}$$

The pressure density relations (the shock Hugoniot) can be expressed as

$$\frac{P_b}{P_a} = \frac{\frac{(\gamma+1)}{\rho_a} - \frac{(\gamma-1)}{\rho_b}}{\frac{(\gamma+1)}{\rho_b} - \frac{(\gamma-1)}{\rho_a}} \tag{2.46}$$

where $\gamma_a = \gamma_b$, giving a compression ratio of

$$\frac{\rho_b}{\rho_a} = \frac{(\gamma+1)\ P_b + (\gamma-1)\ P_a}{(\gamma-1)\ P_b + (\gamma+1)\ P_a} \tag{2.47}$$

and the intake and exhaust velocities are

$$v_a^2 = \frac{1}{2\ \rho_a}\left[(\gamma+1)\ P_b + (\gamma-1)\ P_a\right] \tag{2.48}$$

$$v_b^2 = \frac{1}{2\ \rho_a}\frac{\left[(\gamma-1)\ P_b + (\gamma+1)\ P_a\right]^2}{(\gamma+1)\ P_b + (\gamma-1)\ P_a} \tag{2.49}$$

when $P_b >> P_a$ the strong shock limit is obtained and we get

$$\frac{\rho_b}{\rho_a} = \frac{(\gamma+1)}{(\gamma-1)} \tag{2.50}$$

$$v_a = \left(\frac{\gamma+1}{2}\right)^{0.5}\ \left(\frac{P_b}{\rho_a}\right)^{0.5} \tag{2.51}$$

$$v_b = \left(\frac{(\gamma-1)^2}{2(\gamma+1)}\right)^{0.5} \left(\frac{P_b}{\rho_a}\right)^{0.5} \qquad 2.52$$

$$\frac{T_b}{T_a} = \frac{\gamma-1}{\gamma+1} \frac{P_b}{P_a} \qquad 2.53$$

A shock compression is not isentropic as viscosity and heat conduction are present and increase the internal energy. The shock Hugoniot (Fig. 2.2) shows the Hugonoit A-B defining the possible final states and the isentrope

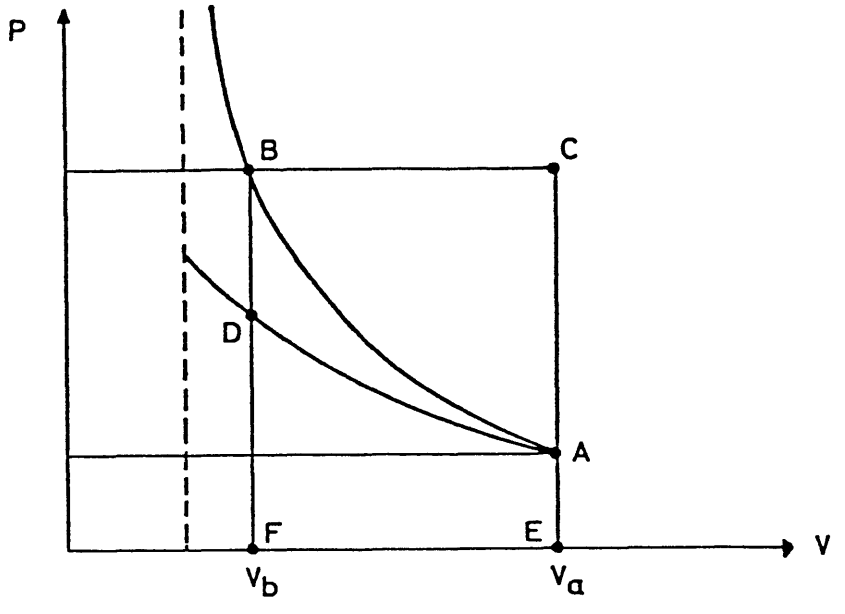


Fig. 2.2 THE SHOCK HUGONIOT (see text)

A-D. The difference in energy is just the difference in area under the two lines. The inference is that successive weak shocks can achieve a higher final density as the total effect will follow the isentrope much more closely than a single strong shock which leads asymtopically to a limiting final density.

In some targets shock reflection will occur and the intake velocity of the reflected shock is dependent on the exhaust velocity of the first wave but the pressure ratio after a reflected shock is constant at 6 (24).

For spherical targets it is necessary to know the effect of spherical convergence on a shock wave. From a simple appreciation it can be seen that the pressure driving the shock will increase as the area it is driving decreases to conserve momentum flux also the shock velocity accelerates as the wave moves in.

This effect combined with the reflected shock effect gives a large jump in density. The large compression allied with the associated heating can raise the core to thermonuclear conditions, being limited by implosion symmetry or the ion mean free path (this is of the order of the shock front thickness).

In microsphere targets the shock has to propagate from the high density shell material to the lower density of the fill gas. For negligible pressure of filler gas the inner surface of the shell moves inwards once the shock front has passed and a rarefaction wave moves back into the shell. The inward movement of the shell acts as a driver for a shock into the gas.

2.4 EQUATIONS OF STATE

When matter is compressed the relationship between pressure and density (the equation of state) is of great importance. For inertial confinement targets (microspheres) the filler gas can be approximated reasonably by the ideal gas law but for the effects of pressure on solid material other descriptions have to be used.

The ideal gas law derived from classical thermodynamics, gives the results:

$$P\,\rho^{-\gamma} = \text{const} \qquad 2.54$$

$$T\,\rho^{(1-\gamma)} = \text{const} \qquad 2.55$$

and

$$\gamma = \frac{\ln P}{\ln \rho}_{s} \qquad 2.56$$

where γ is the ratio of specific heats which in the case of a monatomic gas is 1.66, alterations to the internal energy states of the associated particles will reduce this value.

Equation 2.54 applied to the final and initial states of a compressed gas for a given initial density and final pressure shows that to maximise the final density a low initial pressure is required underlining the need to reduce preheat.

In the case of cold dense matter the Fermi degenerate electron gas model may be applicable. As they are fermions there can only be two electrons per phase space volume of h^3 so the electrons will fill up the available phase space to a level E_F, the Fermi energy, and this will determine the minimum pressure of the cold free electron gas

$$E_F = \frac{1}{8}\left(\frac{3}{\pi}\right)^{0.66} \frac{h^2}{m_e} n_e^{\,0.66} \qquad 2.57$$

$$P_F = \frac{1}{20}\left(\frac{3}{\pi}\right)^{0.66} \frac{h^2}{m_e} n_e^{\,1.66} \qquad 2.58$$

this shows the same power law as the ideal gas case and they are equivalent when $kT >> E_F$. This model is generally applicable where $kT < E_F$ but it is limited by the fact that it does not include the Coulomb interactions. In the range of practical interest these energies are comparable to the Fermi energy and so should be considered. The Thomas-Fermi model treats the electron energy as the sum of kinetic and Coulomb potential energy and provides a self consistent solution where the electron density at the 'boundary' of each atom is reduced from the average by the concentration of electrons around the nucleus. The pressure is then taken as the Fermi degenerate pressure of the boundary electron density. This model is equivalent to the free electron gas in the case of $kT >> E_F$ and to the Fermi degenerate gas for $E_F >> kT$ but at low densities the pressure falls more rapidly.

One of the problems with the above models is that they do not include the quantum mechanical binding forces which hold a solid in equilibrium. These are of the order 100 kbar and so the above models predict large values of pressure for solids at room temperature, hence they are only useful for megabar pressures. Calculations including the binding forces have been done (58) and give results in the cold compression case comparable with experimental data.

There have been experimental determinations of the equation of state principally be measuring parameters in the Rankine Hugoniot equations (57,59,60). These have been extended by semi empirical methods and exist as a 'library' of numerical tabulations (60).

2.5 RAYLEIGH-TAYLOR INSTABILITIES

The shells of inertial confinement microspheres are subject to Rayleigh-Taylor instability. When a low density medium accelerates a high density one the interface may go unstable. The classical growth rate is given by

$$\gamma = (\alpha\, k\, a)^{0.5} \qquad 2.59$$

where:

α - is the Attwood number $\left(\frac{\rho_1 - \rho_2}{\rho_1 + \rho_2}\right)$

k - the spatial wave number

a - the acceleration.

Hence large wave numbers have the biggest growth rate but saturate earlier. The situation is more complex for finite thickness layers and diffuse boundaries but it will appear from calculations by Bodner et al (61) that for shell targets the maximum growth rate is for wavelengths of the order of the shell thickness (Δr) i.e.

$$\gamma\, t_{MAX} = \left(4\pi\ \alpha \frac{r}{\Delta r}\right)^{0.5} \qquad 2.60$$

using

$$a = \frac{2r}{t^2} \text{ and } K_{MAX} = \frac{2\pi}{\Delta r} \text{ in equation 2.43}$$

Here r is the target radius and shows that the aspect ratio of the target $\frac{r}{\Delta r}$ is important for stability in imploding shell targets.

2.6 THE THESIS WORK

The topics in this chapter show that in theory a useful gain can be made in ablation pressure by using shorter laser wavelengths. In subsequent chapters experimental work will be presented to support this using a consistent method over a range of laser intensities and wavelengths.

In this work, on plane targets, the energy was found to be transported laterally out of the focal spot region for large values of intensity. This intensity cut off was found to decrease with laser wavelength. Spherical targets, evenly illuminated, are not prone to this apparent energy loss.

CHAPTER THREE

PREVIOUS EXPERIMENTAL WORK

			Page
3.1	INTRODUCTION		47
3.2	EXPLODING PUSHERS		47
	3.2.1	THEORETICAL MODELS	47
	3.2.2	EXPERIMENTAL OBSERVATIONS	48
3.3	ABLATIVE PUSHERS		50
	3.3.1	SCALING OF ABLATIVE IMPLOSIONS WITH LASER PARAMETERS	50
	3.3.2	METHODS OF ABLATION PRESSURE MEASUREMENT	52
		3.3.2.1 RECOIL METHODS	52
		3.3.2.2 FARADAY CUP MEASUREMENTS	53
		3.3.2.3 SHOCK WAVE PROPAGATION	53
		3.3.2.4 X-RAY SPECTROSCOPY	53
	3.3.3	EXPERIMENTAL OBSERVATIONS	54
	3.3.4	COMPILATION OF PREVIOUS RESULTS	55

3.1 INTRODUCTION

The last chapter looked at the pressures involved in laser produced plasmas. These lead to two possible compression methods, the exploding pusher type and the ablative compression type.

The exploding pusher mode is where the energy in the hot electron preheat (produced at high values of $I\lambda^2$) is deposited in the microballoon wall on a timescale short compared with the expansion time. The wall will then explode with half going inwards and half outwards. The inward moving part pushes the filler gas before it to form a compressed core. Using a target of small mass maximises the specific energy delivered by the laser and enables thermonuclear burn to occur. This method of compression produces high temperatures but low densities (and pressures) due to the preheating of the filler gas by hot electrons and the non-isentropic compression.

The ablative mode avoids hot electron preheat, the laser pulse being tailored for duration and shape so that the heating is confined to the target surface. This ablates off accelerating the rest of the shell inwards. With good laser pulse shaping this method can produce near-isentropic compression.

3.2 EXPLODING PUSHERS

3.2.1 THEORETICAL MODELS

Models were developed by Storm et al (62) and Rosen and Nuckolls (63) but have been reviewed and extended by Ahlborn and Key (64).

The Storm model made two assumptions and also included a number of arbitrary constants. They assumed that the imploded density was proportional to that obtained if the pusher shell

expanded uniformly to fill the sphere (i.e. $\rho_F \propto \frac{\Delta R}{R}$) and that the temperature in the core is proportional to that part of the energy absorbed before the shell has moved past 0.66 of the initial radius. It is notable that this model describes, well, neutron yield over a wide range of targets and laser energy.

Rosen and Nuckolls introduced into their model consideration of the shock preheating followed by adiabatic compression when calculating the ion temperature to obtain a value of neutron yield.

Ahlborn and Key considered the problem as a whole following the development of the implosion to predict the final values of temperature and density. In their shock wave model they assumed that the laser pulse is short so that the shell of the target is instantaneously (and homogenously) heated. The implosion then creates a shock wave which is reflected from the centre and may be reflected again from the imploding pusher-gas interface but after the first reflection subsequent ones grow weak and can be approximated by an adiabatic compression. On calculating the final pressure they obtain a maximum which does not take into account radiation losses, rarefaction waves in the pusher material, fast-electron preheat of the gas and non-symmetric illumination.

3.2.2 EXPERIMENTAL OBSERVATIONS

Initial work on this topic by KMS Fusion Inc. (65) used a two beam Nd-glass laser with a pulse length between 30-1000 ps, energy up to 230 J and power up to 200 GW. Their focussing system involved a 'clamshell' technique enabling nearly spherical illumination.

With DT filled glass microballoons and irradiances up to 4×10^{15} W cm^{-2} they obtained neutron yields when the specific energy exceeded 0.7 J/ng. The compression ratios (>100) were

inferred from X-ray pinhole pictures and the ion temperature obtained from an analysis of the compression and expansion of a DT sphere and data of thermonuclear reaction rates as a function of temperature.

Lawrence Livermore Laboratory (LLL) with their bigger lasers could obtain greater specific energies and so larger yields from which the fusion products could be studied. Ion temperatures inferred by observation of the energy spectrum of 3.52 MeV α particles (66) gives values of 3 to 4 kev for yields of ~10^6 neutrons. These measurements also confirmed the products were of thermonuclear origin and not from fast ions striking absorbed D_2 in the chamber walls (67).

LLL obtained yields of up to 10^9 neutrons and ion temperatures up to 8 kev from the Argus system (68) producing 5 TW in two beams focussed by f/1 lenses. On these larger yields time of flight analysis of the neutron flux was possible and removed any possible ambiguity about the α particle measurements due to scattering in the glass shell.

There is evidence (69) that improvements in the implosion symmetry will greatly enhance the neutron yield. Work with other laser wavelengths (70,71) suggests that the exploding pusher properties are not purely wavelength sensitive but depend on the $I\lambda^2$ product determining the conversion to fast electrons.

There have been a number of different ways of measuring the core density. X-ray line width measurements (72,73,70) have been carried out at the Rutherford laboratory (RL), LASL and LLE, RL have also used an X-ray shadowgraph technique (74), KMS X-ray pinhole images (75), zone plate coded images of particle emissions have been used at LLL (76). The spectroscopic methods (with spatial resolutions) enabled separate determination of the time averaged density, temperature and plasma dimensions of the compressed gas and the imploded glass to be made.

A graph of the density results is shown in Fig. 3.1 and compared with the three models Storm, Rosen and Nuckolls and Ahlborn and Key. A lot of scatter is evident particularly in the KMS results possibly due to a different measurement technique but is more probably a feature of their good illumination symmetry as other six beam shots (see Chapter 8) get similar good compressions.

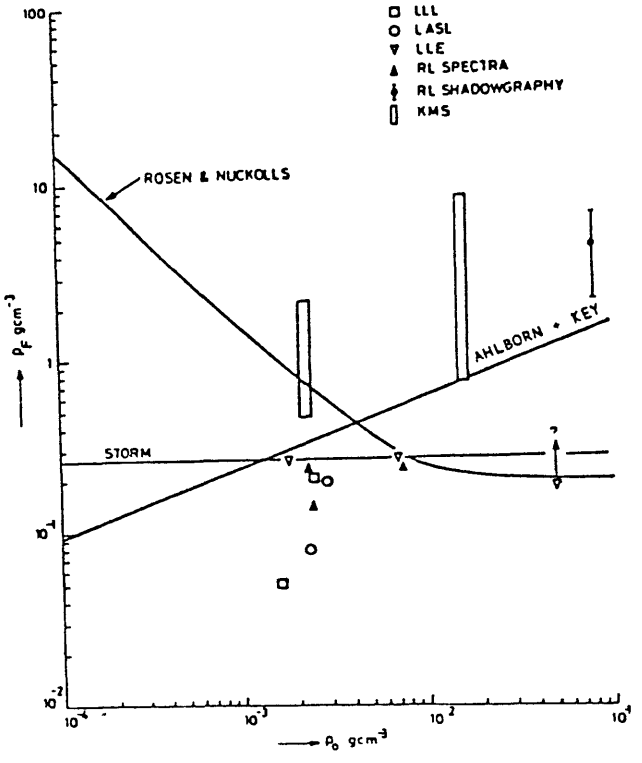


Fig. 3.1 DENSITY OBSERVATIONS IN EXPLODING PUSHER TARGETS (24)

3.3 ABLATIVE PUSHERS

3.3.1 SCALING OF ABLATIVE IMPLOSIONS WITH LASER PARAMETERS

From the scaling of the hot electron production threshold ($I\lambda^2 \sim 10^{14}$ W cm^{-2} μm^2) it is apparent that there will be an optimum irradiance for the ablation process dependent on the laser wavelength. Above this an increased amount of energy goes into hot electrons, and not into the ablation process, preheating the fill gas and reducing compression.

Using laser wavelengths longer than ~1 μm is not pratical for truly ablative implosions requiring very large aspect ratio targets. One method to avoid this is to use a quasi-ablative approach where the high aspect ratio high density shell is surrounded by a thick low density material so a high value of $I\lambda^2$ can be used. The thick low density layer absorbs the energy from the fast electrons without appreciably reducing the terminal velocity as its mass is low, it also reduces the possibility of Rayleigh-Taylor instability.

Multilayer targets have also been proposed to optimise the fusion yield for ablative compressions using short laser wavelengths (77). They involve the use of the following devices:

a) a low density jacket to reduce Rayleigh-Taylor instability growth

b) a double shelled target giving velocity doubling when the outer shell strikes the lower mass inner one

c) preheat shields to protect the fuel from radiative and hot electron preheat

d) two fuel layers, the outer containing most of the fuel and the inner one to act as an igniter.

These principles form the basis of long term laser fusion target design and are generally for unshaped laser pulses. For a properly shaped laser pulse the compression can be made isentropic on simple targets. Analyses by Kidder (78) and Ashby (79) on shell targets lead to the time history of the pressure at the interface to be

$$P(t) = P(o)\ (1-\tau^2)^{0.5} \qquad 3.1$$

where

$$\tau = \frac{t}{t_c} \qquad 3.2$$

and

t_c - the time to collapse to zero radius.

A simple scaling model can relate this to the laser intensity but gives a laser pulse shape where the higher intensity levels are outside the ablative regime, even so the model gives lower bounds on the laser requirements.

3.3.2 METHODS OF ABLATION PRESSURE MEASUREMENT

Part of the reason for the lack of experimental results of ablative implosions compared with exploding pusher implosions is the diagnostic difficulties due to the high density and low temperature of the cores produced.

The methods of ablation pressure measurement are largely indirect measurements of mass motion and make basic assumptions about the energy transport. They are also time independent and make no allowances for the time varying intensity of the irradiating laser pulse.

3.3.2.1 RECOIL METHODS

The pressure is inferred by measuring the recoil momentum of a massive target (80,81). Rumsby et al (82) measured the recoil velocity of small metal foils irradiated by ruby and CO_2 lasers using ruby laser shadowgraphy. The models of Cooper (53) and Puell (49) were employed assuming the mass ablated by the laser was negligible to obtain a scaling of ablation pressure of

$$P \propto I^{0.75} \lambda^{-0.25} \qquad 3.3$$

This study was for laser intensities between 3×10^9 W cm^{-2} and 5×10^{10} W cm^{-2} for the CO_2 laser and between 5×10^9 W cm^{-2} and 3×10^{11} W cm^{-2} for the ruby laser and shows good agreement with the self regulating inverse Bremsstrahlung ablation model (see Section 2.2.3).

This method is unsuitable for measuring the instantaneous pressure during a short laser pulse as the explosion of the target due to hot electron preheat contributes to the results giving anomalously high values.

3.3.2.2 FARADAY CUP MEASUREMENTS

The Naval Research Laboratory used a set of Faraday cups to analyse not only the forward moving residual target but also the backward moving ablated material (83). Their targets were 10 μm thick polymer foil targets irradiated at 3×10^{12} W cm^{-2} and 10^{13} W cm^{-2} using a 1 μm, 3 ns laser pulse. This method is prone to the same drawbacks as the recoil methods.

3.3.2.3 SHOCK WAVE PROPAGATION

Measurement of the shock wave velocity in the solid material can provide a value of the ablation pressure initiating the shock provided the equation of state of the shocked material is known (see Sections 2.3 and 2.4).

This method was investigated by Van Kessel and Sigel (84, 85) using solid hydrogen, and plexiglass targets with observations using high speed photography and irradiated with a 1.06 μm Nd laser pulse of 5 ns duration and 10 J.

Fast electron preheat again confuses the results as it perturbs the solid material ahead of the shock.

3.3.2.4 X-RAY SPECTROSCOPY

A method of separating out the effects of ablation and preheat is to use the self generated X-ray emission from the heated material. The X-ray intensity scales roughly as

$$I \propto \rho^2 \, T^{0.5} \, \exp\left(-\frac{h\nu}{kT}\right) \qquad 3.4$$

and so the ablation front region provides the greatest thermal X-ray emission. The relevant plasma parameters n_e and T_e can be determined spectroscopically (see Chapter 7) by the Stark broadening of spectral lines and the soft X-ray continium slope respectively.

Galanti and Peacock (86) have used this method on polyethylene targets irradiated at 10^{12} W cm^{-2} with 1 μm, 5 ns laser pulses and Key et al (87,88) at 2 x 10^{15} W cm^{-2} with 1 μm 100 ps laser pulses on glass microballoon targets using space resolved X-ray spectroscopy.

3.3.3 EXPERIMENTAL OBSERVATIONS

The main results come from time integrated X-ray pinhole pictures which give an indication of the compression ratio and the electron temperature which when compared with computations (89) indicate a localised hot core inside a cold dense region.

Work done by CEA Lemeil Laboratory (90) using high aspect ratio glass microballoons, 1.06 μm laser light at 10^{14} W cm^{-2}, streaked X-ray and 2 ω_0 (0.53 μm) emission enabled a deduction of implosion time of ~1 ns.

Results quoted by Key (24) from Lawrence Livermore Laboratory using Shiva gave a core with significant preheating to give a neutron yield of ~10^7 and used a novel radio chemistry method to deduce $\rho \Delta r \sim 4 \times 10^{-2}$ cm^{-2}. Analysis using a hydrodynamic code gave a pressure of ~4000 Mbar, and a density of ~10 gm cm^{-3}, though improving on the exploding pusher values it is still far from the projected value of 1000 gm cm^{-3}.

More recently the Rutherford Laboratory (72) has investigated the implosion dynamics more thoroughly by the use of X-ray shadowgraphy using a back-lighting X-ray source which is absorbed as it passes through the dense region of the imploding target. The resulting flux is imaged onto film through a slit via a streak camera cathode. The dynamical development from this and other data suggests the onset of Rayleigh-Taylor instability.

3.3.4 COMPILATION OF PREVIOUS RESULTS

Putting this data together (see Fig. 3.2) with the

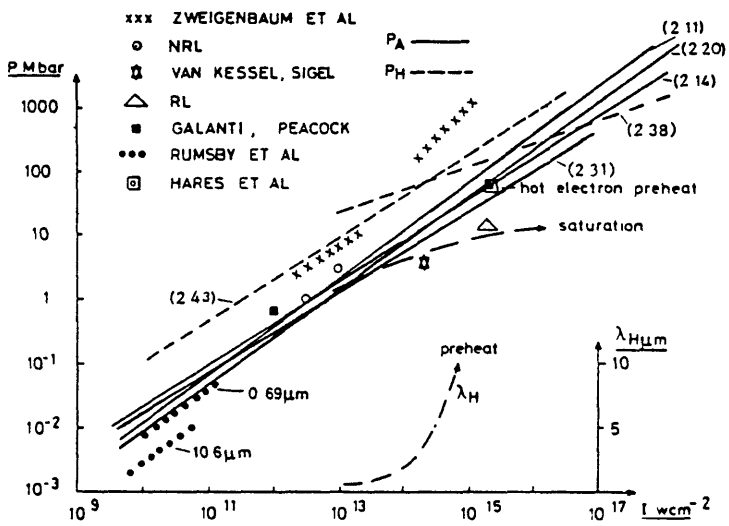


Fig. 3.2 ABLATION PRESSURE OBSERVATIONS WITH SIMPLE ANALYTIC MODELS (EQUATION NUMBERS IN BRACKETS) (24)

predictions of the simple analytic models from Chapter 2, it can be seen that the model descriptions do not differ appreciably in the laser intensity range of interest and the experimental data is in fair agreement. Even so one model may be more applicable in a given region than the others except above intensities of $\sim 10^{15}$ W cm^{-2} where the pressure appears to saturate. Detailed work at the Rutherford Laboratory (91) has shown that this is due to the production of hot electrons, thermal flux inhibitions,

and, as will be shown later, lateral energy transport. This leads to a decrease in the proportion of laser energy coupled into the surface ablation process. This reduction in effective absorption can be offset somewhat by decreasing the laser wavelength.

CHAPTER FOUR

THE DETERMINATION OF MASS ABLATION RATE BY TIME RESOLVED X-RAY SPECTROSCOPY

			Page
4.1	INTRODUCTION		58
4.2	PRINCIPLE OF MEASUREMENT		59
4.3	EXPERIMENTAL DETAILS		62
	4.3.1	LASER BEAM CHARACTERISTICS	62
	4.3.2	TARGETS	65
	4.3.3	DIAGNOSITICS	67
		4.3.3.1 AREA MASS DENSITY	67
		4.3.3.2 BURNTHROUGH TIME	67
		4.3.3.3 LASER ENERGY	69
		4.3.3.4 PULSE DURATION AND TIME HISTORY	69
		4.3.3.5 FOCAL SPOT SIZE	69
		4.3.3.6 TIME INTEGRATED SPECTROSCOPY	71
		4.3.3.7 FARADAY CUPS	71

4.1 INTRODUCTION

The advantages of using X-ray spectroscopy in measuring ablation pressure were outlined in the last chapter, in particular it can be used to separate the effects of ablation from those of hot electron preheat. It can also be used to measure the rate at which mass is ablated away from the target surface. One way of doing this is (92,93,94) by using a layered target whose materials differ in atomic number by one or two. A series of laser shots are then attempted at decreasing intensities to establish the intensity at which the X-ray emission from the underlying layer just disappears. This then associates a given intensity with a given mass density. Using the pulse duration a mass ablation rate can be calculated and the ablation pressure can then be inferred either by using a particle velocity measurement or by energy balancing.

These experiments used time integrating X-ray spectrometers needing a number of shots to establish one mass ablation rate value making the measurement susceptible to changes in laser and target parameters. Also filamentation of the laser beam (14,95) could cause a high burn through rate.

In the work presented here this method was extended by employing an X-ray streak camera to follow the time history of the spectrally resolved X-ray emission and enable the time of transition from the characteristic spectra of the top layer to that of the underlaying layer to be directly measured (see Fig. 4.1). Although time resolved spectroscopy has been previously used on single element targets (96), this is the first use of time resolved spectroscopy on layered targets. Furthermore three different laser wavelengths have been used showing that gains in ablation pressure are available for shorter laser wavelengths.

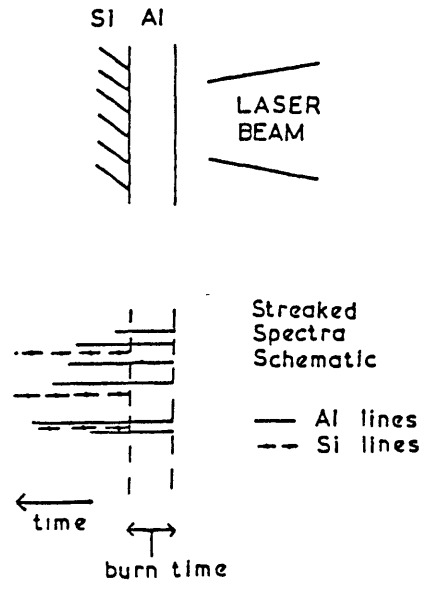


Fig. 4.1 METHOD OF BURNTIME MEASUREMENT SHOWING THE DELAY OF THE SILICON EMISSION WITH RESPECT TO THE ALUMINIUM EMISSION

4.2 PRINCIPLE OF MEASUREMENT

The experimental set up is illustrated in Fig. 4.2. The laser beam of wavelength λ, duration (for a square pulse) τ, and energy E is focussed onto the layered target (surface layer of thickness ℓ, and density ρ) in a spot of radius r. The time of burn through, t_B, is then obtained from the streaked spectra. From these observables the specific mass ablation rate can be determined to a first approximation as

$$\dot{m} = \frac{\rho \ell}{t_B} \qquad 4.1$$

and the incident laser intensity as

$$I_o = \frac{E}{\tau \pi r^2} \qquad 4.2$$

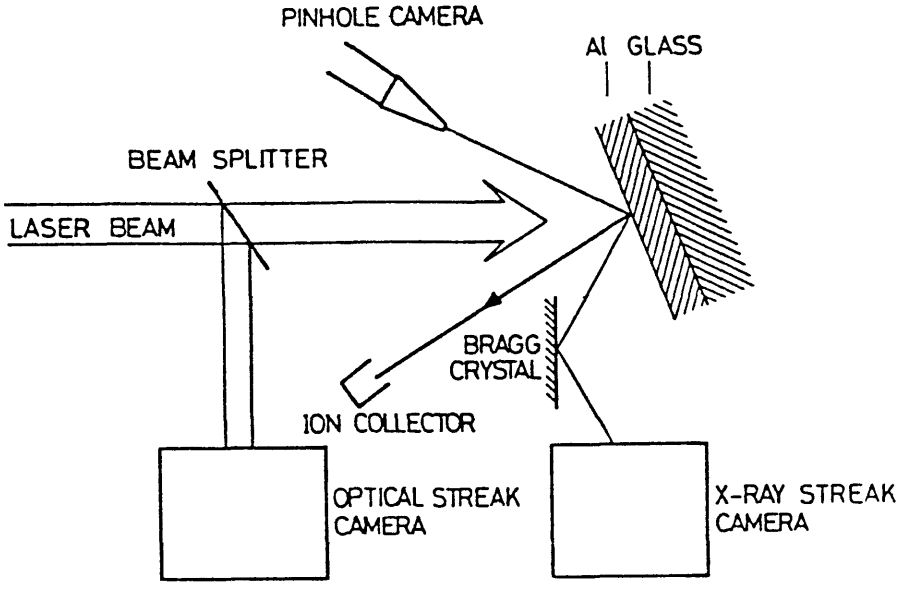


Fig. 4.2 SCHEMATIC DIAGRAM OF THE PLANE TARGET MASS ABLATION RATE EXPERIMENT

These expressions are approximate in a number of ways:

a) the laser pulse is assumed to be a 'top hat' function with respect to time

b) all the laser energy is absorbed and goes into the ablation process

c) the radius of the spot is constant and well defined with no lateral energy spread

d) the burn rate across the ablation front is constant, so burn through is even.

A correction factor can be introduced to account for the intensity variation of the laser pulse with time so that the value of $\dot{m}$ obtained is then uniquely identified with a specific intensity (in this case the peak laser intensity). Assuming:

$$\dot{m} = CI^{\alpha} \qquad 4.3$$

where I is the instantaneous irradiance.

Introducing the time dependence of the laser pulse as

$$I = I_o f(t) \tag{4.4}$$

where I_o is the peak irradiance.

Combining equations 4.3 and 4.4 and integrating over the burn time produces

$$\int_o^{t_B} \dot{m}\, dt = \rho\ell = CI_o{}^{\alpha} \int_o^{t_B} f(t)^{\alpha}\, dt = CI_o{}^{\alpha}\, t_I \tag{4.5}$$

where t_I is the integral. Hence

$$\frac{\rho\ell}{t_B} = \frac{CI_o{}^{\alpha}}{t_B}\, t_I \tag{4.6}$$

If we now refer the required value of $\dot{m}$ to the peak laser intensity i.e.

$$\dot{m}_p = CI_o{}^{\alpha} \tag{4.7}$$

then

$$\dot{m}_p = \dot{m}\,\frac{t_B}{t_I} \tag{4.8}$$

$\frac{t_B}{t_I}$ is then the correction factor needed to get a mass ablation rate for the peak laser intensity of a shot irrespective of the burn time. A first approximation to the value of α can be obtained from equations 4.1 and 4.2. This procedure could be repeated once a new scaling law (equation 4.3) is obtained from the new figures. In the present case it was found that any further iteration would not have reduced the scatter in the data appreciably.

This correction also meant that the intensity value had to be corrected from an average value to the peak value. This was done by a simple integration of equation 4.4 so that

$$\varepsilon = \int_o^{t_F} I_o f(t)\, dt = I_o\, \tau \tag{4.9}$$

where ε is the area energy density of the laser pulse (assumed to be constant over the focal spot, see Section 4.3.1).

$$\varepsilon = \frac{E}{\pi r^2} \qquad 4.10$$

and t_F is the total duration of the laser pulse. Thus

$$I_o = \frac{\varepsilon}{\tau} = \frac{E}{\pi r^2 \tau} \qquad 4.11$$

The other assumptions inherent in the equations 4.1 and 4.2 will be discussed in Chapter 5.

4.3 EXPERIMENTAL DETAILS

The series of experiments presented below produced the first comparative measurement of the mass ablation rate over a range of laser intensities from 2×10^{13} W cm^{-2} to 2×10^{15} W cm^{-2} at three laser wavelengths 1.05 μm, 0.53 μm and 0.35 μm on plane targets from single shot data.

4.3.1 LASER BEAM CHARACTERISTICS

These experiments were performed at the Rutherford Central Laser Facility using the 1.05 μm (ω_0) Neodymium phosphate glass laser VULCAN (14) in its long pulse mode. This produced a Q switched envelope from which a pulse of 1.5 ns was switched using a two stage Pockells-cell gate. The prepulse level was measured as less than 10^{-5} of the peak intensity by a photodiode system.

The spatial profile of the beam was controlled by an apodiser to give a shape as shown in Fig. 4.3 which shows the near field beam profile (at 1.05 μm). The intensity at the centre is approximately twice that if the filling of the aperture were uniform. Superimposed on this is noise which fluctuates to ±30% on scale lengths of 0.1 cm to 1 cm over a total final disc diameter of 10.8 cm. This noise results from interference fringes in the beam splitters, air turbulence, optical defects and dust.

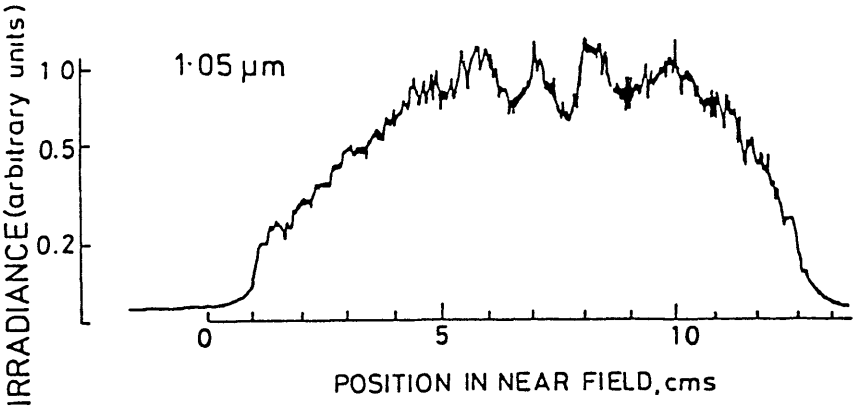


Fig. 4.3 1.05 μm NEAR FIELD SPATIAL BEAM PROFILE

The experiments at 1.05 μ were conducted with the 1.5 ns pulse at typically 60 J on target. The beam was focussed by an f/1 doublet aspheric lens (97). The quality of the lens was good enough that the intensity variations in the focal spot were dominated by the beam characteristic.

Alignment of the targets was achieved by expanding a CW YAG laser in an achromatic Cassegrainian telescope and then leading the beam via the main laser optics onto the target. The reflections of the beam from the target were viewed with a telemicroscope system and the target was moved by a stepping motor towards the lens until it was in the focal plane when the far field image was of minimum size. The targets were then moved further towards the lens to achieve the desired irradiance. The laser energy was held approximately constant.

For the experiments at 0.53 μm the main laser beam was frequency doubled using a type II KDP crystal (thickness 12 mm, diameter 110 mm) (98). To increase the peak power the incident laser pulse was shortened to 0.8 ns and was further shortened to 0.6 ns by the non-linear conversion process in the crystal. The conversion efficiency was not optimised resulting in only about 15 J of second harmonic radiation on target.

The same lens was used as for the 1.05 μm shots with the spacing of the doublet being adjusted for 0.53 μm use. The beam path was formed using 0.53 μm dielectric mirrors which reduced the residual 1.05 μm radiation to less than 0.1%. The different focal lengths at 1.05 μm and at 0.53 μm ensured that the intensity of 1.05 μm irradiation was even lower at $\sim 10^{-5}$ of the intensity of 0.53 μm radiation.

Target positioning was achieved using the same method as for 1.05 μm but with an intra-cavity frequency doubler in the CW YAG laser.

Third harmonic generation (0.35 μm) was achieved by using a second type II KDP crystal (9 mm thick) and summing some of the infra-red, unconverted by the first crystal, with the 0.53 μm photons. The polarisation mismatch scheme of Craxton (99,100) was used. The energy of 0.35 μm radiation on target was typically 5 J and the pulse length was 0.7 ns. Figure 4.4 shows a near field image of the 0.35 μm beam. The central dip is due to an over corrected apodization and the interference patterns are produced by Fresnel reflections in the uncoated windows of the cells containing the KDP crystals. The residual 1.05 μm and 0.53 μm intensities were reduced to less than 10^{-5} of the 0.35 μm intensity by the dielectric mirrors and chromatic aberations in the lens which was an f/2.5 fused silica spherical doublet.

The target alignment system was the same as described above except that an Argon-Ion laser (using wavelength 0.476 μm) was used instead of the CW YAG. The wavelength discrepancy was taken into account by displacing the target from the Argon-Ion laser focus by an amount calculated from the focal length and refractive indices of the fused silica.

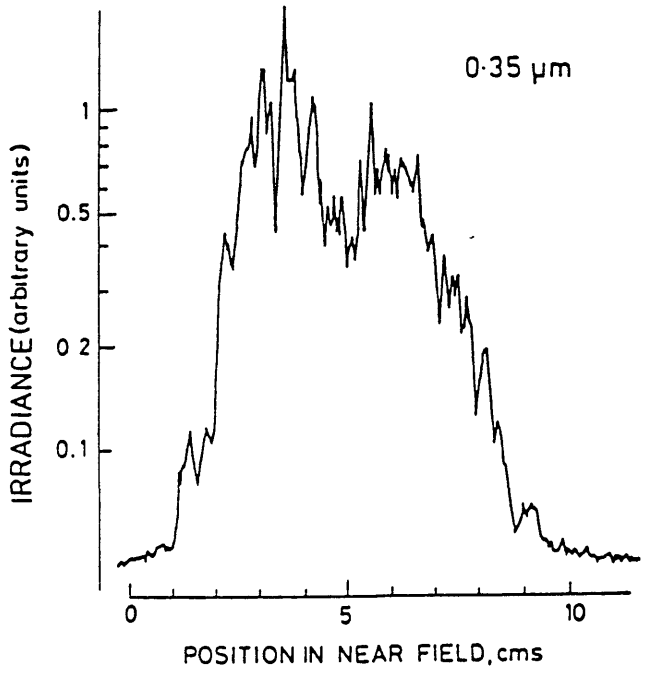


Fig. 4.4 0.35 μm NEAR FIELD SPATIAL BEAM PROFILE

4.3.2 TARGETS

The majority of the targets used were glass microscope slides coated by thermal evaporation with a layer of aluminium at solid density. The layer thickness was varied, for different targets, between 0.1 μm and 2.0 μm as measured by a film thickness monitor.

Aluminium and silicon (in the form of glass or silicon monoxide (S_iO) were chosen for the layers as they are;

a) easy to handle with respect to reactivity, toxicity, etc.

b) easy to deposit in even, thin layers

c) of medium atomic number (13 and 14 respectively) so that at the electron temperature found in these plasmas, characteristic hydrogen-like and helium-like resonant line emission is produced at easily detectable levels, and

d) of adjacent atomic numbers and have line emissions which overlap in the wavelength range of readily available equipment allowing detection on one instrument.

During the 0.35 μm run some slightly different targets were used. These had silicon monoxide as the top layer deposited on a thick layer of aluminium, using the glass slide as a base only. This allowed the n=1 to n=2 transitions of silicon and aluminium to be used allowing burn through to be detected at lower laser intensities. It is not possible to use these lines for aluminium coated targets as the long lifetime of the aluminium resonance lines obscures the silicon radiation (see Fig. 4.5).

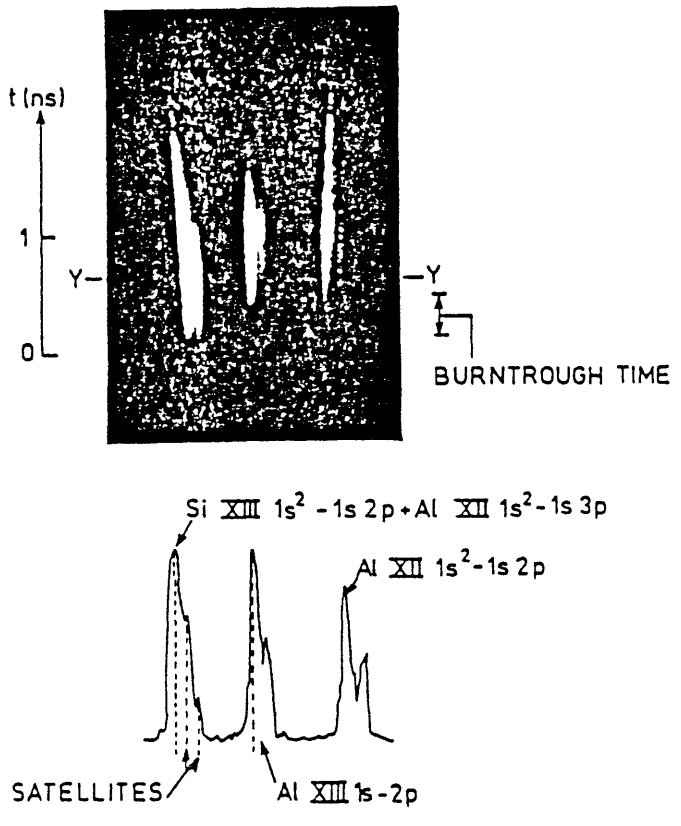


Fig. 4.5 TYPICAL STREAK OF A SILICON MONOXIDE ON ALUMINIUM TARGET (THE S_i XIII $1s^2$–1s2p IS COINCIDENT WITH THE Al XII $1s^2$–1s3p)

The targets were mounted at the centre of the vacuum chamber with the target normal angled at 15° (see Fig. 4.2) away from the laser beam axis to ensure that the path from the interaction region to the X-ray streak camera slit was not blocked by the target edge and that ion collectors could be placed close to the direction of maximum ion emission.

4.3.3 DIAGNOSTICS

4.3.3.1 AREA MASS DENSITY

The area mass density of the top layer of the target was measured during its deposition by a commercial film thickness monitor. With the deposition occurring at approximately solid density a value for the layer thickness could be obtained and compared well against a direct measurement of thickness by electron microscope.

4.3.3.2 BURN THROUGH TIME

This was measured by an X-ray streak camera spectrometer (101) with a low density caesium iodide cathode, and Bragg reflection from a thallium-acid phthalate crystal (TlAP,2d = 25.75 Å). The spatial resolution of the streak camera determined the spectral resolution to be $\frac{\lambda}{\Delta\lambda}$ = 500. The streak speed used was 100 ps/mm giving a time resolution of 30 ps projected to be 300 μm on the cathode (101).

The sensitivity of the whole system was such that a good exposure was possible from a single laser shot, on Ilford HP5 (400 ASA) using a Hadland 50/40 optical intensifier.

A typical streak from one of these shots is shown in Fig. 4.6. The spectral lines shown are the higher energy members of the hydrogen-like and helium-like resonance transitions of

aluminium and silicon and the associated continua. This is for the aluminium on glass targets. Figure 4.5 shows a typical result for the silicon monoxide on aluminium targets. The lines here are the lower members of the same spectral series (i.e. Si XIII $1s^2$-1s 2p mixed with Al XII $1s^2$-1s 3p, Al XIII 1s-2p and Al XII $1s^2$-1s 2p).

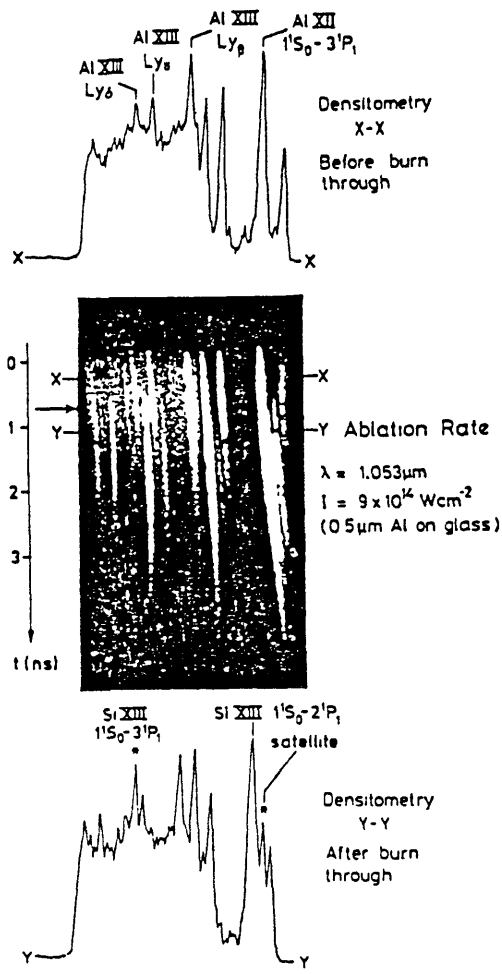


Fig. 4.6 TYPICAL STREAK OF AN ALUMINIUM ON GLASS TARGET

It can be readily seen from the timescale that the resonance transitions are relatively long lived compared to the continua which was helpful in identifying the time origin on the film. This and deciding where a line started were the main problems in making the measurement of burn through time. I will discuss this further in Chapter 5.

4.3.3.3 LASER ENERGY

The measurement of the laser energy was essentially the same at all three laser wavelengths. An Apollo calorimeter measured the total (time integrated) energy in a fraction of the beam split off just before the pulse entered the target chamber. This was scaled to the energy on target by the transmission factor of the chamber windows, the lens and the pellicle (if used) and the reflection factors of any intervening mirrors and beam splitters. The typical energies on target were 60 J, 15 J and 5J for 1.05 μm, 0.53 μm and 0.35 μm respectively.

4.3.3.4 PULSE DURATION AND TIME HISTORY

The full width half maximum (FWHM) of the laser pulse was measured using an optical streak camera with an optical multi-channel analyser as a recording medium. A set of filters was used for bandwidth and intensity control of the incoming laser radiation. A typical result for 0.53 μm is shown in Fig. 4.7. The time resolution is 50 ps, and indicates a trapezoidal shape with the decay slower than the attack. This was more pronounced for 1.05 μm pulses (see Chapter 5).

4.3.3.5 FOCAL SPOT SIZE

The focal spot radius was monitored using an X-ray pinhole camera with two channels, one being filtered to 1.4 kev (1/e transmission of 25 μm Be) and the other to 2.4 kev (1/e transmission of 125 μm Be). The pinholes were of 6 μm diameter in a platinum subtrate of 20 μm thickness. This gave a

resolution of approximately 10 μm. The whole system had a magnification of 4. The recording medium was either Industrex C or Kodirex X-ray films.

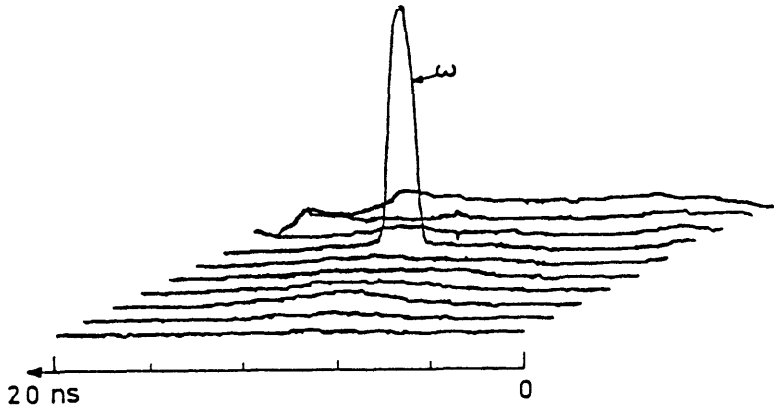


Fig. 4.7 OPTICAL MULTI-CHANNEL ANALYSER PICTURE OF THE 1.05 μm LASER PULSE

The pinhole camera was positioned above the main lens at an angle of approximately 70° to the laser beam axis meaning the vertical dimensions of the focal spot were foreshortened. The spot diameter was taken as the FWHM intensity of the major axis of the elliptical spot formed by the X-ray emission on the film, after being corrected for film response (102).

This instrument also provided valuable information as to the uniformity of the focal spot. For 1.05 μm and 0.53 μm this appeared to be good (fill factors of ~50%) but for 0.35 μm with large focal spots the image was of a ring of emission (fill factor of about ~10%) due to spherical aberrations in the lens which was sometimes broken up into hot spots (see Figs. 5.1, 5.2 and 5.3). These were probably caused by a combination of beam inhomogeneities, which were exacerbated by the non-linear frequency multiplication, and self focussing in the under dense plasma (14,95). These effects, if present will lead to anomalously fast burn through and as all spot sizes of over 100 μm were suspect, for the 0.35 μm cases, they were removed from the results.

The most basic assumptions in using this measurement is that the width measured is proportional to and representative of the actual size of the spot over which the laser energy is absorbed and dissipated. This was found not to be the case and that, particular at small spot sizes, a substantial proportion of the laser enegy was transported laterally out of the 'focal' region and into the low temperature surrounding material. This did not show up on the pinhole pictures as the area was too cold to emit enough X-rays at a short enough wavelength to be detected.

The sizes of the images from the differently filtered channels in the pinhole camera agreed well with each other (and also with the size calculated from the f number of the lens and its defocus, see Fig. 5.4), indicating that the temperature profile was fairly sharp at the edge of the focal spot.

4.3.3.6 TIME INTEGRATED SPECTROSCOPY

An extra diagnostic which provided a variety of measurements was a time integrated miniature X-ray crystal spectrometer of the Bragg type (see Chapter 7 and ref. 103). It can provide time averaged measurements of the electron density and temperature and the ground state densities of the ions in the region of the ablation front. These were obtained by measurements of the Stark broadening (104) of the higher order resonance lines which are optically thin. It was found that the Stark width was a small proportion of the total line width and the errors introduced were large. This was partly due to the relatively low electron density with the relatively high emitter charge.

4.3.3.7 FARADAY CUPS

An array of up to 12 Faraday cups were placed at various angles around the target chamber wall (at a distance of 38 cm from the plasma) to obtain a measurement of the charge reaching

the chamber wall against time (see Fig. 4.8). An assumption about the charge to mass ratio (or using Thompson parabola measurements) yields a measurement of the mass. Integration over the angular distribution will give the total mass ablated.

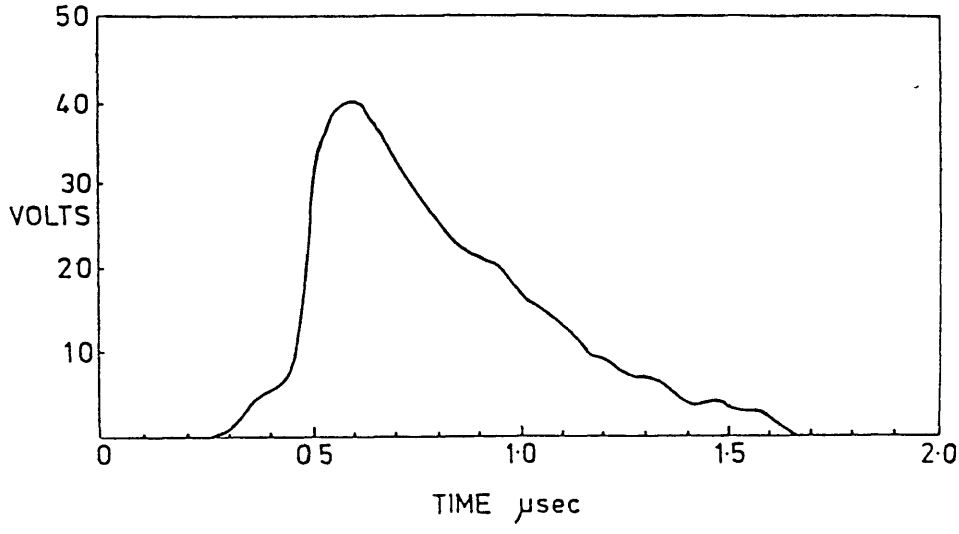


Fig. 4.8 FARADAY CUP SIGNAL

The charge time profile can be converted to a velocity spectrum of the ion which provides a characteristic velocity, being the peak of the distribution. A more useful value is that of the average ion velocity obtained by averaging over the distribution. For the distributions found in these experiments the two values were found to differ by a factor of ~0.9 (105) so the former was used as it was simpler to measure.

The total mass measured can be compared to the ablated mass measured by the X-ray diagnostics. This will then tell if most of the laser energy is deposited in the mass given by the X-ray measurements or not.

CHAPTER FIVE

MASS ABLATION RATES : RESULTS AND DISCUSSIONS

		Page
5.1	INTRODUCTION	74
5.2	BRIEF HISTORY OF EXPERIMENTS	74
5.3	MEASUREMENT ANALYSIS	78
5.3.1	TARGETS	78
5.3.2	LASER ENERGY	78
5.3.3	SPOT SIZE	78
5.3.4	BURN DELAY	83
5.3.5	CORRECTION FACTOR	84
5.4	DISCUSSION	87
5.4.1	LATERAL ENERGY TRANSPORT	89
5.4.2	EXPERIMENTAL REPRESENTATION	95
5.4.3	PRESSURE MEASUREMENT	99
5.5	WAVELENGTH SCALING	102
5.6	CONCLUSIONS	106

5.1 INTRODUCTION

This chapter will present the results of the mass ablation rate experiments and discuss some of the associated problems and ramifications. The mass ablation rates will be interpreted to provide ablation pressure measurements and their wavelength scalings.

5.2 BRIEF HISTORY OF EXPERIMENTS

The series of shots used to obtain the data presented in this section of the thesis were done in the period from November 1979 to March 1981 and formed a sequence over which experimental technique was steadily improved and altered as problems arose and effects were realised. Initial experiments with filter packs were unsuccessful.

Experiments with a Bragg crystal spectrometer on the streak camera combined with a change in the type of layered targets were successful. The targets consisted of aluminium deposited on the microscope slide in a vacuum coating plant. Other combinations were attempted (e.g. potassium chloride on titanium) but were found not to be as suitable (see Chapter 4) particularly from the diagnostic point of view.

The experiments at 0.35 μm used an f/2.5 fused silica lens limiting the spot size to 200 μm. It was found that inhomogeneities due to self focussing occurred.

During part of this run a slightly different target was used. Silicon monoxide was coated onto a thick aluminium substrate so that the target layers were essentially reversed. The lower energy resonance line (1 to 2 transitions) were used to observe the burn through.

The measurements and results are presented in Tables 5-1, 5-2 and 5-3 for 1.05 μm, 0.53 μm and 0.35 μm respectively, the individual measurements will be discussed in the next section and refer to these tables.

TABLE 5-1

1.05 μm MASS ABLATION RATE : EXPERIMENTAL DATA

Shot Number	Target Thickness Nominal (μm)	ρℓ (gm cm^{-2})	Laser Energy on Target (J)	Spot Diameter (μm)	Burn Delay (ps)	Correction Factor	Incident Intensity (10^{13} W cm^{-2})	Absorbed Intensity (10^{13} W cm^{-2})	Mass Ablation Rate (10^{5} gm cm^{-2} s^{-1})
291179/02	0.50	1.35	54.32	560	1600	1.15	1.41	0.96	0.97
291179/03	1.00	2.70	40.08	180	1900	1.17	12.01	5.92	1.66
291179/04	1.00	2.70	41.63	320	2700	1.27	3.29	2.01	1.27
291179/05	0.50	1.35	49.29	56	750	1.28	127.26	42.75	2.30
291179/08	0.50	1.35	66.53	90	890	1.22	66.50	23.86	1.85
291179/09	0.50	1.35	67.54	180	1200	1.16	16.87	7.78	1.31
291179/10	0.50	1.35	67.03	240	1110	1.17	9.42	4.88	1.42
291179/11	0.70	1.89	69.05	90	890	1.22	69.02	24.54	2.59
291179/12	0.70	1.89	65.52	90	960	1.20	65.49	23.49	2.36
291179/13	0.70	1.89	69.05	70	820	1.24	114.10	38.33	2.89
291179/14	0.25	0.68	65.52	180	1470	1.15	16.37	7.62	1.48
041279/01	0.50	1.35	56.95	320	690	1.30	4.50	2.60	1.27
061279/12	0.50	1.35	57.46	180	1200	1.16	14.36	6.82	1.31
061279/13	0.50	1.35	66.02	130	910	1.21	31.63	12.65	1.80
061279/15	0.70	1.89	54.43	56	960	1.20	140.54	46.48	2.36
030180/06	0.50	1.35	42.46	180	1090	1.18	10.65	5.43	1.46
040180/02	0.50	1.35	56.45	180	1050	1.18	14.11	6.75	1.52
040180/04	0.50	1.35	56.45	180	1200	1.16	14.11	6.75	1.31
040180/08	0.50	1.35	54.43	180	1090	1.18	13.60	6.55	1.46

TABLE 5-2

0.53 μm MASS ABLATION RATE : EXPERIMENTAL DATA

Shot Number	Target Thickness Nominal (μm)	ρℓ (gm cm^{-2})	Laser Energy on Target (J)	Spot Diameter (μm)	Burn Delay (ps)	Correction Factor	Incident Intensity (10^{13} W cm^{-2})	Absorbed Intensity (10^{13} W cm^{-2})	Mass Ablation Rate (10^{5} gm cm^{-2} s^{-1})
220780/04	0.4	1.38	5.33	110	480	1.18	10.01	7.78	3.39
220780/07	0.4	1.38	7.06	140	595	1.16	8.19	5.12	2.69
220780/09	0.2	0.49	3.53	140	305	1.34	4.09	3.30	2.14
230780/02	0.2	0.49	11.38	180	305	1.34	7.98	6.18	2.14
230780/03	0.2	0.49	8.93	320	400	1.23	1.98	1.71	1.49
230780/05	0.2	0.49	7.06	260	347	1.29	2.37	1.90	1.81
230780/07	0.2	0.49	11.07	210	245	1.45	5.71	4.61	2.88
230780/10	0.1	0.35	8.28	320	285	1.37	1.84	1.55	1.69
230780/11	0.1	0.35	5.76	260	305	1.34	1.94	1.90	1.54
240780/01	0.1	0.35	7.45	180	208	1.50	5.23	4.22	2.53
240780/13	0.4	1.62	13.68	120	415	1.22	21.60	15.78	4.76
240780/15	0.4	1.62	15.70	110	440	1.21	29.49	21.03	4.44
240780/17	0.4	1.62	16.78	80	400	1.23	59.60	40.48	4.98
240780/19	0.8	2.43	11.81	80	550	1.17	41.95	29.15	5.17
240780/21	0.8	2.43	13.46	56	418	1.22	97.62	63.85	7.09
280780/02	0.8	2.43	20.66	56	345	1.29	149.82	97.27	9.09
280780/05	0.8	2.43	10.44	50	440	1.21	94.95	62.48	6.45
290780/01	1.6	4.32	27.00	50	695	1.16	245.55	147.90	7.21
290780/02	1.6	4.32	19.22	46	703	1.16	206.56	131.37	7.13
290780/03	1.6	4.32	26.28	50	625	1.16	239.01	143.50	8.02
290780/11	1.6	4.05	24.77	50	740	1.17	225.25	136.90	6.40
290780/12	1.6	4.05	24.05	56	638	1.16	174.35	112.00	7.36
290/80/15	1.6	4.05	22.54	70	933	1.23	104.56	68.41	5.34
290780/22	1.6	4.32	24.05	110	933	1.23	45.19	31.37	5.70
300/80/01	0.1	0.27	19.87	280	218	1.48	5.76	4.61	1.83
300780/03	0.1	0.27	25.20	416	220	1.48	5.76	2.58	1.82
300780/06	0.1	0.27	23.54	620	242	1.44	1.39	1.19	1.61
300780/07	0.1	0.27	5.11	110	170	1.58	9.61	7.58	2.51
300/80/09	0.8	2.16	22.75	110	417	1.22	42.75	29.71	6.32
300780/11	0.8	2.16	19.58	110	438	1.21	36.79	25.79	5.94
310780/10	0.8	2.16	25.63	56	407	1.22	185.84	116.12	6.48

TABLE 5-3

0.35μm MASS ABLATION RATE : EXPERIMENTAL DATA

Shot Number	Target Thickness Nominal (μm)	ρℓ (gm cm^{-2})	Laser Energy on Target (J)	Spot Diameter (μm)	Burn Delay (ps)	Correction Factor	Incident Intensity (10^{13} W cm^{-2})	Absorbed Intensity (10^{13} W cm^{-2})	Mass Ablation Rate (10^{5} gm cm^{-2} s^{-1})
250281/08	1.0	4.32	3.91	42	605	1.15	38.72	33.00	8.21
250281/11	1.0	4.32	3.39	42	550	1.17	33.62	29.28	9.19
250281/12	1.0	4.32	3.83	46	550	1.17	31.68	27.10	9.19
250281/14	1.0	4.32	5.97	60	605	1.15	29.02	24.92	8.21
040381/04	1.0	2.70	5.30	64	495	1.19	22.03	19.83	6.49
040381/05	1.0	2.70	7.10	64	440	1.22	30.31	26.23	7.51
040381/12	0.4	2.16	6.60	52	385	1.26	42.68	36.45	7.04
050381/01 *	1.0	4.32	4.44	18	385	1.26	239.68	189.34	14.09
060381/02	0.7	1.49	2.29	31	275	1.40	41.61	35.37	7.18
060381/05	0.7	1.49	1.90	25	220	1.50	53.11	44.62	9.61
060381/06	0.7	1.49	0.35	33	330	1.31	5.59	4.81	5.60
060381/10	0.7	1.49	2.80	68	330	1.31	10.60	9.12	5.60
110381/01	0.7	1.49	5.02	76	275	1.40	15.18	13.06	7.13
110381/04	0.7	1.49	5.20	89	315	1.33	11.48	9.87	6.30
110381/05	0.7	1.49	3.31	50	253	1.44	23.19	19.94	8.03
110381/06	0.7	1.49	2.65	37	253	1.44	33.80	28.73	8.03
110381/07	0.7	1.49	1.79	36	231	1.47	24.13	20.51	8.97
110381/08	0.7	1.49	7.35	100	275	1.40	12.85	11.05	7.18
120381/03	1.0	2.13	2.14	34	385	1.26	32.33	27.48	6.94
120381/10	1.0	2.13	8.45	80	330	1.31	23.09	19.63	8.46
120381/12	1.0	2.13	6.38	41	303	1.35	66.40	56.44	7.92

* The two types of targets; Aℓ on glass and SiO on Aℓ are above and below the line respectively.

5.3 MEASUREMENT ANALYSIS

5.3.1 TARGETS

The target thicknesses presented are nominal values. The actual deposited value is given in the column for area mass density ($\rho\ell$) as measured by the peizo-electric deposition monitor.

5.3.2 LASER ENERGY

Energy losses were taken into account at 4% per surface due to transmission through the vacuum chamber window, the main lens and pellicle (if used). The figures shown in Tables 5-1 to 5-3 are the energies on the target surfaces.

5.3.3 SPOT SIZE

The diameter of this was measured from the X-ray pinhole camera data. Typical X-ray images and their densitometer traces are shown in Figs. 5.1 to 5.3. These show small focal spots (tight focus) (Figs. 5.1(a), 5.2(a) and 5.3(a)) and a comparison with the large focal spots (~200 μm diameter) (Figs. 5.1(b), 5.2(b) and 5.3(b)). Note the ring structures and beam break up (Fig. 5.3(b)) for the large focal spot at 0.35 μm. This sort of variation in the effective beam profile would lead to anomalous burn through so 0.35 μm shots with spot sizes of greater than 100 μm diameter were not used.

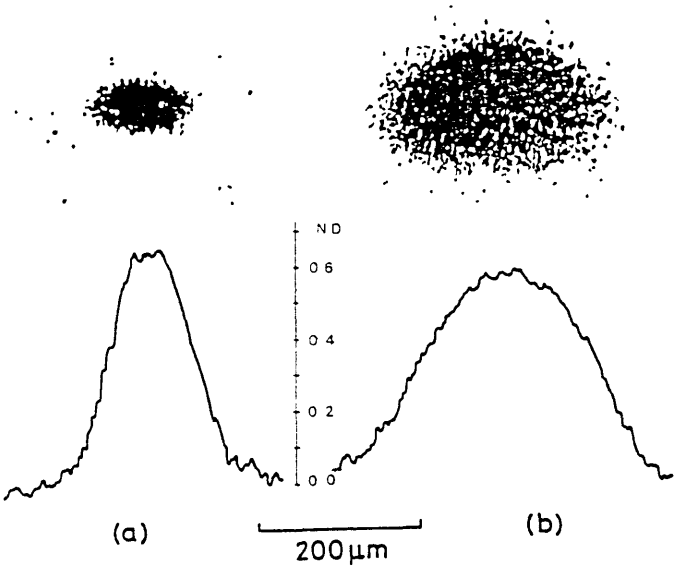


Fig. 5.1 1.05 µm X-RAY PINHOLE PICTURES
(a) TIGHT FOCUS
(b) 200 µm DIAMETER

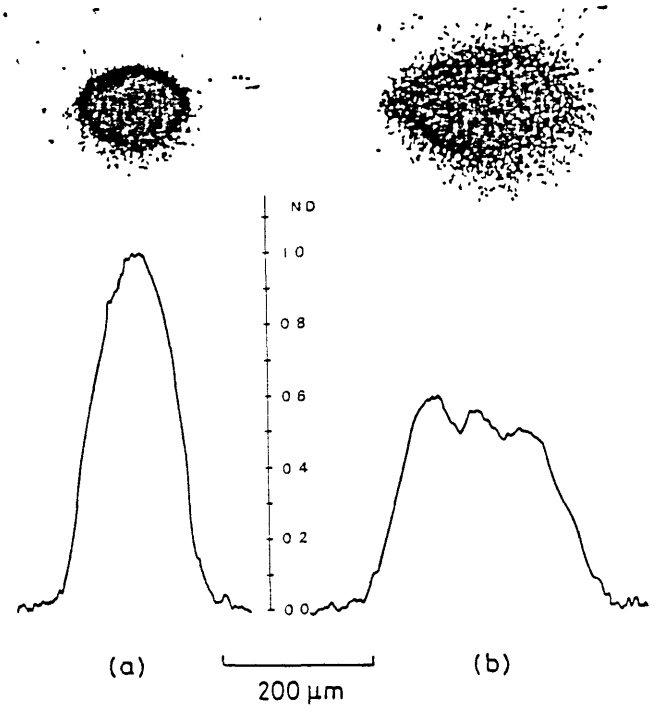


Fig. 5.2 0.53 µm X-RAY PINHOLE PICTURES
(a) TIGHT FOCUS
(b) 200 µm DIAMETER

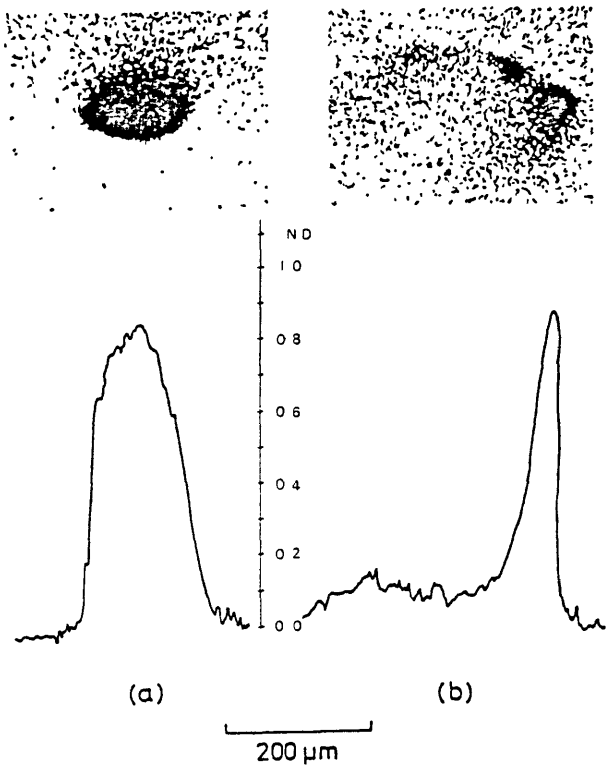


Fig. 5.3 0.35 µm X-RAY PINHOLE PICTURES
(a) TIGHT FOCUS
(b) 200 µm DIAMETER

For the 1.05 µm and 0.53 µm runs a plot of the full width at half maximum intensity of the pinhole images (after taking into account film response (102, Section 7.7)) was plotted against the lens defocussing (Figs. 5.4 and 5.5 respectively). This shows the effective f number of the beam as 1.9 except within 150 µm of the focal plane where there was a minimum diameter of 50 µm. There was little difference between the two channels of the pinhole camera as can be seen from the figures.

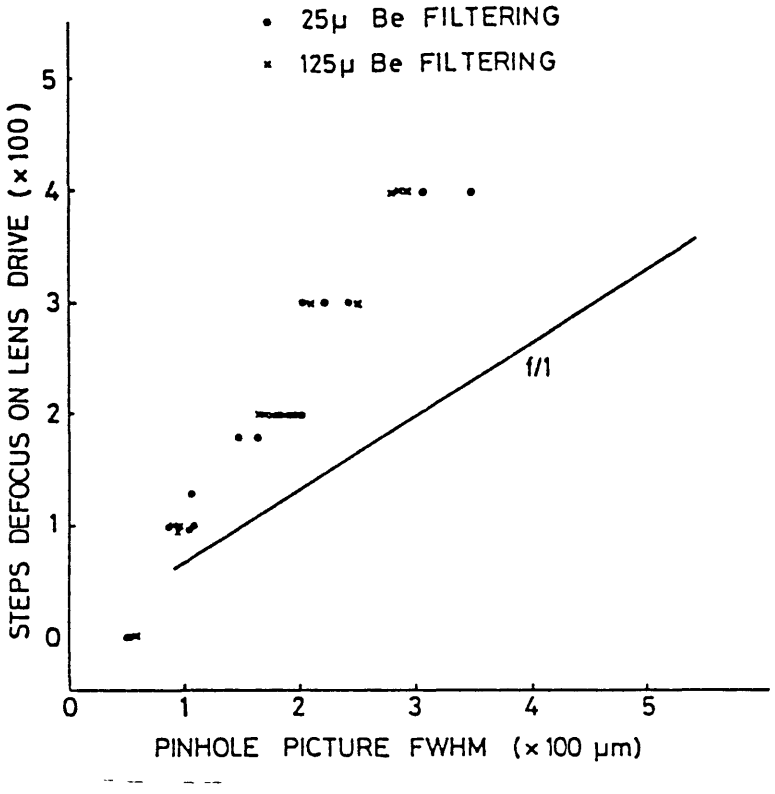


Fig. 5.4 1.05 μm; LENS DEFOCUS AGAINST MEASURED PINHOLE PICTURE SIZE

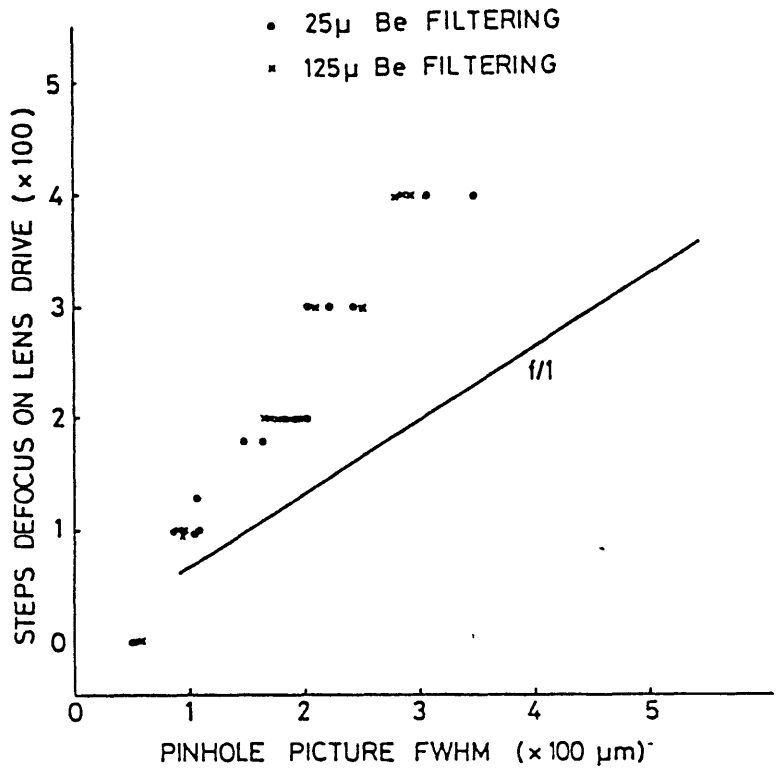


Fig. 5.5 0.53 μm; LENS DEFOCUS AGAINST MEASURED PINHOLE PICTURE SIZE

The spot sizes from these graphs were used in the analysis thus removing any irregularities in individual pinhole camera data, as the amount of defocus of each shot was measured to ±20 μm. This process could not be done for the 0.35 μm data due to the large f number of the lens and lens aberations, and the alignment laser was not the same wavelength as the pulse laser. The defocussing had a large error and the measured size from the pinhole camera had to be used. The scatter of data in the intensity measurements is correspondingly greater.

5.3.4 BURN DELAY

A typical streak is shown in Fig. 4.6 for the aluminium on glass targets. The simple measurement of burn-through was taken between the start of the dielectronic satellites (see Chapter 6)

of the Al XII $1s^2$-1s3p line and the dielectronic satellites and intercombination lines of the Si XIII $1s^2$-1s2p lines. The delay between the Al XIII 1s-4p and 1s-5p and the Si XIII $1s^2$-1s3p, was also used. These sets were chosen as they are spectrally adjacent and of similar intensity.

Figure 4.5 shows a streak taken for the silicon monoxide on aluminium targets and the delay is measured between the Si XIII $1s^2$-1s2p and the Al XIII 1s-2p and Al XII $1s^2$-1s2p.

The largest error in the measurements of t_B is the identification of the start of the lines, which usually introduced a 50 ps error.

5.3.5 CORRECTION FACTOR

This was calculated as discussed in Chapter 4 using the time history of the laser pulse recorded by the optical streak camera. This then had to be approximated so that the integration could be done. The initial approximation used was of a gaussian. Although this closely resembled the laser pulse (particularly for the 1.05 μm case) it proved difficult to use because it had no well defined starting point. Even if the peak of the laser pulse and the emission continuum (which was short-lived) were matched it was found that on integration a substantial part of energy occurred well before the start of any X-ray emission (particularly if the integrand is raised to the scaling power of α, see Chapter 4). A trapezium was finally decided upon as it matched the shape of the laser pulse reasonably well and had a well defined starting point.

For the use of a correction factor of this sort to be valid the start of the X-ray emission (as detected) must coincide with the start of the laser pulse and not be significantly delayed. This was checked by comparing the laser pulse shape with the shape of the recombination continuum of aluminium XII and XIII ions (see Fig. 4.6). This continuum is relatively short lived

and a densitometer trace in the temporal direction (Fig. 5.6) showed that rise time (t_r) corresponds to that of the laser pulse. Moreover being of similar shape the time from start to maximum is similar. This indicates that for the purposes of this experiment the laser pulse and the detectable X-ray emission start at approximately the same time and the use of the correction factor is reasonable.

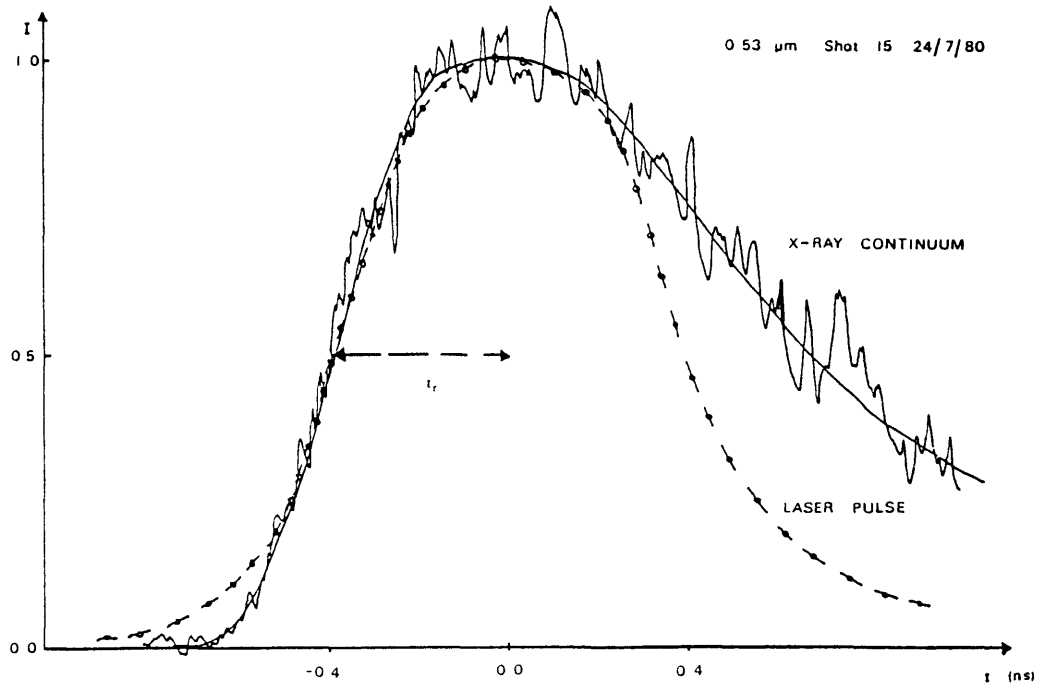


Fig. 5.6 COMPARISON OF THE X-RAY CONTINUUM AND LASER PULSE TIME PROFILES

Typical laser pulses with their fits are shown in Fig. 5.7. A graph of the calculated correction factors against burn time is shown in Fig. 5.8.

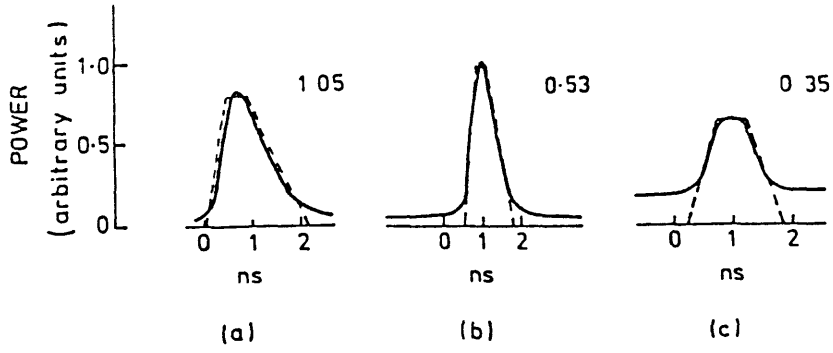


Fig. 5.7 LASER PULSE SHAPES AND TRAPEZOIDAL FITS
(a) 1.05 μm
(b) 0.53 μm
(c) 0.35 μm

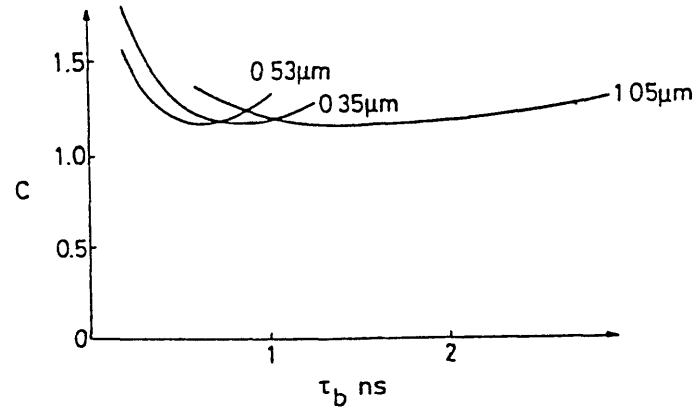


Fig. 5.8 CALCULATED CORRECTION FACTORS AGAINST BURN TIME

5.4 DISCUSSION

Once the above variables have been quantified for each shot, calculation of the required parameters was relative easy. The incident intensity is described by Equation 4.11 ($\int f(t)\,dt$ simply being the full width at half maximum intensity of the laser pulse for the trapezoidal fit). This was converted to an absorbed intensity (as only absorbed energy can go into ablation) by using a combination of absorption measurements from other laboratories for similar laser conditions (106-108) a best fit to the data is shown in Fig. 5.9.

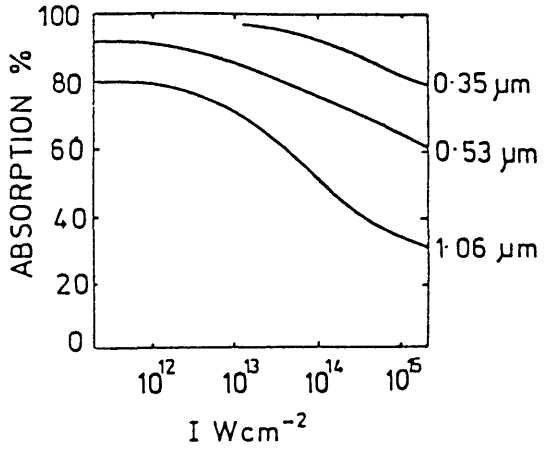


Fig. 5.9 ABSORPTION FRACTION AGAINST INCIDENT IRRADIANCE FOR THE THREE LASER WAVELENGTHS

Figure 5.10 is a graph of mass ablation rate against incident intensity for all three laser wavelengths. Least squares fits to these give for 1.05 μm

$$\dot{m}_{1.05} = (0.87 \pm 0.06) \times 10^5 \left(\frac{I_o\ (W\ cm^{-2})}{10^{13}}\right)^{0.21\pm0.02} \text{gm cm}^{-2}\ \text{s}^{-1} \qquad 5.1$$

for 0.53 μm

$$\dot{m}_{0.53} = (1.35 \pm 0.08) \times 10^5 \left(\frac{I_o\ (w\ cm^{-2})}{10^{13}}\right)^{0.33\pm0.02} \text{gm cm}^{-2}\ \text{s}^{-1} \qquad 5.2$$

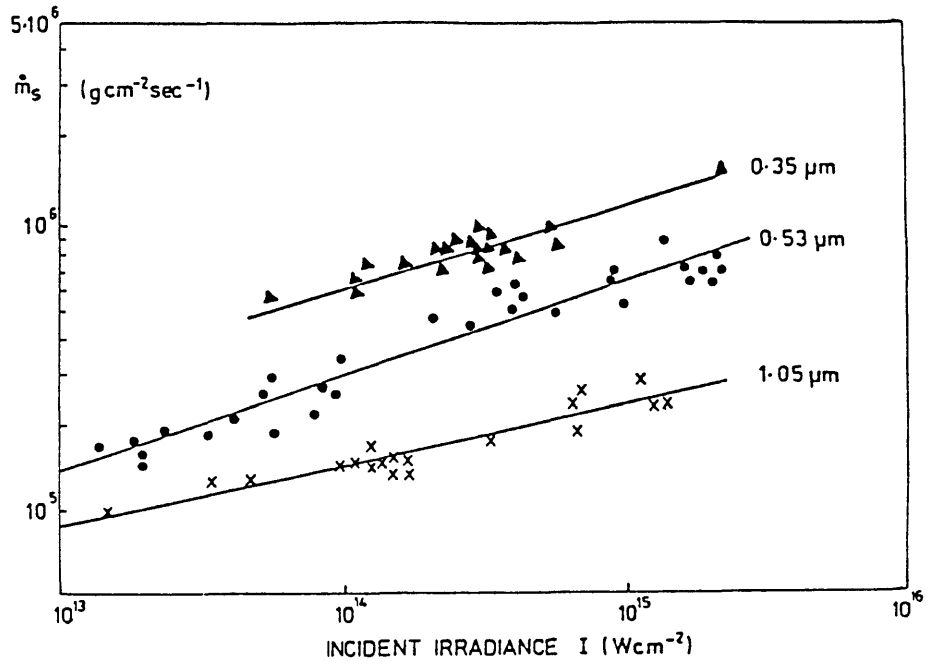


Fig. 5.10 MASS ABLATION RATES AGAINST INCIDENT IRRADIANCE FOR THE THREE LASER WAVELENGTHS

and for 0.35 μm

$$\dot{m}_{0.35} = (3.08 \pm 0.69) \times 10^5 \left(\frac{I_o \text{ (W cm}^{-2})}{10^{13}}\right)^{0.29\pm0.06} \text{gm cm}^{-2} \text{ s}^{-1} \qquad 5.3$$

In Fig. 5.11 the absorption fractions (Fig. 5.9) have been included to produce a graph of mass ablation rate against absorbed irradiance. Least squares fits to these give

$$\dot{m}_{1.05} = (0.94 \pm 0.06) \times 10^5 \left(\frac{I_a \text{ (W cm}^{-2})}{10^{13}}\right)^{0.26\pm0.03} \text{gm cm}^{-2} \text{ s}^{-1} \qquad 5.4$$

$$\dot{m}_{0.53} = (1.40 \pm 0.08) \times 10^5 \left(\frac{I_a \text{ (W cm}^{-2})}{10^{13}}\right)^{0.36\pm0.03} \text{gm cm}^{-2} \text{ s}^{-1} \qquad 5.5$$

$$\dot{m}_{0.35} = (3.1 \pm 0.7) \times 10^5 \left(\frac{I_a\ (W\ cm^{-2})}{10^{13}}\right)^{0.31\pm0.06} gm\ cm^{-2}\ s^{-1} \qquad 5.6$$

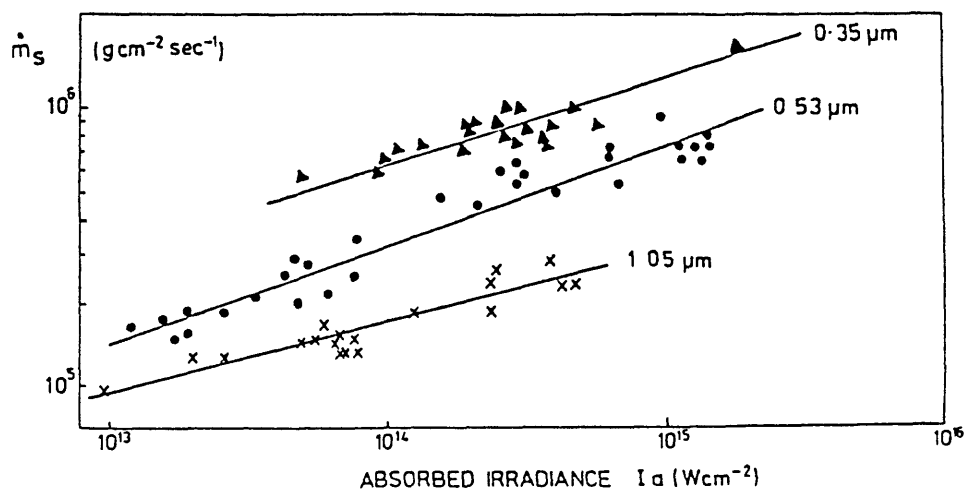


Fig. 5.11 MASS ABLATION RATES AGAINST ABSORBED IRRADIANCE FOR THE THREE LASER WAVELENGTHS

5.4.1 LATERAL ENERGY TRANSPORT

Figure 5.12 shows the variation of velocity, calculated from the peak of ion collecton signals (see Fig. 4.8), with absorbed irradiance for each of the three laser wavelengths. Least squares fitting gives

$$v_p^{1.05} = (6.7 \pm 0.3) \times 10^7 \left(\frac{I_a\ (W\ cm^{-2})}{10^{13}}\right)^{0.06\pm0.02} cm\ s^{-1} \qquad 5.7$$

$$v_p^{0.53} = (4.6 \pm 0.2) \times 10^7 \left(\frac{I_a\ (W\ cm^{-2})}{10^{13}}\right)^{0.11\pm0.02} cm\ s^{-1} \qquad 5.8$$

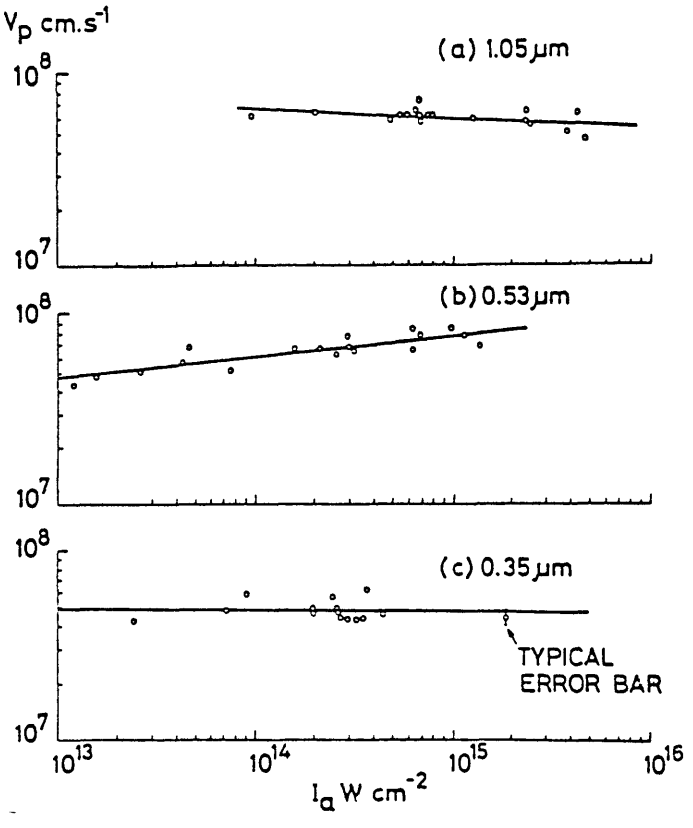


Fig. 5.12 ION VELOCITY (AT THE PEAK OF THE DISTRIBUTION) AGAINST ABSORBED IRRADIANCE
(a) 1.05 μm
(b) 0.53 μm
(c) 0.35 μm

and

$$v_p^{0.35} = (4.9 \pm 0.6) \times 10^7 \left(\frac{I_a \text{ (W cm}^{-2})}{10^{13}}\right)^{0.0\pm0.02} \text{ cm s}^{-1} \qquad 5.9$$

Also from the data a measure of the ablated mass (105) can be obtained (see Section 4.3.3.7). Figure 5.13 shows this value relative to the ablated mass as measured by the X-ray diagnostics normalised to the laser energy and plotted against absorbed irradiance. It is notable that this normalised relative mass is essentially independent of I_a for 1.05 μm but decreases for increasing I_a for 0.53 μm and 0.35 μm.

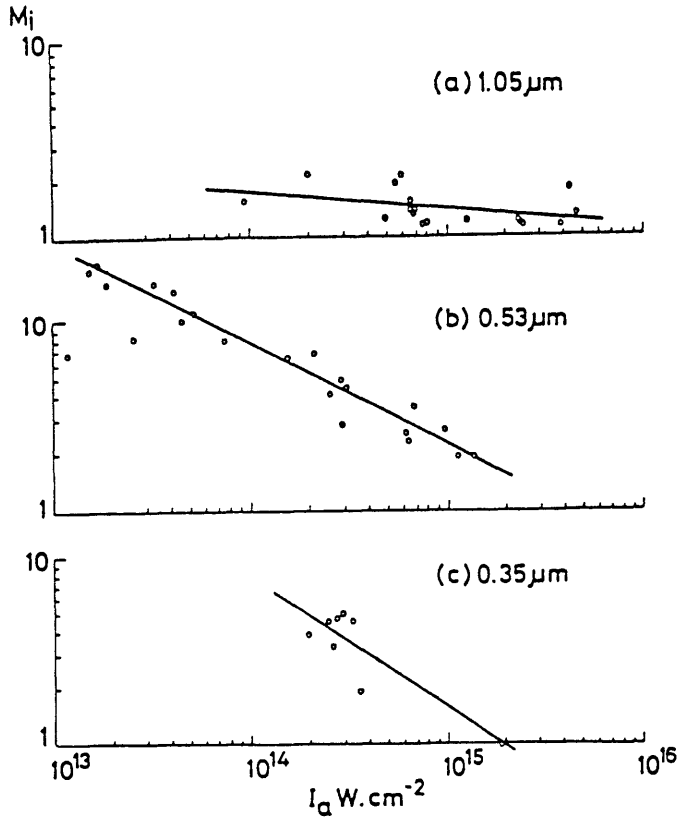


Fig. 5.13 RELATIVE MASS AGAINST ABSORBED IRRADIANCE
(a) 1.05 μm
(b) 0.53 μm
(c) 0.35 μm

The angular variations as measured by the Faraday cups showed a greater spreading of the ion plume for higher irradiances at 0.53 μm (small spot size) whilst at low irradiances a $\cos^4 \theta$ dependence was found. Similar measurements at 1.05 μm showed no such spreading. Work done by Lewis et al (109) following earlier suggestions (110) found that to a good approximation

$$v_p(\theta) = v_p \cos^2 \theta \qquad 5.10$$

and

$$n(\theta) = n_p \cos^4 \theta \qquad 5.11$$

where

$v_p(\theta)$ - the ion velocity at the current peak

$n(\theta)$ - the number of ions per steradian.

The measurements conducted during these experiments, though less detailed, are broadly consistent. From these angular distribution functions angular averages are obtained of

$$\langle v_p(\theta) \cos \theta \rangle = B v_p \qquad 5.12$$

$$\langle v_p^2(\theta) \rangle = c v_p^2 \qquad 5.13$$

with B = 0.66 and c = 0.6.

The experimental results can be represented by

$$\dot{m} = \dot{m}_K I_a^x \qquad 5.14$$

$$v_p = v_K I_a^y \qquad 5.15$$

where the constants $\dot{m}_K$, v_K, x and y depend on wavelength. The ratio of the power flow per unit area in the ablation for the high temperature focal spot, of area A_s, (as measured by the pinhole camera) to the absorbed irradiance I_a is

$$0.5 \frac{\dot{m} < v_p^2(\theta) >}{I_a} = 0.5\ C\ \dot{m}_K\ v_K^2\ I_a^{(x+2y-1)} \qquad 5.16$$

When this ratio is 1 all the absorbed power goes into ablation. This occurs at an irradiance of

$$I_o = (0.5\ C\ \dot{m}_K\ v_b^2)^{\left(\frac{1}{1-x-2y}\right)} \qquad 5.17$$

The values of I_o, $(x+2y-1)$ and the corresponding focal spot diameter, ϕ_o, which gives I_o as the absorbed power, are given in Table 5-4.

TABLE 5-4

PARAMETERS I_o, ϕ_o WHEN LATERAL ENERGY TRANSPORT IS NEGLIGIBLE. THE EXPONENT $(x + 2y - 1)$ SHOWS INCREASING ENERGY INTO LATERAL TRANSPORT FOR $\phi<\phi_o$ OR $I>I_o$

$\lambda(\mu m)$	$I_o/10^{-13}$ (W cm^{-2})	$x + 2y - 1$	ϕ_o (μm)
1.05	1.30	-0.86	511
0.53	0.75	-0.42	599
0.35	3.20	-0.69	163

The negative values of the exponent show that for $I_a>I_o$ as I_a increases less of the absorbed energy goes into ablation from the area A_s. For $I_a<I_o$ the scaling law would change so that the power flow in the ablating material would not exceed the absorbed irradiance. Experiments with spherical targets (111,112) and large focal spots with low irradiances (113) do show a stronger scaling with $x \sim 0.6$ and $y \sim 0.2$.

A measure of the energy in the ablated material (not just from A_s) can be obtained from Figs. 5.12 and 5.13 by $E_i \propto M_i v_p^2$ and is found to scale as $I_a^{-0.2}$, $I_a^{-0.3}$ and $I_a^{-0.7}$ for λ = 1.05, 0.53 and 0.35 μm respectively. This can be compared with the total absorbed energy which is proportional to $A(I_a)$ (see Fig. 5.9). If these two scalings are the same then most of the absorbed energy ends up in ablating material. For these experiments this appeared to be true for the 1.05 μm and 0.53 μm but the 0.35 μm results were inconsistent and may be inaccurate.

It was originally thought that the apparent energy losses could be attributed to fast electrons and ions of the kind generated by high intensity short laser pulses (see Chapter 1). Recent work (114) has been shown that in long pulse high intensity experiments fast electrons are generated and preheat the target over a large area with a narrow jet of fast ions emitted normal to the target. This effect is however insufficient to explain the energy losses, as are the thermal radiation losses.

Evidence of ablation from an area greater than A_s (and therefore of lateral energy flow) has been provided by Lewis et al (109) by measurements of v_p with respect to the optical focal spot diameter at constant irradiance (110). They found

$$v_p = 5 \times 10^7 \left(\frac{I \ (W \ cm^{-2})}{10^{13}}\right)^{0.2} \left(\frac{\phi \ \mu m}{200}\right)^{0.3} cm \ s^{-1} \qquad 5.18$$

Using typical values of the present experiments where $I \phi^2$ was constant (~10 J in 1.7 ns at 1.05 μm)

$$v_p = 6.9 \times 10^7 \left(\frac{I \ (W \ cm^{-2})}{10^{13}}\right)^{0.033} \qquad 5.19$$

which is consistent with the low scaling of our measurements. As the work of Lewis shows similar effects it may be concluded that the spot size mainly determines the proportion of power transmitted outside the focal spot region for the case, here, of approximately constant laser energy.

The lateral energy flow varies with laser wavelength as is shown by changes in ϕ_o but it is unclear from the data what the scaling might be though it would appear to be between 0 and 3.

5.4.2 EXPERIMENTAL REPRESENTATION

From the above discussion it would appear that the whole effect can be represented by two areas of ablation. A central one characterised by the high temperture focal spot and an outer annulus whose presence shows up as a large number of slow ions which dominate the ion signal, swamping out the much faster but less numerous ions from the high temperature region. This can be illustrated as in Fig. 5.14. The inner part has parameters I_i, ϕ_i, v_i, $\dot{m}_i$ for irradiance, diameter, ion velocity and mass ablation rate with similar parameters I_r, ϕ_r, v_r, $\dot{m}_r$ for the outer ring (I_r is the apparent effective irradiance).

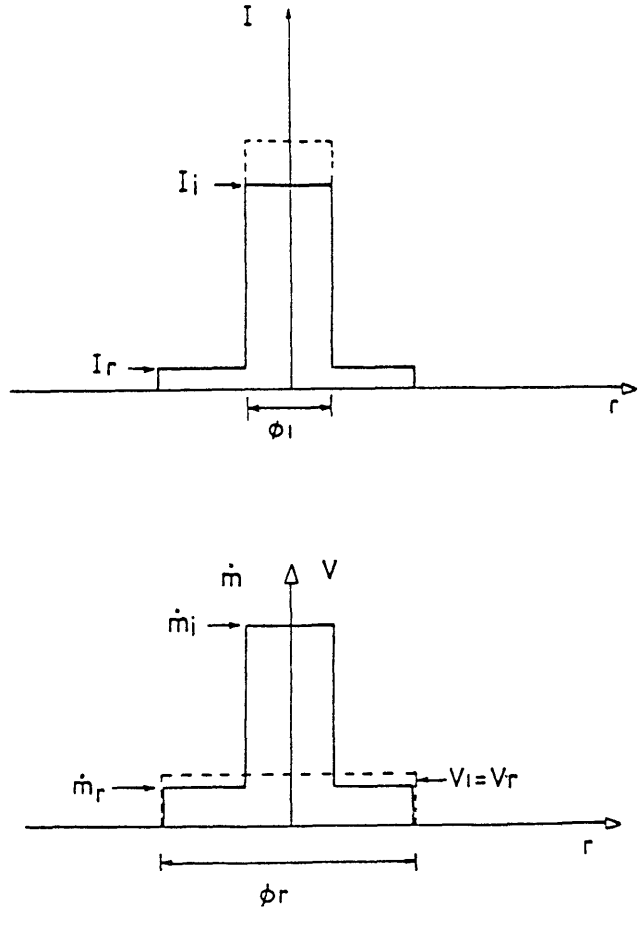


Fig. 5.14 REPRESENTATION OF PLANAR ABLATION WITH FOCAL SPOT AND OUTER ANNULUS

From this representation we can derive the magnitude and spatial distribution of the ablation parameters. Experiments without 'edge' effects, e.g. on spherical targets and with large focal spots, suggest (112)

$$\dot{m}_\infty \propto I_a^{0.6} \tag{5.20}$$

$$v_\infty \propto I_a^{0.2} \tag{5.21}$$

It is reasonable to assume that these scalings will hold for the inner and outer regions that are being considered as each region is separate with no lateral energy flows.

Using our values of I_o where there is no lateral energy flow to get the constant in Equations 5.20 and 5.21 using Equations 5.14 and 5.15

$$\dot{m}_\infty = \dot{m}_K I_o^{x} \left(\frac{I_a}{I_o}\right)^{0.6} \tag{5.22}$$

and

$$v_\infty = v_K I_o^{y} \left(\frac{I_a}{I_o}\right)^{0.2} \tag{5.23}$$

The coefficients, $\dot{m}_K I_o^{(x-0.6)}$, $v_K I_o^{(y-0.2)}$ are given in Table 5-5 and their scaling with wavelength can be compared with the

TABLE 5-5

PROPORTIONALITY CONSTANTS n_x and v_x ASSUMING SCALING SIMILAR TO THE SPHERICAL ABLATION EXPERIMENTS (112)

$\lambda(\mu m)$	m_k $(I_o/10^{13}$ W cm$^{-2})^{x-0.6}$ 10^5 gm cm^{-2} s^{-1}	v_k $(I_o/10^{13}$ W cm$^{-2})^{y-0.2}$ 10^7 cm s^{-1}
1.05	0.86	6.2
0.53	1.50	4.7
0.35	2.20	3.9

analytic models of Chapter 3. The scaling is

$$\dot{m} \propto \lambda^{-0.85} \qquad 5.24$$

$$v_p \propto \lambda^{0.42} \qquad 5.25$$

which gives the -2:1 ratio of the wavelength power dependencies shown by the sonic point deflagration models (Equations 2.12, 2.13 and reference 48). The actual magnitude of the powers lie somewhat between the self regulating absorption model (Equations 2.24, 2.25 and reference 52) and the critical density model (Equations 2.12, 2.13 and reference 48) but agree closely with that of Max Mckee and Mead (Equations 2.29, 2.30 and reference 56). Although agreement of these coefficients appears to be good with the latter model this may be fortunate as the irradiance scaling of $\dot{m}$ and v_p differs somewhat and the model does not take into account inverse Bremsstrahlung which is known to be important over the conditions of the experiment (33). The scaling is better described by the self regulating absorption model (Equations 2.24, 2.25).

The observed scaling of v_p can give values of the diameter of the outer ring and its effective irradiance in the limit of a small focal spot so that the majority of the energy ends up in the annulus. Then the velocity given by the peak ion signal will be

$$v_K \, I_o^{(y-0.2)} \, I_r^{0.2} = v_K \, I_a^{y} \qquad 5.26$$

or

$$I_r = I_o \left(\frac{I_a}{I_o}\right)^{5y} \qquad 5.27$$

giving

$$\phi_r = \phi_o \left(\frac{I_o}{I_a}\right)^{2.5y} \left(\frac{A(I_o)}{A(I_a)}\right)^{0.5} \qquad 5.28$$

where

A(I) - the absorption fractions.

In a similar fashion the effective irradiance of the inner region can be derived from the observed scaling of $\dot{m}$

$$\dot{m}_K \, I_o^{(x-0.6)} \, I_i^{0.6} = \dot{m}_K \, I_a^{x} \qquad 5.29$$

giving

$$I_i = I_o \left(\frac{I_a}{I_o}\right)^{\left(\frac{x}{0.6}\right)} \qquad 5.30$$

These values of I_i and I_r give the extent of the differences between the two regions (i.e. the lateral energy spread). Taking the ratio of Equations 5.27 and 5.30

$$\frac{I_i}{I_r} = \left(\frac{I_a}{I_o}\right)^{\left(\frac{x}{0.6} - \frac{y}{0.2}\right)} \qquad 5.31$$

The magnitude of the quantities I_i, I_r, $\phi_i=\phi_r$, ϕ_r, $\dot{m}_i=\dot{m}$, $\dot{m}_r$, v_i, $v_r=v_p$ and the extrapolated limiting values of $\dot{m}_\infty$ and v_∞ for $I_A = 10^{15}$ W cm^{-2} are shown in Table 5-6. From this the scaling of the associated range of the lateral energy spread, ϕ_r, with wavelength can be gauged

TABLE 5-6

ABLATION PARAMETERS AT $I_a = 10^{15}$ W cm^{-2}

λ (μm)	$\dot{m}_\infty$ (10^5 gm cm^{-2} s^{-1})	$\dot{m}$ (10^5 gm cm^{-2} s^{-1})	$\dot{m}_r$ (10^5 gm cm^{-2} s^{-1})	v_∞ (10^7 cm s^{-1})	v_i (10^7 cm s^{-1})	v_p (10^7 cm s^{-1})	I_i/I_a	I_r/I_a	ϕ_r(μm)
1.05	14	3.1	0.5	16.0	9.5	5.1	0.085	0.035	695
0.53	24	7.3	6.3	12.0	7.6	7.6	0.140	0.110	132
0.35	35	13.0	4.4	9.8	4.9	4.9	0.190	0.032	153

$$\phi_r \propto \lambda^{\beta} \qquad 5.32$$

where β is about 1.5 for the 1.05 μm to 0.35 μm range and 2.5 for the 1.05 μm to 0.53 μm range. The latter figure is thought more reasonable as the focal spot characteristics of the 0.35 μm data were less well defined.

The causes of the lateral energy flow are uncertain and the disparity of the parameters in the inner and outer region for 1.05 μm but not for 0.53 μm indicate different mechanisms coming into play. It is probable that a surface plasma created by processes such as energy deposition by hot electrons and thermal X-rays aids the heat transport, alternatively energy transport by radiation might be important but these experiments give no indications of the causes.

5.4.3 PRESSURE MEASUREMENTS

A measure of the ablation pressure can be obtained by simple momentum conservation

$$P = \dot{m} < v_p(\theta) \cos\theta > \qquad 5.33$$

where $< v_p \cos\theta >$ is the average ion velocity over angle from the target normal. Also

$$I_A = 0.5 \dot{m} < v_p(\theta)^2 > \qquad 5.34$$

where $< v_p(\theta)^2 >$ is an angular average over all the ions. By combining Equations 5.33 and 5.34 using Equations 5.12 and 5.13

$$P = (2 \dot{m} I_a)^{0.5} \frac{< v_p(\theta) \cos\theta >}{< v_p(\theta)^2 >^{0.5}} = (2 \dot{m} I_a)^{0.5} BC^{-0.5} \qquad 5.35$$

At the point where lateral energy conduction is neglected, i.e. I_o we can get an experimental value of P_∞

$$P_\infty (I_o) = B \dot{m}(I_o) v_p(I_o) = BC^{-0.5} (2 \dot{m} I_a)^{0.5} \qquad 5.36$$

P_∞ cannot be deduced for other values of I_a but if we use the scaling for the spherical data (Equations 5.20 and 5.21) then

$$P_\infty = P_\infty(I_o)\left(\frac{I_a}{I_o}\right)^{0.8} = K_\infty\left(\frac{I_a\ (W\ cm^{-2})}{10^{13}}\right)^{0.8} \qquad 5.37$$

The values of K_∞ (and Z, the scaling) are shown in Table 5-7 for the three laser wavelengths. The wavelength scaling would

TABLE 5-7

ABLATION PRESSURE DEFINED BY K AND Z FOR THE LIMITING CASES (SEE TEXT)

λ(μm)	P_∞		$P_{\infty\ell}$		P_i		$P_{i\ell}$		P_r	
	K	Z	K	Z	K	Z	K	Z	K	Z
1.05	3.5	0.8	3.7	0.63	4.0	0.35	4.1	0.20	4.0	-0.12
0.53	4.6	0.8	4.5	0.68	4.3	0.48	4.2	0.40	4.4	0.22
0.35	5.6	0.8	6.7	0.66	8.9	0.41	9.9	0.31	8.9	0.00

appear to be $P_\infty \propto \lambda^{-0.42}$. This agrees with the Max Mckee Mead model (Equation 2.31) but is stronger than the self regulating model (Equation 2.26) which would appear to be more appropriate. The Max Mckee Mead model gives a coefficient of approximately 0.5 of the value of the experimental results but it includes a factor of this magnitude to account for spherical geometry which may not be appropriate here. The simple critical density model (Equation 2.14) gives a pressure coefficient close to the experimental value but predicts a much stronger scaling $P_\infty \propto \lambda^{-0.67}$ though the irradiance scaling is close to the model prediction (Equation 2.14).

If irradiance scaling is not assumed, a lower bound estimate can still be obtained

$$P_{\infty\ell} = BC^{-0.5} \quad (2\ \dot{m}\ I_a)^{0.5} \qquad 5.38$$

by using the experimental values of $\dot{m}$ and I_a. The results are shown in Table 5-7 and suggest $P_\infty \propto \lambda^{-0.28}$ in the range 1.05 μm to 0.53 μm and $I_a = 10^{13}$ W cm^{-2} there is no 0.35 μm data at this irradiance and extrapolation is unreliable. This scaling is close to the value of $\lambda^{-0.22}$ predicted by the inverse Bremsstrahlung absorption model (Equation 2.26).

The differences between the estimated scaling of P_∞ and the experimental values of $P_{\infty\ell}$ is reduced due to the appearance of $\dot{m}$ to the power of 0.5. The observed value decreases from the value with zero lateral energy flow as I_a/I_o increases and the ratio of the pressures $P_\infty : P_{\infty\ell}$ goes to 2 at $I_a = 10^{15}$ W cm^{-2}.

Considering the higher temperature focal spot, the pressure generated can be estimated from

$$P_i = C\ \dot{m}\ v_i = BC^{-0.5}\ (2\ m\ I_i)^{0.5} \qquad 5.39$$

With the result shown in Table 5-7 which relies on the assumed scaling of I_i and v_i, as before a lower bound can be obtained direct from the experimental results

$$P_{i\ell} = B\ \dot{m}\ v_p \qquad 5.40$$

These results are also included in Table 5-7. This uses the velocity taken from the peak of the ion current which for cases of appreciable lateral energy transport is largely due to ions from the outer region which move at a lower velocity. In the case at 1.05 μm and high intensity the ratio $v_i : v_p$ can be 2.

Finally the ablation pressure in the outer region can be estimated

$$P_r = B\ \dot{m}_r\ v_p = BC^{-0.5}\ (2\ \dot{m}_r\ I_r)^{0.5} \qquad 5.41$$

The results are included in Table 5-7. This is only well defined at high values of I_a/I_o where the total energy spread is great, it again depends on the assumed scaling from the spherical cases.

5.5 WAVELENGTH SCALING

From the above discussion we can see the significance of laser wavelength when compression of inertial fusion targets is attempted by ablation. For this consideration we want to compare the values at the same incident irradiance as the absorption fraction will be inherent in the use of a particular wavelength. From Table 5-8 where the values are set out for the incident

TABLE 5-8

ABLATION PRESSURE (Mb) CALCULATED FROM TABLE 5-7 AND FIG. 5.9 FOR VALUES $I = 10^{14}$ W cm^{-2} AND $I\lambda^2 = 10^{14}$ W cm^{-2} μm^2

λ(μm)	$I = 10^{14}$ W cm^{-2}				$I\lambda^2 = 10^{14}$ W cm^{-2} μm^2			
	P_∞	$P_{\infty\ell}$	P_i	$P_{i\ell}$	P_∞	$P_{\infty\ell}$	P_i	$P_{i\ell}$
1.05	13	10	7	6	13	10	7	6
0.53	23	18	11	9	65	31	21	16
0.35	32	29	22	20	182	121	53	38

irradiance of $I_o = 10^{14}$ W cm^{-2} we get

$$P_\infty \propto \lambda^{-0.8} \qquad 5.42$$

$$P_{\infty\ell} \propto \lambda^{-1} \qquad 5.43$$

$$P_i \propto \lambda^{-1} \qquad 5.44$$

$$P_{i\ell} \propto \lambda^{-1.1} \qquad 5.45$$

A preferred view may be to keep a constant hot electron temperature and hence preheating range by keeping $I\lambda^2$ constant (115). Doing this for $I\lambda^2 = 10^{14}$ W cm^{-2} μm^2, which is an appropriate upper limit for ablative implosions for small (~100 μm diameter) targets, gives from Table 5-8

$$P_{\infty} \propto \lambda^{-2.4} \qquad 5.46$$

$$P_{\infty \ell} \propto \lambda^{-2.3} \qquad 5.47$$

$$P_{i} \propto \lambda^{-1.8} \qquad 5.48$$

$$P_{i\ell} \propto \lambda^{-1.7} \qquad 5.49$$

The circa λ^{-2} scaling of the maximum driving pressure is a strong argument in favour of shorter laser wavelength for ablative implosion, although it is mainly a coincidence of making $I \propto \lambda^{-2}$.

Figures 5.15, 5.16 and 5.17 show the comparison with other

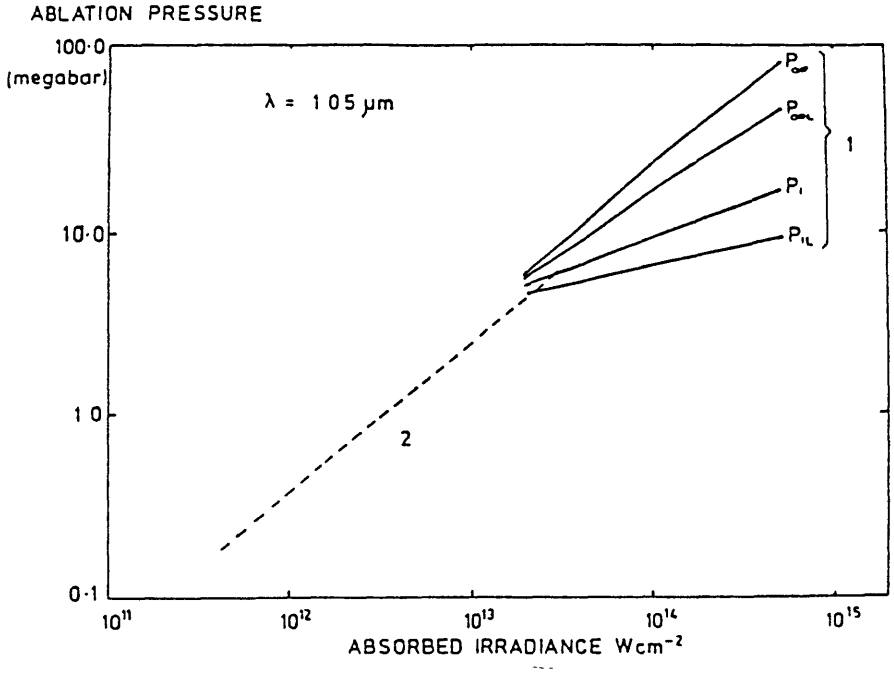


Fig. 5.15 1.05 μm ABLATION PRESSURE RESULTS
(1) PRESENT RESULTS
(2) ION EMISSION AND RECOIL MOMENTUM MEASUREMENTS (see Fig. 3.2)

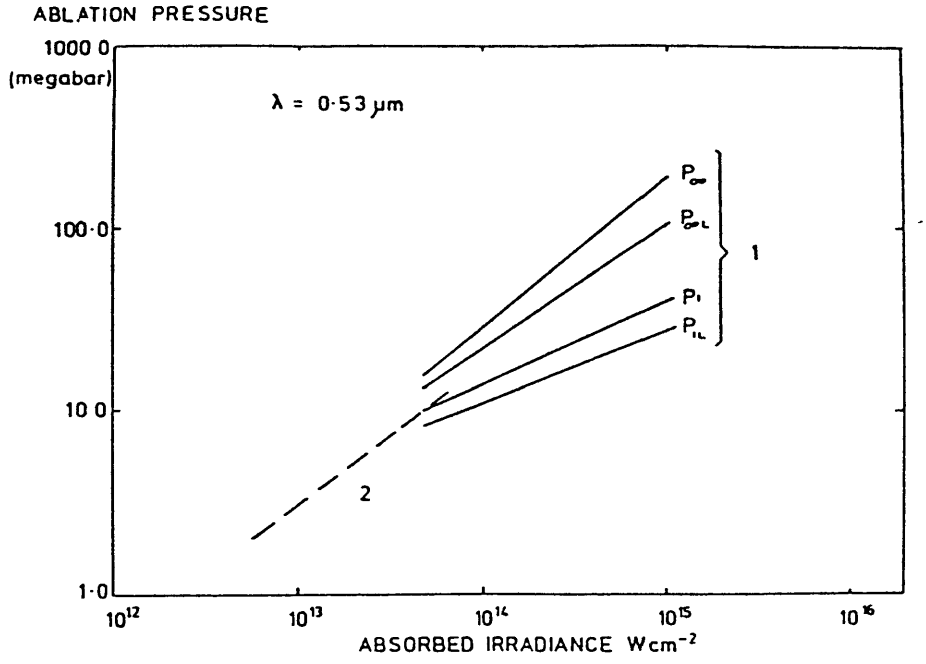


Fig. 5.16 0.53 μm ABLATION PRESSURE RESULTS
(1) PRESENT RESULTS
(2) SPHERICAL PRESSURE MEASUREMENTS (14)

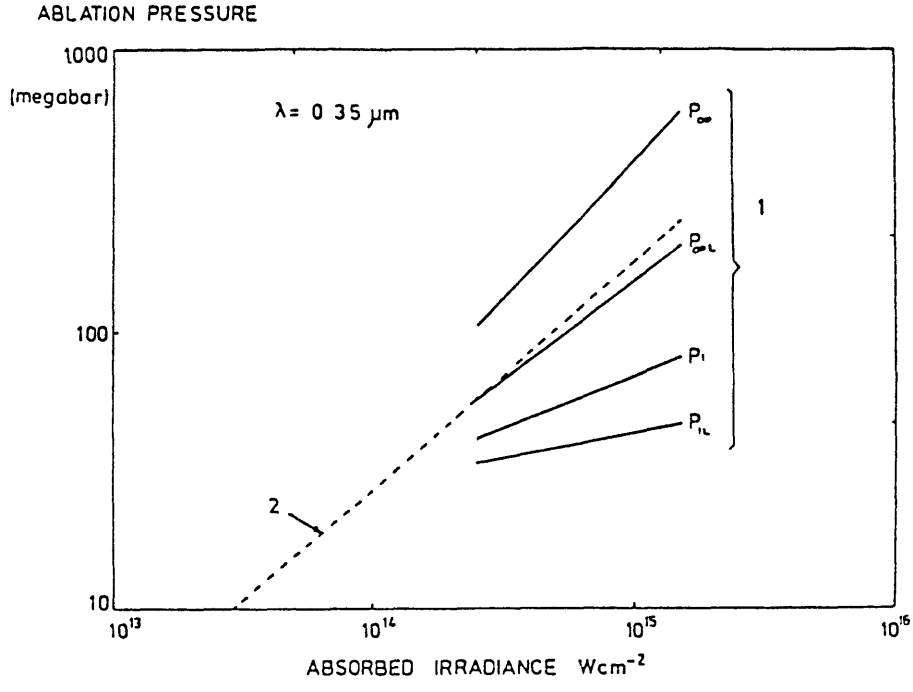


Fig. 5.17 0.35 μm ABLATION PRESSURE RESULTS
(1) PRESENT RESULTS
(2) $P_{\infty \ell}$ INFERRED FROM MASS ABLATION DATA (116)

data. In Fig. 5.15 for 1.05 μm data there is ion and recoil momentum data (for focal spots in the irradiance range 5 x 10^{11} to 3 x 10^{13} W cm^{-2}). It would appear that the values of pressure obtained in the zero limit of lateral energy loss agree quite well but it also shows the pressure in the focal spot (P_i, $P_{i\ell}$) is reduced by the loss.

Figure 5.16 shows the 0.53 μm results and also those from spherical target measurements (14), again the agreement is good.

Other measurements (116) at 0.35 μm (see Fig. 5.17) of mass ablation rate can yield under a similar analysis to the above $P_{\infty \ell}$ agreeing well with our results.

5.6 CONCLUSIONS

A study has been made of ablation as a function of wavelength and irradiance at absorbed intensities between 10^{13} and 10^{15} W cm^{-2} and laser wavelengths of 1.05 μm, 0.53 μm and 0.35 μm. It was found that for small focal spot sizes lateral energy transport is important. A model of ablation from two regions to take account of this is presented to estimate the ablation parameters in the absence of this process.

The results confirm that short wavelengths are advantageous for ablative compression and quantify that advantage.

CHAPTER SIX

PLASMA SPECTROSCOPY

		Page
6.1	INTRODUCTION	108
6.2	EMISSION AND ABSORPTION PROCESSES	108
6.3	IONISATION MODELS	108
6.3.1	LOCAL THERMODYNAMIC EQUILIBRIUM	109
6.3.2	CORONAL EQUILIBRIUM	110
6.3.3	COLLISIONAL RADIATIVE REGION	111
6.4	LINE INTENSITIES	112
6.5	ENVIRONMENTAL EFFECTS ..	113
6.5.1	DOPPLER BROADENING	114
6.5.2	STARK BROADENING	114
6.5.3	RADIATIVE TRANSFER	114

6.1 INTRODUCTION

The emitted radiation from a laser produced plasma provides a rich source of information about the state and type of matter from which it originates. This chapter will outline, briefly some of the relevant spectroscopy. It is a general rule of thumb that the emission of interest occurs at

$$h\upsilon \sim \text{few } kT_e \qquad 6.1$$

6.2 EMISSION AND ABSORPTION PROCESSES

There are three processes which together give the basic emission spectrum; line radiation, recombination radiation and Bremmstrahlung (117). The latter two being broadband emissions.

Many electron processes occur in the non-hydrogenic ions such as auto-ionisation and dielectronic recombination and involve doubly excited levels. These processes are important in determining population levels in a plasma (118). Dielectronic satellite radiation arises from these doubly excited levels when one of the two electrons decays to the ground state. For a doubly excited helium-like ion this can be similar to a hydrogenic decay with a slight longer wavelength due to the shielding of the second electron.

In the severe plasma environment (high temperature and density) mixing of the levels can occur and transitions forbidden by the normal selection rules (117) appear in the emission spectrum.

6.3 IONISATION MODELS

In a plasma where transition rates are balanced by detailed inverses thermodynamic arguments alone can be used. If the plasma is optically thin but collisions dominate radiative rates, the plasma is in local thermodynamic equilibrium (LTE) and is characterised by an electron temperature (T_e).

Another region where approximations can be made is the coronal domain. Here the plasma is considered optically thin and ionisation equilibrium is simply a balance between collisional ionisation and radiative recombination.

6.3.1 LOCAL THERMODYNAMIC EQUILIBRIUM

This is the approximation which is valid at sufficiently high densities where collisional processes dominate. The ionic distribution is described by the Saha equation (119)

$$\frac{n_z\, n_e}{n_{z-1}} = 2\left(\frac{2\pi\, m_e\, kT_e}{h^2}\right)^{1.5} \frac{B_z(T_e)}{B_{z-1}(T_e)} \exp\left(-\frac{E_{z-1}(\infty)}{kT_e}\right) \qquad 6.2$$

where

n_z - the density of ion of charge z

n_e - the electron density

m_e - the electron mass

kT_e - the electron temperature

$B_z(T_e)$ - the partition function

$E_{z-1}(\infty)$ - the ionisation energy of the (z-1) ion species.

The partition function is

$$B_z(T_e) = \sum_{\text{all } p} g_z(p) \exp\left(-\frac{E_z(p)}{kT_e}\right) \qquad 6.3$$

where the plasma removes the upper states by ionisation depression (120,121,122).

A necessary but not sufficient condition for LTE to be valid is (119)

$$n_e \geq 1.6 \times 10^{12}\, (kT_e)^{0.5}\; E_T^{\,3}\ \text{cm}^{-3} \qquad 6.4$$

where E_T is the largest energy gap in the term of the scheme considered.

Although full LTE is not achieved in present laboratory plasmas partial LTE can exist between the higher levels in an ion and Griem (104) has proposed for hydrogen-like ions that level n and above are in LTE if

$$n_e \geq \frac{2 \times 10^{18} Z^6 (kT_e)^{0.5}}{n^{8.5}} \text{ cm}^{-3} \qquad 6.5$$

As well as the condition on density the electron-electron collision rate must be large enough compared to the timescale of the plasma parameters.

Griem (104) derived an equilibration time for hydrogen-like ions, levels n and above of

$$\tau_n = \frac{4.5 \times 10^7 Z^3}{n^4 n_e} \left(\frac{kT_e}{Z^2 E_H}\right)^{0.5} \exp\left(\frac{Z^2 E_H}{n^3 kT_e}\right) s \qquad 6.6$$

and an equilibration time for ionisation states of

$$\tau_Z = \frac{1.15 \times 10^7 Z^3 N_+}{n_e (N_+ + N)} \left(\frac{kT_e}{Z^2 E_H}\right)^{0.5} \exp\left(\frac{Z^2 E_H}{kT_e}\right) s \qquad 6.7$$

where N_+ and N are the total densities of the ionisation states Z + 1 and Z respectively (123).

6.3.2 CORONAL EQUILIBRIUM

Coronal ionisation equilibrium where the dominant processes are collisional excitation and spontaneous emission has been tabulated by Jordan (124) and House (125) for elements up to Z = 48. McWhirter (119) gives a timescale for the formulation of the last ion stage (Z) as

$$\tau = \frac{1}{n_e(S(z-1) + \alpha(Z))} \qquad 6.8$$

where

S - the collisional ionisation coefficient

α - the radiative recombination coefficient.

which for Z = 10 and $n_e = 10^{22}$ cm^{-3} gives $\tau = 10^{-10}$ s and is of the order of the plasmas considered here showing that a more accurate description should be time dependent (119).

6.3.3 COLLISIONAL RADIATIVE REGION

The LTE and coronal regions form the two extreme of models with respect to density. In between these account has to be taken of the transitions between all the bound levels.

A collisonal radiative model by Bates et al (126) includes, ionisation from any bound level, three body recombinations into any level, collisional transitions between bound levels, spontaneous radiative decay and radiative recombination. The plasma is assumed to be optically thin to its own radiation although the case for an optically thick 1-2 transition is considered in a later paper (127). The model describes the regions between the LTE and coronal models and reduces to these at high and low electron densities respectively. This transition is shown in Fig. 6.1. This model only describes the equilibrium between fully stripped and hydrogen-like ions. Summers (128) extended these calculations to cover fully-stripped to argon-like and includes the density dependent dielectronic recombination.

Lee (129) has written a code to calculate the population levels under this scheme. Preliminary calculations are performed to determine which states are in LTE. Then a coronal approximation is applied to the remaining states as a first guess to state populations, electron density, and ionisation potential depression. Rate equations are then used to determine the level populations of the excited states and auto-ionising levels of the hydrogen-like and helium-like levels. The process is iterative and stops when the electron density converges to the desired value.

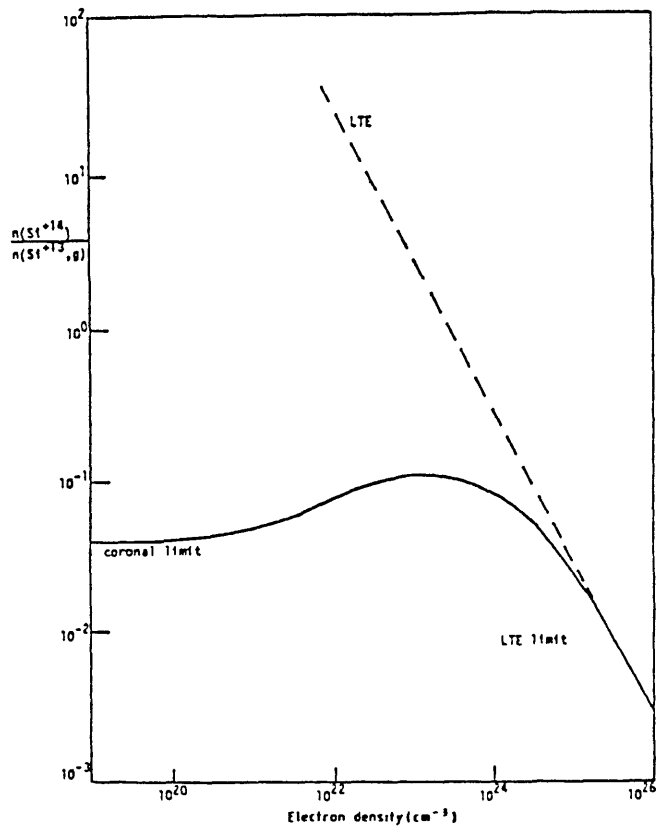


Fig. 6.1 COLLISIONAL RADIATIVE EQUILIBRIUM FOR SILICON AT T_e = 540 eV

6.4 LINE INTENSITIES

For an optically thin plasma the number of photons emitted per unit time and volume

$$n[\nu(p,q)] = N(p)\, A(p,q) \qquad 6.9$$

For coronal or LTE models the calculation of N(p) is straightforward though care must be taken about the model validity and the possibility of opacity effects. For

collisional-radiative models the calculation is more complex (Lee's program (see Section 6.3.3) gives some line intensities), as many population mechanisms have to be considered.

The optically thin line intensities have provided a means of density and temperature diagnosis and the hydrogen-like and helium-like transitions and the associated radiation have been extensively analysed (104, 119). For example, the doublet ratio of the hydrogenic $1S_{1/2} - 2P_{2/3,3/2}$ departs from the statistical value of 0.5 in the collisional-radiative region due to mixing of the $2P_{1/2}$ and $2P_{3/2}$ levels. This process which is density dependent and significant in this region will give rise to a density diagnostic (130).

In the case of helium-like ions the ratios of the resonance line, $1s^2\ {}^1S_0 - 1s2p\ {}^1P_1$, intercombination line, $1s^2\ {}^1S_0 - 1s2p\ {}^3P_1$ and spin forbidden line $1s^2\ {}^1S_0 - 1s2s\ {}^3S_1$ depend on electron density over a wide range (118,131).

For typical laser produced plasmas, opacity effects are important, especially for the lower members of the resonance line series and this will seriously alter the line ratios observed.

The dielectronic satellites (see Section 6.2) can also be interpreted to give electron densities and temperature (132).

6.5 ENVIRONMENTAL EFFECTS

The line spectra is affected by emission processes, line broadening and radiative transfer. This section will deal with the last two effects. Line broadening can be divided into three types;

a) natural broadening

b) doppler broadening

and c) Stark broadening.

For the plasmas here natural broadening is generally negligible relative to the other broadening mechanisms.

6.5.1 DOPPLER BROADENING

Doppler broadening is given by:

$$P(\Delta w) = \frac{1}{\pi^{0.5}\ \Delta\omega_o} \exp\left(-\frac{\Delta\omega^2}{\Delta\omega_o{}^2}\right) \qquad 6.10$$

where

$$\Delta\omega_o = \frac{\omega}{c}\left(\frac{2k\ T_i}{m_i}\right)^{0.5} \qquad 6.11$$

This broadening is suppressed if the particle mean free path for collisions is less than the emitter wavelength (133).

6.5.2 STARK BROADENING

The broadening is greatest for transitions from levels of high principle quantum number leading to line widths which vary as (104)

$$\Delta\upsilon \propto n_1^2 - n_1^2 \qquad 6.12$$

6.5.3 RADIATIVE TRANSFER

For a plasma of finite size the optical opacity is

$$\tau_0(\upsilon) = \int_{-\infty}^{\infty} k\ (\upsilon,x)\ dx \qquad 6.13$$

where

$$k(\upsilon,x) = K(\upsilon,x)\left[1-\exp\left(-\frac{h\upsilon}{kT}\right)\right] \qquad 6.14$$

$K(\upsilon,x)$ is the absorption coefficient of a plasma (for line and continuum radiation) at the frequency υ and position x.

If $\tau_o(\upsilon)$ is very much less than 1 the resulting radiation is optically thin and its intensity is just

$$I(\upsilon) = \int_{-\infty}^{\infty} \varepsilon(\upsilon,x)\, dx \qquad 6.15$$

where

$\varepsilon(\upsilon,x)$ - the emission coefficient.

When re-absorption is not negligible

$$dI(\upsilon,x) = (\varepsilon(\upsilon,x) - k(\upsilon,x)\ I(\upsilon,x))\, dx \qquad 6.16$$

over the path element dx. This leads directly to the equation of radiative transfer

$$I(\upsilon) = I(\upsilon_o)\ \exp(-\tau_o) + \int_o^{\tau_o} S(\upsilon,\tau)\ \exp(-\tau)\, d\tau \qquad 6.17$$

using τ as a variable, and

$$S(\upsilon) = \frac{\varepsilon(\upsilon)}{k(\upsilon)} \qquad 6.18$$

is the source function.

In general the solution of this equation is difficult because of the effect of re-absorption on the energy level populations. In the limiting cases where these effects are decoupled, solutions are possible. One such is LTE where the population levels depend only on collisional effects and the source function is just

$$S(\upsilon,x) = B(\upsilon,T(x)) \qquad 6.19$$

where

$T(x)$ - the local temperature

and $B(\gamma,T)$ - the Plank function (134).

For a homogeneous plasma where the temperature is uniform the radiative transfer equation becomes

$$I(\upsilon) = B(\upsilon,T)\ (1 - \exp\ (-\tau_o)) \qquad 6.20$$

This predicts a saturation of the line intensity at the black body limit. When opacity is large there is opacity broadening of the line which has a flat region in the centre of its profile. This is the most common correction for opacity used in calculations even though the radiative effects may not entirely be decoupled and the plasma not homogenous.

CHAPTER SEVEN

THE DESIGN OF THE Mk.IV MINIATURE X-RAY SPECTROMETER

		Page
7.1	INTRODUCTION	118
7.2	DIAGNOSTIC DEVELOPMENT	118
7.3	BRAGG REFLECTION	118
7.4	TYPES OF SPECTROMETERS	119
7.5	THE FLAT CRYSTAL SPECTROMETER	119
7.6	THE Mk.IV MINIATURE X-RAY SPECTROMETER	121
7.7	FILM	127
7.8	PROBLEMS OF THE Mk.IV SPECTROMETER IN USE	128

7.1 INTRODUCTION

This chapter details the design and construction of a miniature X-ray spectrometer for use in the six beam target area at the Rutherford Laboratory (14). This device enabled the spectra of a laser produced plasma to be produced in a single shot with a spectral range and resolution comparable to similar devices developed earlier (103) for the two beam target chamber.

7.2 DIAGNOSTIC DEVELOPMENT

As has been noted earlier (see Section 6.1) the spectral region of interest for laser produced plasmas is in the soft X-ray region. A variety of instruments were quickly developed to help analyse these plasma signatures.

Initial techniques consisted of finding a time averaged value of the electron temperature (135) from the slope of the X-ray continuum using a set of foils with differing transmission factors (136) to get a crude spectral resolution. The X-ray detection was either scintillators or X-ray diodes (137). The spectral details of the plasma were recorded using normal incidence or grazing incidence spectroscopy (138). It was only with significant increases in laser power and plasma temperature that Bragg crystal spectrometry became practical (7). Spatial resolution was obtained by putting a narrow slit in the plane of the crystal dispersion (139).

Crystal dispersion has high spectral resolution with inherent resolving powers of 10^4, this is often limited by the physical size of the X-ray source (140). The relative advantages of applying Bragg crystal and grazing incidence spectrometers to the study of laser produced plasmas is discussed in reference 55.

7.3 BRAGG REFLECTION

The rocking curve and reflection integral are functions of wavelength (angle) and are unique to a particular crystal

specimen. It is necessary to know these values so that the relative intensities of lines can be compared and the instrumental broadening can be allowed for when doing line width calculations. Rocking curves and reflection integrals can be calculated for both perfect and ideal mosaic crystals (141). The curves for real crystals fall somewhere between these two and measurements have to be made, for a crystal to be usable.

7.4 TYPES OF SPECTROMETERS

The variety of crystal spectrometers is described in reference 142. The simplest types of Bragg spectrometer is the flat crystal instrument as described in the next section. The de Broglie spectrometer (143) has a crystal bent to a convex cylindrical surface giving a greater spectral range. This type of instrument has been widely used to obtain X-ray spectra of multiply charged ions in laser produced plasmas (11,55). Spectrometers with crystals bent to a concave cylindrical surface give greater sensitivity and resolution (142). Both these spectrometers though suited to small sources do not offer a very wide spectral range.

7.5 THE FLAT CRYSTAL SPECTROMETER

Reference 103 gives an analysis for a flat crystal spectrometer, a schematic of which is shown in Fig. 7.1. and gives, for source size limited resolution, resolving power by

$$\frac{\lambda}{\Delta\lambda} = \tan\theta \frac{L}{\Delta x} \qquad 7.1$$

where

θ - the incidence co-angle

L - the plasma-crystal-film distance

Δx - the source size.

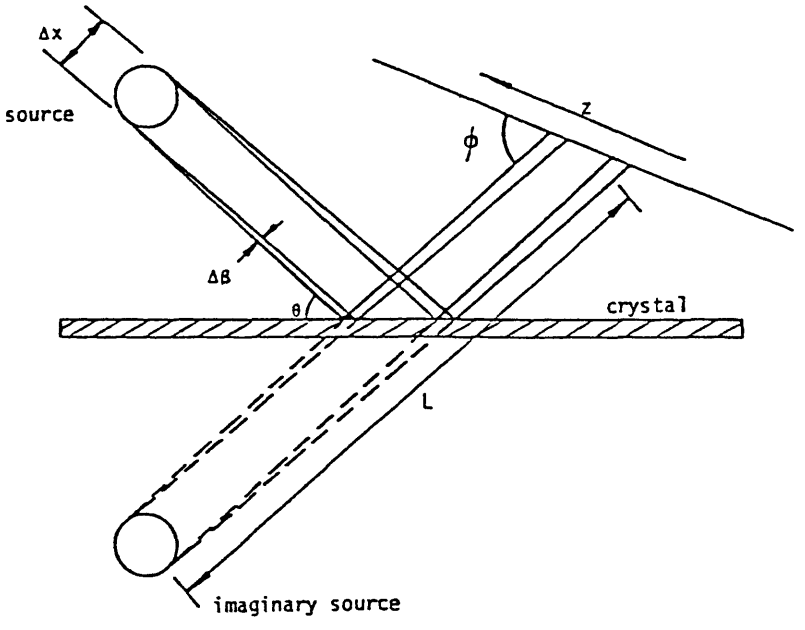


Fig. 7.1 SCHEMATIC OF A FLAT CRYSTAL SPECTROMETER

and the sensitivity by

$$S = \frac{R_c \sin\phi}{L \Delta x} \qquad 7.2$$

where S times the emission from a volume increment gives the exposure of the film.

The transmission of the X-ray filter also has to be taken into account.

Spatial resolution in one dimension (obtained by placing a narrow slit in the plane of dispersion) (see Fig. 7.2) gives a magnification of

$$m = \frac{R_2}{R_1} \qquad 7.3$$

and is limited normally by the slit width which gives an angular uncertainty of

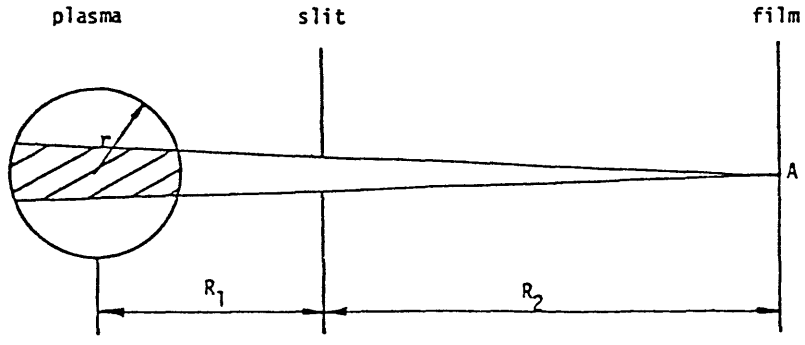


Fig. 7.2 SCHEMATIC OF A SPACE RESOLVING SPECTROMETER

$$\Delta\theta = w\left(\frac{1}{R_1} + \frac{1}{R_2}\right) \qquad 7.4$$

where

w - slit width

R_1 - plasma-slit distance

R_2 - slit-crystal-film distance.

If a slit is used the sensitivity is reduced.

7.6 THE Mk.IV MINIATURE X-RAY SPECTROMETER

With the advent of a six beam target chamber at the Central Laser Facility of the Rutherford Laboratory (144) there was a requirement to have a miniature X-ray spectrometer to produce spectra comparable with those produced from a single laser shot by earlier instruments (103). In practice this meant another flat crystal Bragg spectrometer using the crystals designed for the previous models. The plasma to slit distance should be the same as before, approximately 5 mm. The main problem was to avoid interference of the laser beams by the spectrometer. This was not possible with the previous X-ray spectrometers at this distance from the plasma.

Figure 7.3 shows a side view of the beam chamber. The laser beam axes are at right angles to each other and enter the chamber by the ports marked L (the horizontal pair being north-south). The east-west horizontal ports are used for a probe beam (P) whilst the top port is used for a backlighting laser beam (B).

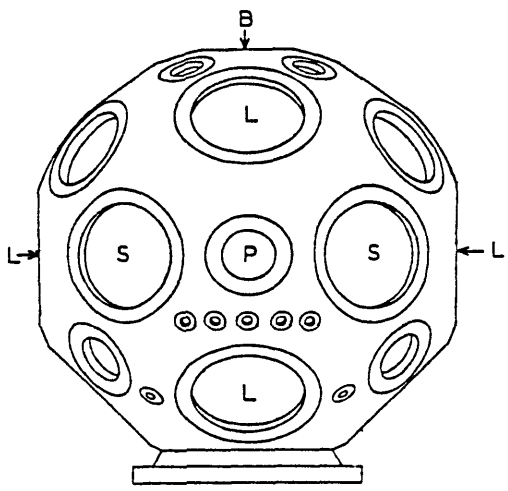


Fig. 7.3 ELEVATION OF THE RUTHERFORD SIX BEAM TARGET CHAMBER

The best available port for a spectrometer is the one marked with an S (i.e. any of the horizontal ports at 45° to the north-south laser axis). Figure 7.4 shows how the laser beams intersect this plane (for f/1 focussing). The axes are plotted in units of the distance to the plasma from the plane and so can be used for any part of the spectrometer to determine the space between the beams.

The original spectrometers (particularly the 'Mk.I, see Fig. 7.5) were used as a basis for the new design (Fig. 7.6).

The specifications shown in Table 7-1, Mk.IV, as compared with the Mk.I version of this type of spectrometer. An example of its spectra is shown in Fig. 7.7.

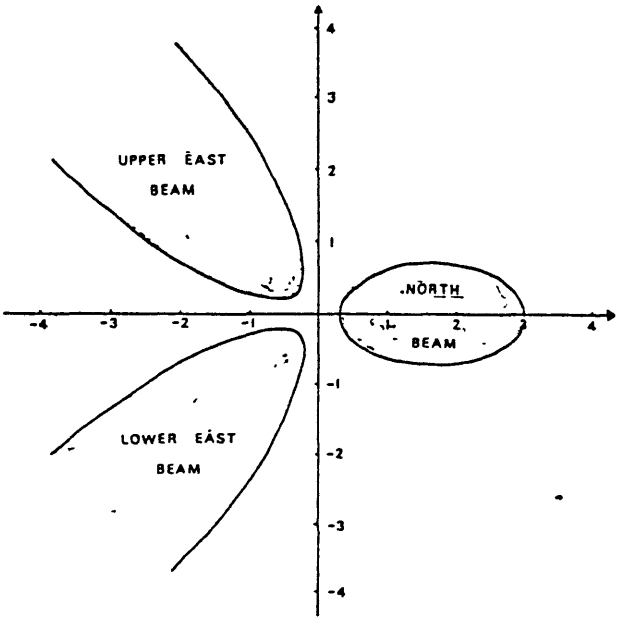


Fig. 7.4 LASER BEAM PROFILES IN THE SPECTROMETER PLANE (AXIS UNITS ARE THE DISTANCE OF THE PLANE FROM THE PLASMA)

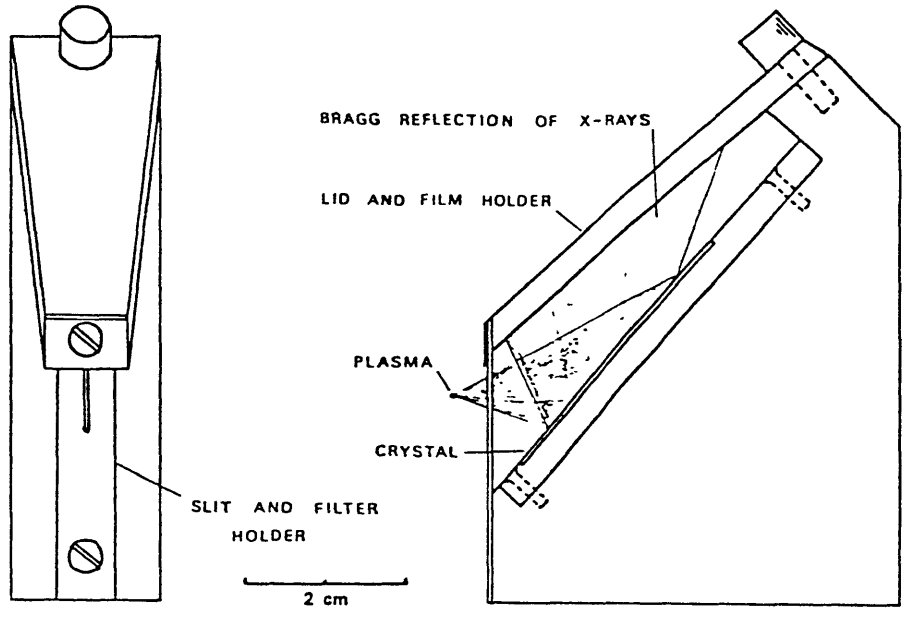


Fig. 7.5 Mk.I MINIATURE X-RAY CRYSTAL SPECTROMETER

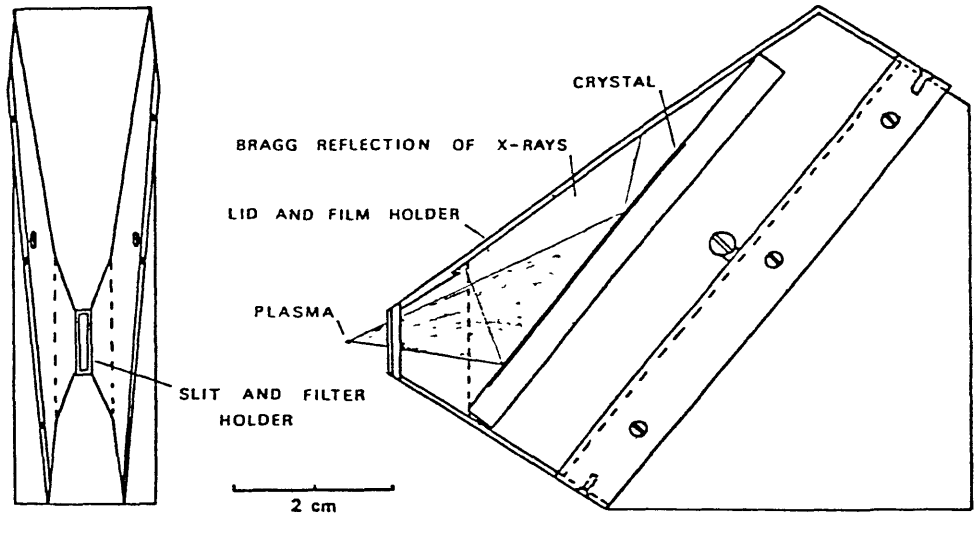


Fig. 7.6 Mk.IV MINIATURE X-RAY CRYSTAL SPECTROMETER

TABLE 7-1

SPECTROMETER SPECIFICATIONS

	Mk. IV	Mk.I
Spectral Range (with PET crystal)	3 - 8 Å	3 - 8.3 Å
Spectral Resolution (with 15 μm source size)	1500 at 8 Å 5200 at 3 Å	1300 at 8 Å 5500 at 3 Å
Relative Luminosity to Mk. I at 3 Å	2.721 0.930	5.156 1.000
Magnification	6.6 at 8 Å 11.3 at 3 Å	3.8 at 8 Å 10.9 at 3 Å

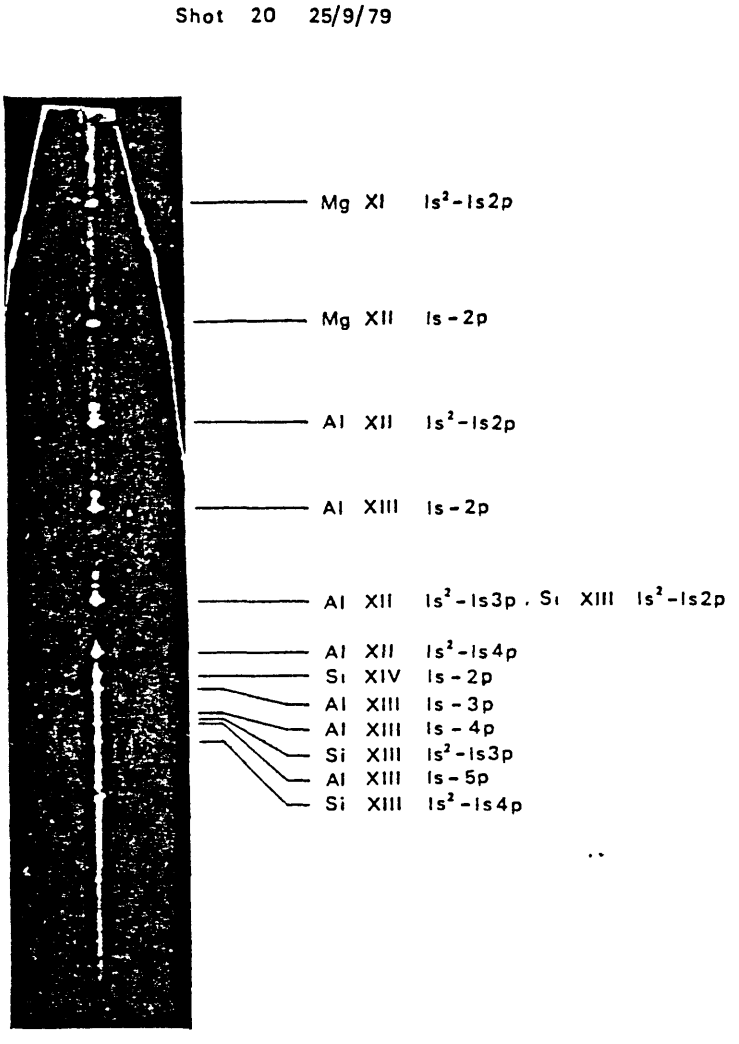


Fig. 7.7 TYPICAL SPECTRA FROM THE Mk.IV SPECTROMETER

7.7 FILM

Two films were used in this spectrometer. Kodirex and Industrex C X-ray films. A calibration of Kodirex for sensitivity at various wavelengths was carried out by Hobby and Peacock (102) and is reproduced in Fig. 7.8. A calibration of Industrex C was carried out on the X-ray micro-focus source at the Rutherford Laboratory (144) and the resulting curve has been added to Fig. 7.8.

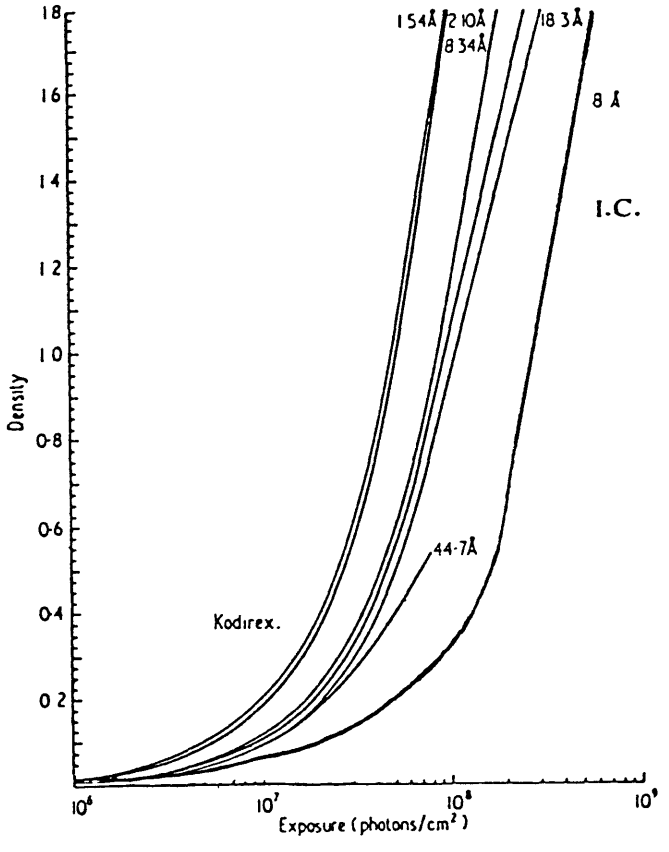


Fig. 7.8 CHARACTERISTIC EXPOSURE CURVES FOR KODIREX (102) AND INDUSTREX C

Developing for both films was standardised using Kodak DX 80 developer diluted 1:4 with water for the time shown in Table 7-2. Fixing was for 10 min and washing 30 min.

TABLE 7-2
DEVELOPING TIMES IN KODAK DX 80

Temperature (°C)	Time (mins)
18	5.0
20	4.0
22	2.0
24	2.5

7.8 PROBLEMS OF THE Mk.IV SPECTROMETER IN USE

A number of problems arose during the use of the Mk.IV miniature X-ray spectrometer.

Due to the need of having the spectrometer sides integrated into the lid the delicate Bragg crystals are more exposed and so more likely to get damaged.

Care was needed on the fitting of the filter and slits which was by glueing with an epoxy resin.

A somewhat more important problem was fogging of the film at the end nearest the plasma. This was caused mainly by spurious radiation generated from the filtering by the X-ray flux from the plasma. It could be reduced somewhat by using the narrowest possible slit.

CHAPTER EIGHT

EXPERIMENTAL DETERMINATION OF PLASMA PARAMETERS USING ARGON SPECTRA

			Page
8.1	INTRODUCTION		130
8.2	EXPERIMENTAL METHOD		130
	8.2.1	X-RAY PINHOLE CAMERA	132
	8.2.2	MINIATURE X-RAY CRYSTAL SPECTROMETER	133
	8.2.3	METHOD OF ANALYSIS	134
		8.2.3.1 THEORETICAL LINE PROFILES	134
		8.2.3.2 EXPERIMENTAL PROFILES	135
		8.2.3.3 FITTING ROUTINE	136
8.3	RESULTS		139
	8.3.1	INTRODUCTION	139
	8.3.2	ANALYSIS	139
		8.3.2.1 SELF-CONSISTENT FIT TO A SERIES	140
		8.3.2.2 SELF-CONSISTENT FIT TO Ar XVII $1s^2$-1s2p GROUP	143
		8.3.2.3 DIELECTRONIC SATELLITE RATIO	144
8.4	COMPARISON WITH IONISATION MODEL		147
8.5	CONCLUSIONS		148

8.1 INTRODUCTION

This chapter outlines the use of plasma spectroscopy to provide details of a laser produced plasma. Results from an exploding pusher experiment (see Chapter 3), where a microballoon containing argon is compressed, is presented and the analysis of the argon spectra to provide core parameters of electron density, temperature and opacity is demonstrated. This work contains the first self-consistent analysis of a complete argon, hydrogen and helium like, spectra and shows three methods of electron density determination:

a) Stark broadening (see Chapter 6)

b) intercombination line width and the ratio of its intensity to that of the associated singlet transition.

c) relative dielectronic statellite intensities (see Chapter 6)

((b) depends on the assumption that the triplet line is optically thin whilst the singlet is optically thick (see later).) This data provides figures of the ground and excited states densities when compared with an ionisation model.

8.2 EXPERIMENTAL METHOD

The experiment summarised in this chapter was performed at the Rutherford Appleton Laboratory using the VULCAN laser system (14) in its 1.05 μm, short pulse (mode locked (98)) configuration delivering up to 10 J in 100 ps in each of six beams.

The six beam target area at RAL was used so that even intensity could be applied over the whole surface of the spherical targets. The six beams are each focussed along a rectangular axis set (see Fig. 8.1), one target radius beyond the target centre (see Fig. 8.2) the overlap of the beams overcoming the reduction in intensity at their edges.

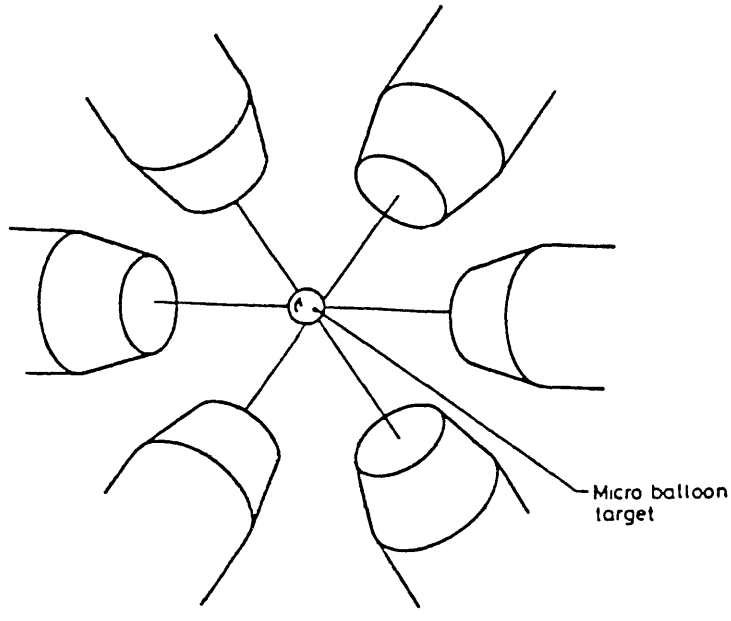


Fig. 8.1 RELATIVE BEAM DIRECTIONS IN THE RUTHERFORD SIX BEAM TARGET CHAMBER

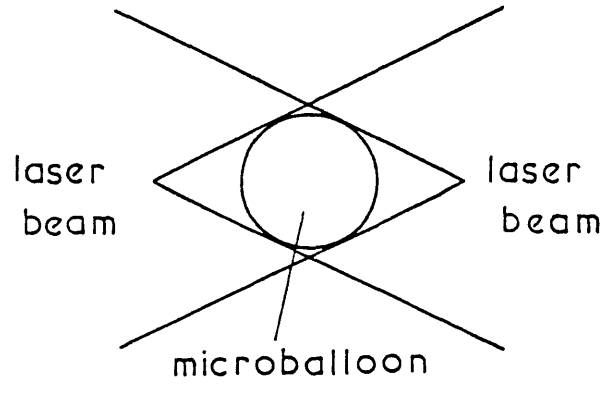


Fig. 8.2 FOCUSSING OF THE LASER BEAMS, ONE TARGET DIAMETER BEYOND THE TARGET CENTRE

The type of targets used were spherical glass microballoons (72) of approximately 100 μm diameter and wall thickness of about 1 μm. These targets were coated with a thin layer (~40 nm) of aluminium to aid alignment at the centre of the target chamber by good reflection of the alignment CW lasers. All the microballoons were filled with 0.4 bar argon and supported by 5 μm carbon fibres.

The main diagnostics were an X-ray pinhole camera and two miniature space resolving X-ray crystal spectrometers.

8.2.1 X-RAY PINHOLE CAMERA

X-ray pinhole imaging was by two 6 μm pinholes (filtered to 1.4 keV and 2.4 keV) in a 20 μm platinum substrate with a magnification of 4 onto Kodirex X-ray film.

Typical results are shown in Fig. 8.3 for a glass walled microballoon.

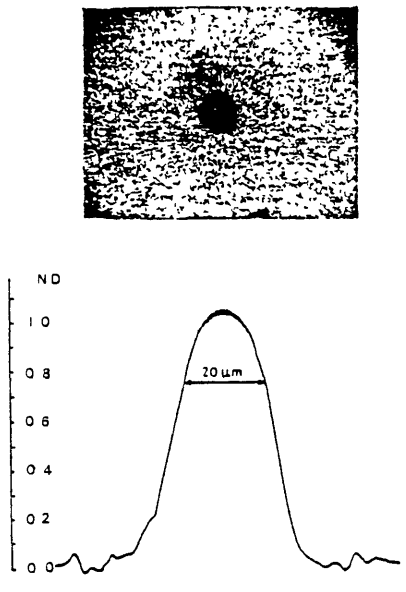


Fig. 8.3 PINHOLE PHOTOGRAPH AND DENSITOMETER TRACING OF AN IMPLODED ARGON-FILLED GLASS MICROBALLON

8.2.2 MINIATURE X-RAY CRYSTAL SPECTROMETERS

The Mk.IV miniature crystal spectrometer (Chapter 7) was used as a general recording spectrometer to obtain spectra of the silicon and argon emission.

A 5 μm slit lying in plane of dispersion provided ~10 mÅ spatial resolution and filtering of 25 μm beryllium giving a cut-off of 1.4 keV whilst keeping the spectrometer light tight and also blocking the debris from the target.

The Mk.I miniature crystal X-ray spectrometer (103), without a slit, was also used, but at a greater distance from the plasma.

Both spectrometers used PET crystals giving wavelengths from 7.5 Å to 3 Å in the case of the Mk.IV and 5 Å to 2.5 Å in the case of the Mk.I. These crystals had been previously calibrated by K. Evans at Leicester University for reflectivity and rocking curves (145).

An expanded densitometer tracing with line identifications is shown in Fig. 8.4 for the argon spectral region.

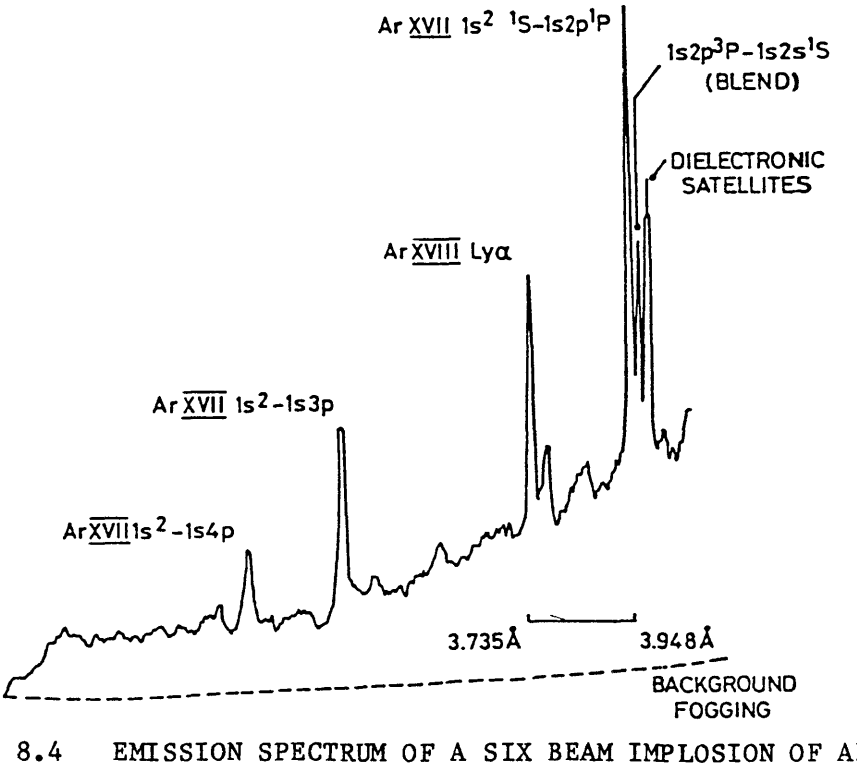


Fig. 8.4 EMISSION SPECTRUM OF A SIX BEAM IMPLOSION OF AN ARGON-FILLED GLASS MICROBALLON

8.2.3 METHOD OF ANALYSIS

The pinhole pictures and spectra were densitometered on a Mk.3 Joyce-Lobel microdensitometer.

The pinhole pictures gave a size to the core plasma which could be used to determine a scale length for use in the line fitting procedure (103).

The main method of diagnosis was using an iterative graphics routine available on the CDC 6400 computer at Imperial College, London. The routine is fed by a suite of programs which:

- calculate theoretical line profiles
- prepare the experimental line profiles.

This suite was written initially by R.W. Lee (129).

8.2.3.1 THEORETICAL LINE PROFILES

The optically thin profiles were generated using programs based on Lee's calculations which are reported in references 146, 147 and 148. A brief description is given here.

Initially two sets of profiles were generated referred to as the standard and the full sets. From the standard sets the electrons are treated dynamically and the ions as quasistatic perturbations (149). For the full set the ions are treated dynamically and the first order shifts and broadening functions from the emitter charge are included, also the fine structure splitting is included in the calculation for the hydrogen-like 1-2 transition.

The differences produced by these functions are demonstrated in Fig. 8.5 (148) which shows an Ar XVIII 1s-2p line at an electron temperature of 5×10^6 °K and electron density of 5×10^{23} cm^{-3}. The solid line shows the standard theory with no

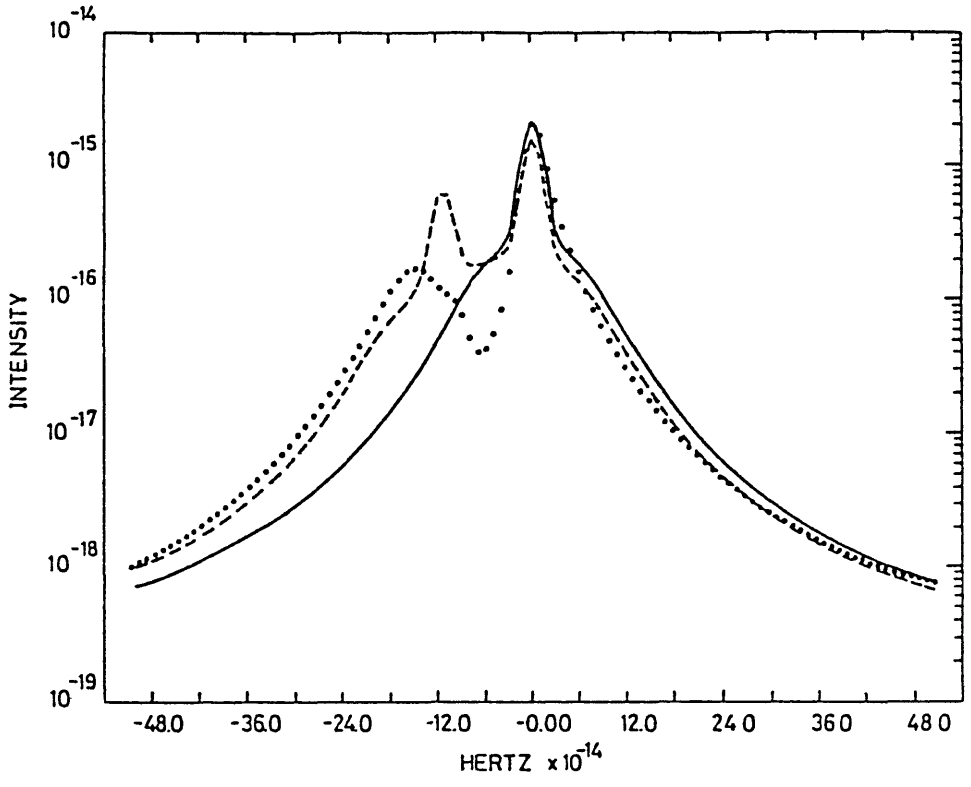


Fig. 8.5 THEORETICAL STARK BROADENED LINE PROFILE OF AN Ar XVIII 1s-2p TRANSITION

fine structure splitting, the dashed line shows the profile when the two fine structure components are treated additively and the dotted line shows the profile when proper L-S coupling (117) is applied.

In this work the full theories were used as the hydrogen-like 1s-2p and helium-like $1s^2$-1s2p lines where the effects are greatest are used for analysis.

8.2.3.2 EXPERIMENTAL PROFILES

The densitometered spectral lines were put into the computer using a graphical digitising tablet which creates a file in binary form of the co-ordinates of the points on the tablet.

This is converted to a set of photon flux versus wavelength difference from the peak of emission which is then used as the data file for the fitting routine.

8.2.3.3 FITTING ROUTINE

Before comparison with the experimental profiles, the fitting routine applies a series of broadening processes in the same order as they occur during emission and observation. First the lines were doppler broadened by an amount corresponding to the ion temperature with the assumption that it is equivalent to the electron temperature. The profiles were then opacity broadened according to the simple formula for the intensity emitted from a uniformly emitting and absorbing slab in LTE.

$$I_\upsilon(\ell,\upsilon) = B(\upsilon,T)(1 - \exp(-\tau(\ell,\upsilon))) \qquad 8.1$$

where B(v) is the black body function

$$B(\upsilon,T) = \frac{2h\upsilon^3}{c_L^2}\left[\frac{1}{e^{\frac{h\upsilon}{kT}} - 1}\right] \qquad 8.2$$

and $\tau(\ell,\upsilon)$ is the optical depth, at frequency υ due to a slab of length ℓ, defined by

$$\tau(\upsilon,\ell) = \frac{n_l\, L(\upsilon)\, e^2\, \ell\, f_{lj}}{e\, \varepsilon_0\, m_e\, c_L} \qquad 8.3$$

where

f_{lj} - the absorption oscillator strength for the transition l to j

n_l - the number density of the lower state of the transition

$L(\upsilon)$ - is the area normalised optically thin line profile.

To correct for emission from a uniformly emitting sphere rather than a slab the value of ℓ, measured as the diameter of the compressed core, had to be reduced by a factor of 1.5 (150).

Finally the instrument profile which was assumed to be gaussian was convolved with the opacity corrected profiles. The instrument profile was dominated (by the source sizes of ~10 μm).

The actual fitting procedure was accomplished by an interactive graphics routine where the fit of the theoretical line profile could be adjusted for opacity, line width and instrument width.

The initial procedure was to shift the broadened theoretical profiles in wavelength to best coincide with the experimental profiles. A choice of scaling of the profile is offered:

a) by equating the intensity of a single experimental point with the theoretical intensity at that wavelength

b) by a least squares fit

c) by equating the areas under the two profiles.

The latter, area normalisation, was most frequently used though, as will be shown later, in some cases, this is not always initially practicable. In general it was felt that this gave a better physical representation.

A quality of fit figure is calculated in each case and is a normalised sum of squares figure, Q, defined by:

$$Q = \frac{\sum(y_{exp} - y_{th})^2}{\sum y_{th}^2} \qquad 8.4$$

where y_{exp} and y_{th} are the experimental and theoretical values of intensity at the same wavelength. The sum is over all experimental points inside the range of the theoretical profile. In general a fit of Q = 0.01 is considered good whereas a fit with Q = 0.1 is poor. Fitting examples will be shown when discussing the results.

There are two major variables in determining the line shape the electron density n_e and the ground state density n_1 (for a given scale length ℓ) (see Chapter 6) but any one line width is not a unique function of n_e and n_1 though the detailed shape may be. This applies for optically thick plasmas, in the case of small optical depth there is little opacity broadening and the line width approximates to a function of electron density, n_e. Therefore a plot of 'best fit' on an $n_1\ell$, n_e axes set at low $n_1\ell$ will be a line at constant n_e and as increasing optical depth tends to increase the apparent line width the required n_e needed to provide the rest of the broadening will decrease.

Ideally, if this is done for a number of transitions in the same series (see Fig. 8.6) the lines of best fit would intersect

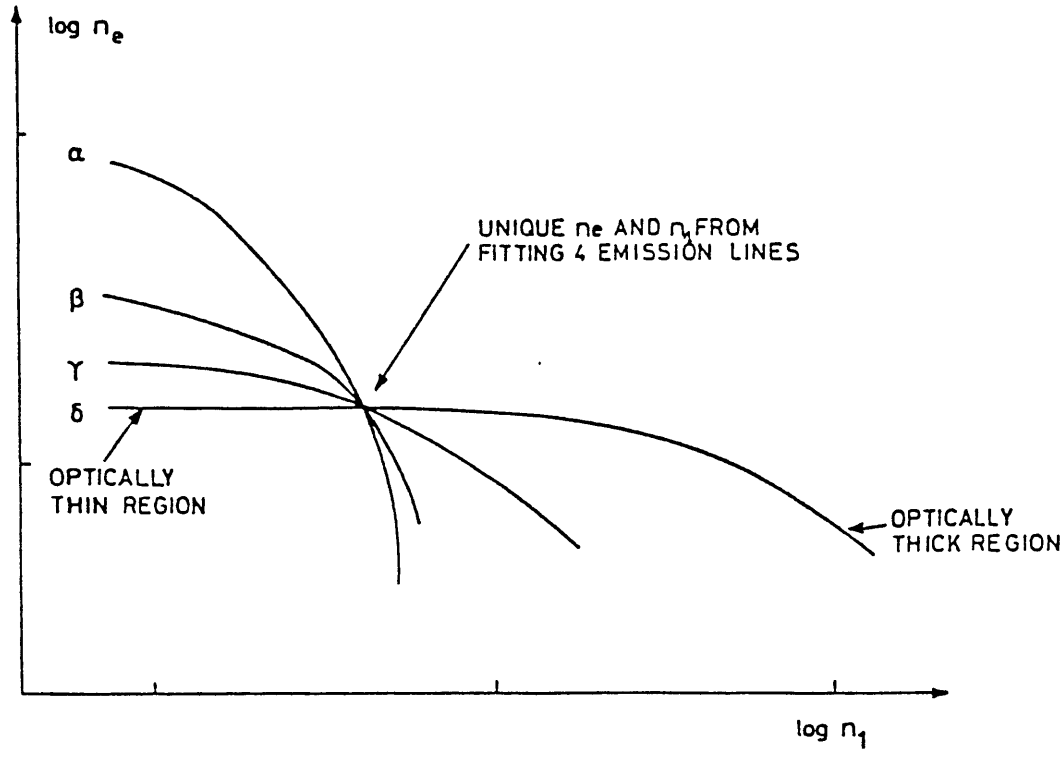


Fig. 8.6 IDEALISED LINES OF BEST FIT FOR SEVERAL SPECTRAL LINES FROM THE SAME SERIES IN n_e, n_1 PARAMETER SPACE

at a single point defining the electron density and ground state density for the slab and series. In practice the 'point' defined is an area determined by a value of Q taken as $Q < 2Q_{MIN}$ where Q_{MIN} is the lowest value of Q obtained during the fitting of the particular line. Hence there is an area of best fit defined by the overlap of these bands from several transitions.

8.3 RESULTS

8.3.1 INTRODUCTION

In this section the analysis of the results from one particular shot no.131 on 29.5.80 will be considered. The target was a glass walled microballoon of 93 μm diameter and 1 μm wall thickness filled with 0.4 bar argon and coated with a thin layer of aluminium (~40 nm). Irradiation with a 100 ps, 1.05 μm laser pulse at 10^{15} W cm^{-2} made this target behave as an exploding pusher (see Chapter 3).

The pinhole picture from shots 131 gives a slab scale length of ~7 μm. This source size gives instrumental broadening of half-width 5 mÅ.

The initial analysis consisted of a determination of the electron temperature by measuring the slope of the recombination continuum of the silicon helium and hydrogen-like series (see Chapter 6). This was done for shot 131 giving a value of 600 ± 70 eV.

8.3.2 ANALYSIS

As stated in the introduction there were three methods of diagnosing the core parameters by using the spectral lines:

a) a self-consistent fit to a whole spectral series

b) by a self-consistent fit to the Ar XVII $1s^2$-1s2p singlet and triplet combination.

and c) by measuring the ratio of the dielectronic satellites associated with the Ar XVIII 1s-2p line.

I will consider each of these in turn with reference to shot 131.

8.3.2.1 SELF-CONSISTENT FIT TO A SERIES

Groups of theoretical doppler broadened line profiles were generated by Lee's programs at an electron temperature of 500 eV and a range of electron densities which encompassed the expected value, around 10^{23} cm^{-3}. One group was for the hydrogen-like lines and one for the helium-like lines. Each file in the group consists of a set of profiles from the 1s-2p, 1s-3p, 1s-4p and 1s-5p transitions in the case of the hydrogen-like lines and $1s^2$-1s2p, $1s^2$-1s3p and $1s^2$-1s4p in the case of the helium-like lines. The relevant profile from each file was compared, in turn with the experimental profile, the ground state density - scale length product ($n_1\ell$) and the wavelength shift being varied to provide the best fit. In the single transition comparisons the fit was provided by area normalisation. This was the case for fits to a line series where only the n=3 and n=4 to n=1 lines and the singlet transitions of the n=2 to n=1 were used for comparison.

A typical fit is shown in Fig. 8.7 for the Ar XVII $1s^2$-1s3p transition. The Q value was 0.0103.

A plot of lines of best fits in n_e, n_1 space is shown in Fig. 8.8 for shot 131. Also represented in this graph is the maximum state of ionisation which is determined by requiring that the total number of hydrogenic (or helium-like ions) is never more than one half of the total number of atoms of the element (150) i.e.

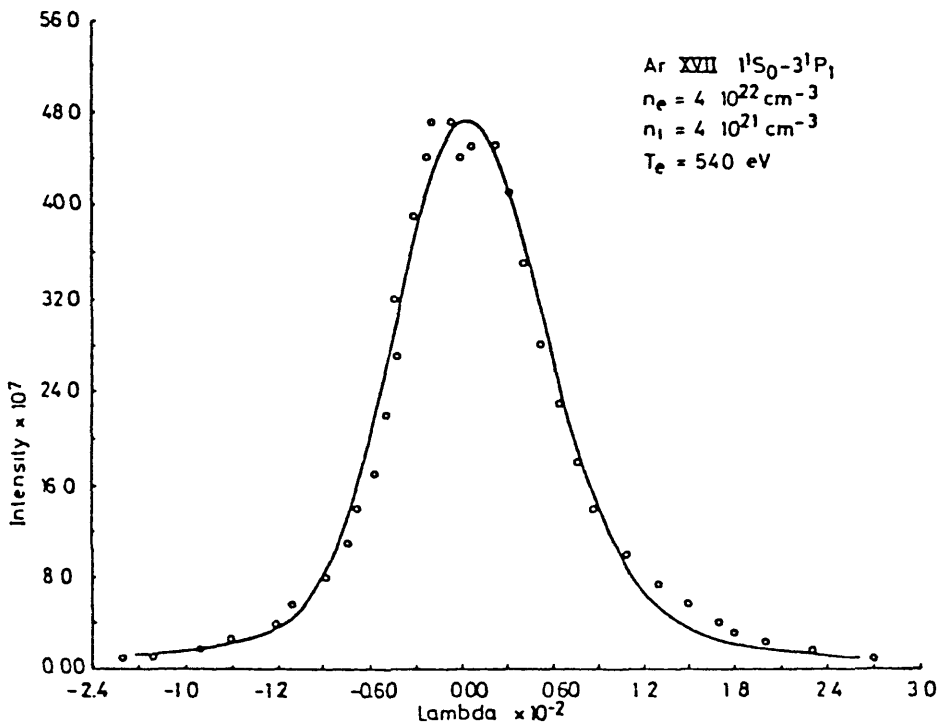


Fig. 8.7 A TYPICAL BEST FIT FOR THE Ar XVII $1s^2$–$1s3p$ TRANSITION

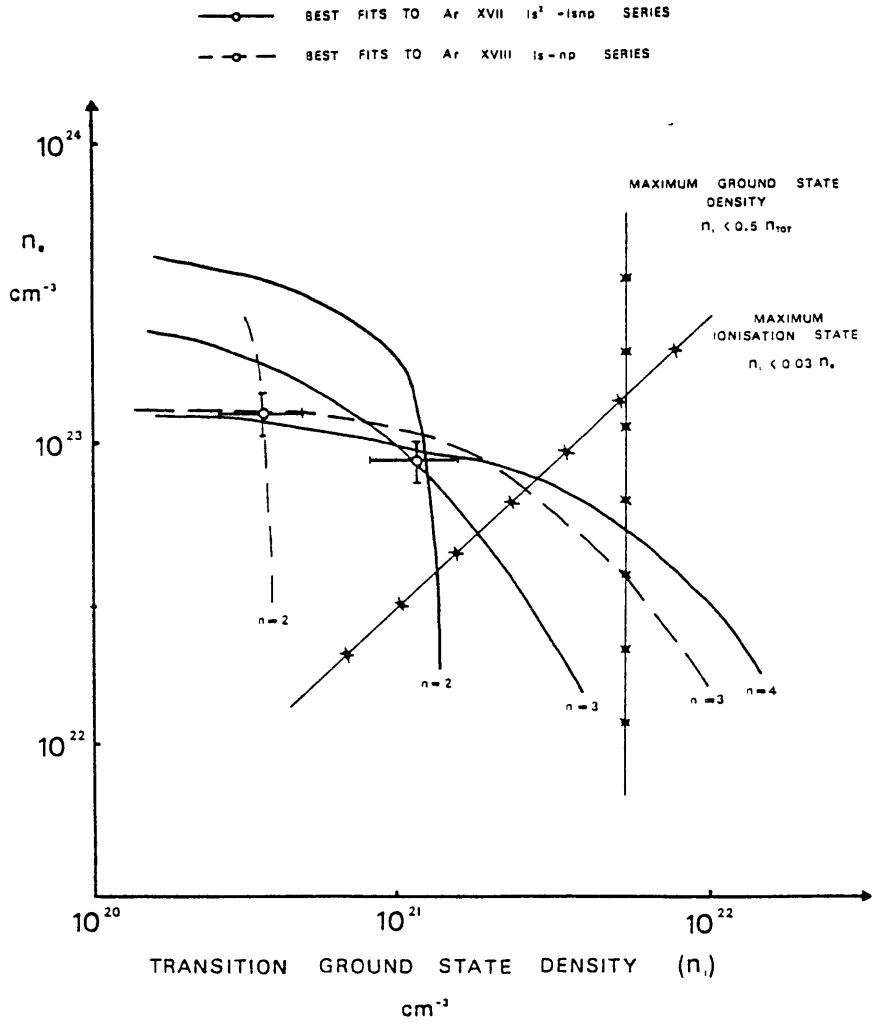


Fig. 8.8 LINES OF BEST FIT IN n_e, n_1 PARAMETER SPACE FOR SHOT 131

$$n_H < \frac{0.5\ n_e}{\overline{Z}}$$

where $\overline{Z}$ is the average charge.

A maximum value of ground state density can also be shown on the graph as determined by the total number of argon nucleii enclosed in the microballoon initially and the compression ratio as defined by the X-ray pinhole image. Using a similar criteria to above i.e. $n_H < 0.5\ n_{TOT}$ a better estimate of the upper bound can be obtained.

From Fig. 8.8 the values of n_e and n_1 predicted are 1.5×10^{23} cm^{-3} and 5×10^{21} cm^{-3} respectively.

8.3.2.2 SELF-CONSISTENT FIT TO THE Ar XVII $1s^2$-1s2p GROUP

A self-consistent fit was attempted using the interactive line fitting programs described earlier. Initially a fit was attempted at varying electron densities to the main line, the Ar XVII $1s^2\ ^1S_0$ - $1s2p\ ^1P_1$. This included the contribution of the Ar XVII $1s^2\ ^1S_0$ - $1s2s\ ^2S_0$ dipole forbidden component to the satellite on the long wavelength side of the singlet transition. A fit to the remainder of this satellite which consists of the spin forbidden Ar XVII $1s^2\ ^1S_0$ - $1s2p\ ^3P_1$ was attempted by using the optically thin doppler broadened profile of the Ar XVII $1s^2\ ^1S_0$ - $1s2p\ ^1P_1$ as an approximation to the triplet lineshape. The surrogate triplet profile was set up with its own ground state density and its intensity modified to take into account the change in transition probability as given by reference 151. This assumes that the collision rates are adequate to mix the singlet and triplet levels. The interactive routine enables these two profiles to be produced separately under differing conditions (in this case ground state density and electron density) and then be added together so that the whole profile can be compared with the experimental one. Using a profile at the same electron density for both transitions and varying the ground state density independently of each other to get the best fit of the whole profile, the actual ground state density can be found.

This is equivalent to emission from a single slab as the opacity of the slab emitting the triplet line to the singlet line being transmitted though it is very small.

At each electron density of the theoretical profiles, the ground state densities of the singlet and triplet transitions are adjusted to give the best fit. The ground state density of the singlet line was set to give an acceptable fit of the singlet profile only, fitting was done using scaling to the peak of the experimental intensity and adjusting the ground state density to achieve the correct line width. The shifted profile for the triplet transition was then added in at a first guess for the ground state density. Being optically thin this intensity will vary in direct proportion to the ground state density (N.B. being optically thick the intensity of the singlet decreases exponentially with increasing ground state density). Inclusion of the triplet slab will alter the required intensity of the singlet transition as the triplet line wings under-lie it. Alterations of the singlet intensity will alter its own line shape and also the 'dipole' forbidden contribution to the satellite blend. The process is thus 'iterative' and the interactive routine is needed for a self-consistent fit of this line group. As the fit is improved it is possible to move from a simple proportional scaling of the intensities to the area normalisation as used for the other line profiles in the series.

This fitting method was applied to the Ar XVII $1s^2$ - 1s2p line group on shot 131 (see Fig- 8.9) and the result compared favourably with the series fit, being $n_e \sim 2 \times 10^{23}$ cm^{-3} and $n_1 \sim 7 \times 10^{20}$ cm^{-3}. These are also plotted in Fig. 8.8.

8.3.2.3 DIELECTRONIC SATELLITE RATIO

Doubly excited ionic levels are populated by a number of atomic processes. The helium-like $2\ell2\ell'$ are populated by dielectronic capture (see Chapter 6) from the hydrogenic ground

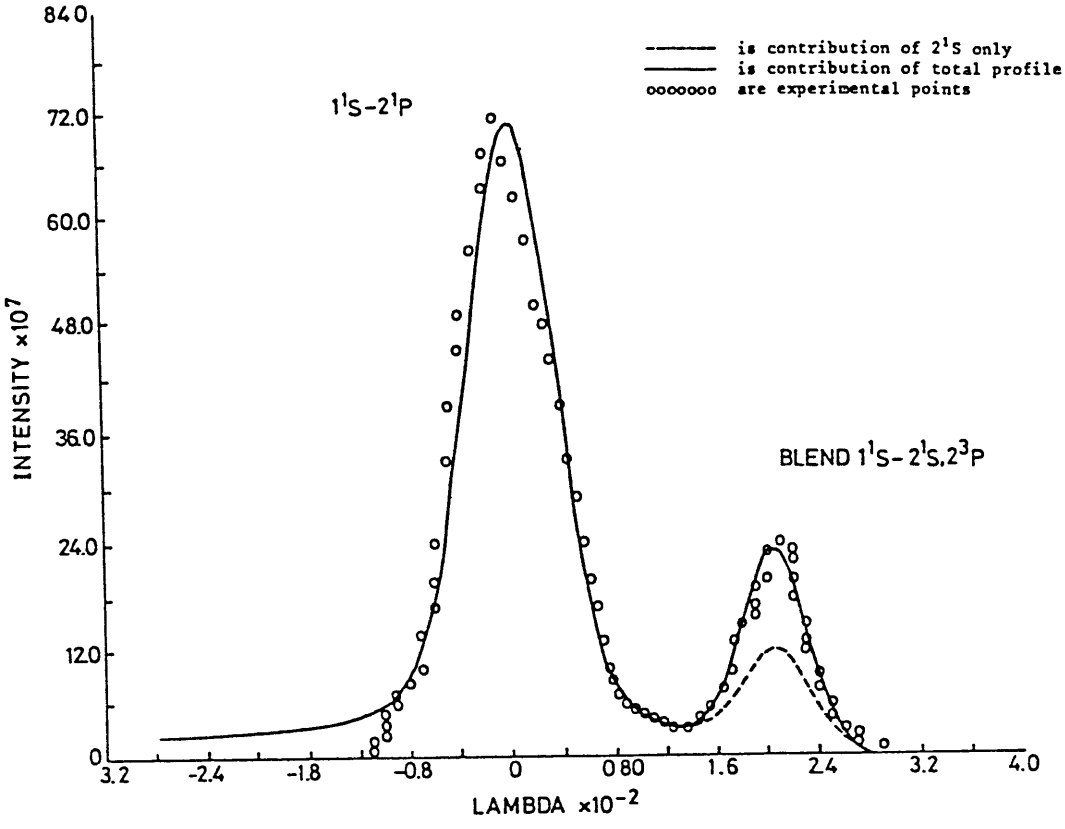


Fig. 8.9 DIAGNOSIS OF THE Ar XVII 1^1S_0-2^1P_1, 2^1S_0-2^3P_1, 1^1S_0-2^1S_0 BLEND IN SHOT 131

state. The dominant population mechanism for the helium-like $2p^2\ ^3P$ levels is inner shell excitations from the $1s2p^3P$ metastable level (152). At high electron densities collisional excitations from the $2\ell2\ell'$ levels is important and provides an electron density diagnostic.

Lunney and Seely (153) have shown that in the case of argon for the regions of temperature and electron density encountered in these experiments the dominant population mechanism for the Ar XVII $2s2p^3P$ and $2p^2\ ^3P$ levels is the inner shell excitations from the $1s2s\ ^3S$ and $1s2p\ ^3P$ metastable levels and that this ionisation stage is undergoing transient ionsation (154).

Figure 8.10 shows the Ar XVIII 1s-2p resonance line and its

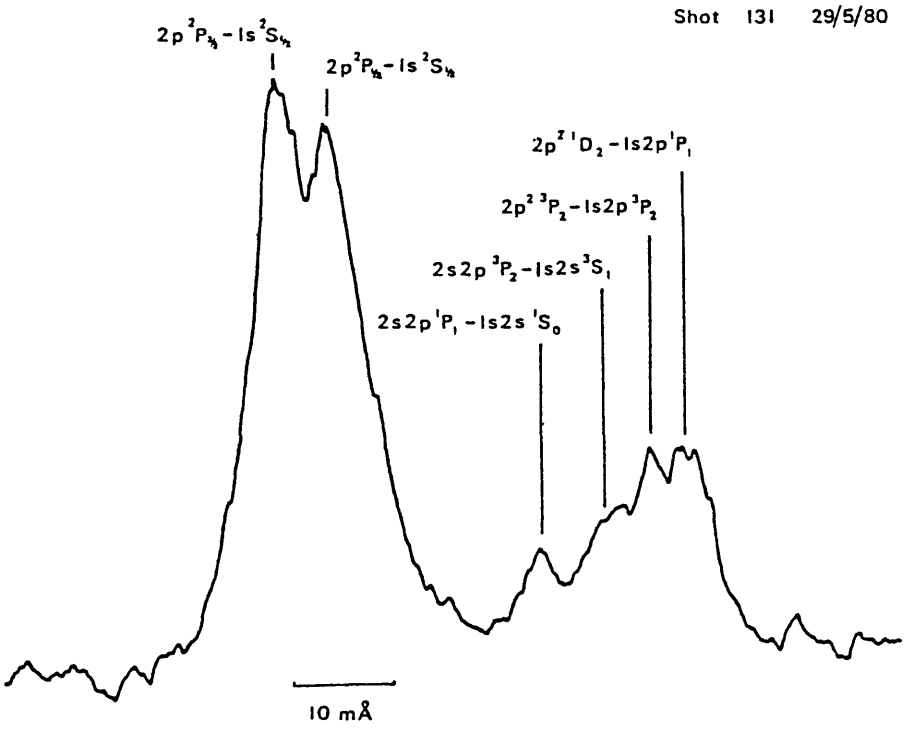


Fig. 8.10 DENSITOMETER TRACE OF THE Ar XVIII 1s-2p RESONANCE LINE AND SATELLITES

associated satellites taken from shot 131. Lunney and Seely (153) provided a graph (Fig. 8.11) which relates the electron density and the ratio of intensities of the main triplet lines to the main singlet lines in the group. The lines are identified in Fig. 8.10 and the intensity ratio from the experimental shots is shown in Fig. 8.11. This indicates an electron density of 2×10^{23} cm^{-3} only for a value of N_M/N_H of ~0.3 where N_M is the total populations of the $1s2s^3S$ and $1s2s^3P$ levels and N_H is the population of the hydrogenic ground state. For no inner shell excitation the value of electron density needed to achieve this satellite ratio is about 10 times higher.

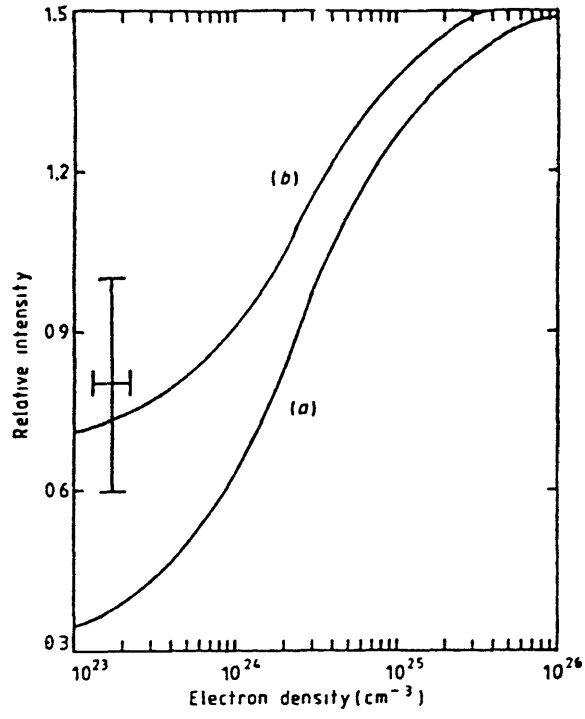


Fig. 8.11 INTENSITY RATIO OF THE TRIPLET TO SINGLET DIELECTRONIC SATELLITES SPECTRALLY ADJACENT TO THE Ar XVIII 1s-2p TRANSITION (153)
(a) WITHOUT INNER-SHELL EXCITATION
(b) WITH INNER-SHELL EXCITATION (N_M/N_H = 0.25)
THE MEASURED EXPERIMENTAL VALUE FROM SHOT 131 IS ALSO INDICATED

8.4 COMPARISON WITH IONISATION MODEL

The spectral series recorded from shot 131 also shows, apart from the helium-like series, the two highest members of the hydrogen-like series, the Ar XVIII 1s-2p and Ar XVIII 1s-3p lines (see Fig. 8.4). Although determination of the 1s-3p line was difficult as it was of low intensity and combined with the Ar XVII $1s^2$-1s5p it was possible to achieve an approximate determination of the electron density and ground state density of the hydrogen-like ions using the self-consistent line fitting method on the 1s-2p and its associated satellites. This gave 5×10^{20} cm^{-3} for the ground state density. The electron density was found to be approximately the same as the value determined for the helium-like series.

Using these figures a comparison can be made with a collisional radiative model (see Chapter 6), pertaining to this plasma regime, predicting the ratio of densities of a number of ions and then excited states and electron density.

R.W. Lee has developed a computer program (run on the ICCC 6800) (129) to predict the population densities of given ions under specified conditions. It includes transitions to and from six auto-ionising levels in the helium-like ion and all of the ground states of various ionic states and the excited levels of the hydrogenic and helium-like ions. This program uses mainly rate equations for the population of levels but reverts to Saha equilibrium (LTE) where the electron collisions in the higher energy states are dominant (see Chapter 6). It iterates over all states until an equilibrium is established and a convergence of electron density occurs when a self-consistent evaluation of the population is established.

Values obtained from this program for the specific case of argon at 500 eV and an electron density of 10^{23} cm^{-3} are 3×10^{20} cm^{-3} and 8×10^{20} cm^{-3} for the ground state densities of the hydrogen-like and helium-like series respectively. This shows consistency between the various experimental measurements and the computer model based on collisional radiative theory.

8.5 CONCLUSIONS

This chapter presents the analysis of a set of argon spectra from the core of an imploded glass microballoon. From these spectra values have been obtained for the electron temperature, electron density and ground state densities of the hydrogen-like and helium-like ions. These have been found to agree with theoretical calculations.

To use the dielectronic satellite ratio as a density diagnostic the degree of inner shell excitation must be taken into account.

REFERENCES

1. A.L. SCHAWLOW, C.H. TOWNES; Infrared and Optical Masers, Phys Rev 112 (6) 1940-9 (Dec. 1958).

2. N.G. BASOV, O.N. KROKHIN; The Conditions of Plasma Heating by the Optical Generator Radiation, 3rd Quantum Electronics Conference, Paris (1963). Ed. N. Bloembergen, P. Grivit, Columbia University. Press New York (1964).

3. N.G. BASOV, O.N. KROKHIN; Sov Phys JETP, 19 123 (1964).

4. J.M. NUCKOLLS, L.L. WOOD, A.R. THIESSEN, G.B. ZIMMERMAN; Laser Compression of Matter to Super High Densities: Thermonuclear (CTR) Applications, Nature 239 (5368) 139-192 (Sept. 1972).

5. K.A. BRUECKNER, S. JORNA; Laser Driven Fusion, Rev Mod Phys, 46 325 (1974).

6. J.L. EMMETT, J.H. NUCKOLLS, L.L. WOOD; Fusion Power by Laser Implosion, Sci Am 24-37 (June 1974).

7. S.W. MEAD, R.E. KIDDER, J.E. SWAIN, F. RAINER, J. PETRUZZI; Appl Optics 11 (2) 345 (1972).

8. D.J. NAGEL, P.G. BURKHALTER, C.M. DOZIER, J.F. HOLTZRICHTER, B.M. KLIEN, J.M. McMAHON, J.A. STAMPER, R.R. WHITLOCK; Phys Rev Lett 33 (13) 743 (1974).

9. P.J. MALLOZZI, H.M. EPSTEIN, R.G. JUNG, D.C. APPLEBAUM, B.P. FAIRLAND, W.J. GALLAGHER; J Appl Phys 45 (4) (1974).

10. K. EIDMANN, M.H. KEY, R. SIGEL; J Appl Phys 6 2402 (1976).

11. V.A. BOIKO, A.Ya. FAENOV, S.A. PIKUZ; J. Quant Spectroc Radiat Transfer 19 11 (1978).

12. R.W. WAYANT, R.C. ELTON; Proc IEEE 64 (7) 1059 (1976).

13. G.J. PERT; Phil Trans R.Soc London A (GB) 300 (1456) 631-40 (1981).

14. Rutherford Laboratory Annual Report to the Laser Facility Committee RL-81-040 (1981).

15. J.D. LAWSON; Some Criteria for a Power Producing Thermonuclear Reactor, Proc Phys Soc B70 6-10 (1957).

16. W.M. BENNETT; Phys Rev 45 890 (1934).

17. H.A. BODIN, A.A. NEWTON; Nucl Fusion 20 (10) 1255 (1980).

18. G.J. PERT; Inertial Confinement, Lectures to the Culham Plasma Physics Summer School, Volume 3 (1980).

19. D.L. BOOK; NRL Plasma Formulary.

20. F.J. McCLUNG, R.W. HELLWRATH; J. Appl Phys 33 828 (1962).

21. A.L. DEMARIA, W.H. GLENN, M.J. BRIENZA, M.E. MACK; Proc IEE 57 2 (1969).

22. A.E. SIEGMAN; An Introduction to Lasers and Masers, McGraw Hill, New York (1971).

23. A. YARIV; Quantum Electronics, John Wiley, New York (1967).

24. M.H. KEY; Lectures on the Physics of the Superdense Region, 20th Scottish Universities Summer School in Physics, Laser Plasma Interactions, St. Andrews 1979. SUSSP Publications Edinburgh (1980).

25. T.P. HUGHES; Plasmas and Laser Light, Adam Hilger, London (1975).

26. G.BEKEFI; Radiation Processes in Plasmas, John Wiley, New York (1966).

27. F.F. CHEN; Laser Interaction and Related Plasma Phenomena, 3 291, Plenum, New York (1974).

28. T. O'NEIL; Phys Fluids 8 2255 (1965).

29. W.L. KRUER, J.M. DAWSON; Phys Fluids 15 446 (1972).

30. W.M. MANHEIMER, H.H. KLEIN; Phys Fluids 18 1299 (1975).

31. J.M. DAWSON; Phys Rev 113 383 (1959).

32. J.M. DAWSON, P. KAW, B. GREEN; Phys Fluids 12 875 (1969).

33. T.P. HUGHES; Lectures on Laser Light in Plasmas, 20th Scottish Universities Summer School in Physics, Laser Plasma Interactions, St. Andrews 1979, SUSSP Publications, Edinburgh (1980).

34. M. BORNATICI et al; Enhanced Scattering and Anomalous Absorption of Light Due to Decay into Plasma Waves, Phys Fluids 12 2362-73 (1969).

35. M.V. GOLDMAN; Parametric Plasmon and Photon Interaction; I, Threshold for Amplification of Plasmons; II, Analysis of Plasmon Propagator and Correlation Functions, Ann. Phys 38 95-116, 117-69 (1966).

36. G.J. PERT; Plasma Phys 20 175 (1978).

37. V.L. GINSBURG; The Propagation of Electromagnetic Waves in Plasmas, 2nd Ed., Pergammon Oxford (1970).

38. L. SPITZER, R. HARM; Phys Rev 89 977 (1953).

39. L. SPITZER; Physics of Fully Ionised Gases, Interscience, New York (1956).

40. R.C. MALONE, R.L. McCRORY, R.L. MORSE; Phys Rev Lett 34 (12) 721 (1975).

41. W.M. MANHEIMER; Phys Fluids 20 265 (1977).

42. D.W. FORSLAND, J.M. KINDEL, K.LEE; Phys Rev Lett 39 284 (1977).

43. K.ESTABROOK, W.L. KRUER; Phys Rev Lett 40 (1) 42 (1978).

44. M.G. HAINES; Lectures on the Coronal Region, 20th Scottish Universities Summer School in Physics, Laser Plasma Interactions, St. Andrews 1979, SUSSP Publications Edinburgh (1980).

45. P. MULSER; Lectures on Radiation Transport, 20th Scottish Universities Summer School in Physics, Laser Plasma Interactions, St. Andrews 1979, SUSSP Publications Edinburgh (1980).

46. K.A. BRUECKNER; Phys Rev Lett 36 677 (1976) and Nucl Fusion 17 1257 (1977).

47. J.D. HARES, J.D. KILKENNY, M.H. KEY, J.G. LUNNEY; Phys Rev Lett 42 1216 (1979).

48. C. FAUQUINON, F. FLOUX; Phys Fluids 13 386 (1970).

49. M.PUELL; Z. Naturf 25A 1807 (1970).

50. O.N. KROKHIN; Sov Phys Tech Phys 9 1024 (1965).

51. R.E. KIDDER; Nucl Fusion 8 3 (1968).

52. A. CARUSO, R. GRATTON; Plasma Phys 10 867 (1968).

53. R.S. COOPER; AIAA Journal 11 831 (1973).

54. N.G. BASOV, V.A. GRIBKOV, O.N. KROKHIN, G.V. SKLIZKOV; Sov Phys JETP 27 575 (1968).

55. T.P. DONALDSON, R.J. HUTCHEON, M.H. KEY; J Phys B 6 1525 (1973).

56. C.E. MAX, C.F. McKEE, W.C. MEAD; Phys Fluids 23 1620 (1980).

57. Ya.B. ZELDOVICH, Yu.P. RAIZER; Physics of Shock Waves and High Temperature Hydrodynamic Phenomena, Vols. I and II, Academic Press, New York (1967).

58. L.McCARTHY; Lawrence Livermore Laboratory Report No. UCRL 14364 (1965).

59. J.M. WALSH, M.H. RICE, Z.G. McQUEEN, F.L. YORGER; Phys Rev 108 196 (1957).

60. B.I. BENNETT, J.D. JOHNSON, G.I. KERLEY, G.T. ROOD; Los Alamos Laboratory Report No. LA 7130 VC34 (1978).

61. S.E. BODNER et al; Paper IAEA CM 37-B-3 Proc IAEA Conference on Plasma Physics and Controlled Fusion Research, Innsbruck (1978).

62. E.K. STORM, J.J. LARSEN, J.M. NUCKOLLS, H.G. AHLSTROM, K.R. MANES; Lawrence Livermore Laboratory Report No. UCRL 79788 (1977).

63. M.D. ROSEN, J.M. NUCKOLLS; Lawrence Livermore Laboratory Report No. UCRL 81343 (1977).

64. B. AHLBORN, M.H. KEY; Rutherford Laboratory Report No. RL-79-033 (1978).

65. P.M. CAMPBELL, G. CHARATIS, G.R. MONTRY; Phys Rev Lett 34 74 (1975).

66. V.W. SLIVINSKY, H.G. AHLSTROM, K.G. TIRSELL, J.LARSEN, S. GLAROS, G. ZIMMERMAN, H. SHAY; Phys Rev Lett 35 1083 (1975).

67. G.M. McCALL, F. YOUNG, A.W. EHLER, J.F. KEPHART, R.P. GODWIN; Phys Rev Lett 30 1116 (1973).

68. W.W. SIMMONS, D.R. SPECK, J.T. HUNT; Argus Laser System: Performance Summary, Appl. Optics 17 999 (1978).

69. R.R. JOHNSON, F.J. MAYER; 1977 Annual Report on Laser Fusion Research, K.M.S. Fusion Inc (1978).

70. K.B. MITCHELL, D.B. VAN HUSTEYN, G.M. McCALL, P. LEE; Phys Rev Lett 42 232 (1979).

71. R.R. JOHNSON; Bull Am Phys Soc 22 84 (1977).

72. Rutherford Laboratory Laser Division Annual Report to the Laser Facility Committee RL-79-036 (1979).

73. B. YAAKOBI, D. STEEL, E. THORSOS, A. HAUER, B. PERRY; Phys Rev Lett 39 1526 (1977).

74. M.H. KEY, C.L.S. LEWIS, J.G. LUNNEY, A. MOORE, T.A. HALL, R.G. EVANS; Phys Rev Lett 41 1467 (1978).

75. R.L. BERGER et al; Proc 7th Int. Conf. on Plasma Physics and Controlled Nucl. Fusion Research IAEA CM37-B-2 (1978).

76. R.A. LERCHE; LLL Report No. UCRL 50021-76 (1977).

77. J.M. NUCKOLLS, R.O. BANGERTER, J.D. LINDL, W.C. MEAD, Y.L. PAN; LLL Report No. UCRL 50021-77 2 4-12 (1978).

78. R.E. KIDDER; Nucl. Fusion 16 3 (1976).

79. D.E.T.F. ASHBY; Nucl. Fusion 16 231 (1976).

80. S.W. GREGG, S.J. THOMAS; J. Appl. Phys 37 2787 (1966).

81. S. ZWEIGENBAUM, Y. GAZIT, Y. KOMET; Plasma Phys 19 1305 (1977).

82. P.T. RUMSBY, M. MICHAELIS, M. BURGESS; Opt Comm 15 422 (1975).

83. Naval Research Laboratory; NRL Memorandum Report No. 3890 (1978).

84. C.G.M. VAN KESSEL, R. SIGEL; Laser Interaction and Related Plasma Phenomena, Eds. H.J. Schwartz, H. Hora 3B 547 Plenum (1976).

85. C.G.M. VAN KESSEL, R. SIGEL; Phys Rev Lett 33 1020 (1974).

86. M. GALANTI, N.J. PEACOCK; J. Phys B 8 2427 (1975).

87. M.H. KEY et al; Rutherford Laboratory Report No. RL-78-020 (1978).

88. M.H. KEY, J.G. LUNNEY, J.M. WARD, R.G. EVANS, P.T. RUMSBY; J. Phys B 12 L213 (1979).

89. Yu.A. ZAKHARENKOV, N.N. ZOREV et al; Zh. Ekst Teor Fiz 70 557 (1976).

90. D. PHILLION et al; Laser Interaction and Related Plasma Phenomena, Eds. H.J. Schwartz, H. Hora 4B 503 Plenum (1977).

91. J.D. HARES; Ph.D Thesis, Imperial College London (1981).

92. F.C. YOUNG, R.R. WHITLOCK, R. DECOSTE, B.H. RIPIN, D.J. NAGEL, J.A. STAMPER, J.M. McMAHON, S.E. BODNER; Appl. Phys Lett 30 45 (1977).

93. B.H. RIPIN, R. DECOSTE, S.P. OBENSCHAIN, S.E. BODNER, E.A. McCLEAN, F.C. YOUNG, R.R. WHITLOCK, C.M. ARMSTRONG, J. GRUN, J.A. STAMPER, S.H. GOLD, D.J. NAGEL, R.H. LEHMBERG, J.M. McMAHON; Phys Fluids 23 1012 (1980).

94. B. YAAKOBI, T.C. BRISTOW; Phys Rev Lett 38 350 (1977).

95. B.I. COHEN, C.E. MAX; Phys Fluids 22 1115 (1979).

96. J. MURDOCH, J.D. KILKENNY, D.R. GRAY, W. TONER; Phys Fluids 24 2107 (1981).

97. D.J. NICHOLAS, J.E. BOON; J. Phys D Appl Phys 14 593 (1981).

98. A. YARIV; Introduction to Optical Electronics, 2nd Ed., Holt Reinhart Winston, New York (1976).

99. R.S. CRAXTON; Optics Comm 34 474 (1980).

100. W. SEKA, S.D. JACOBS, J.E. RIZZO, R. BONI, R.S. CRAXTON; Opt Comm 34 469 (1980).

101. M.W. KEY, C.L.S. LEWIS, J.G. LUNNEY, A. MOORE, J.M. WARD, R.K. THAREJA; Phys Rev Lett 44 1669 (1980).

102. M.C. HOBBY, N.J. PEACOCK; J. Phys E 6 184 (1973).

103. J.G. LUNNEY; Ph.D Thesis, Queens University of Belfast (1980).

104. H.R. GRIEM; Plasma Spectroscopy, McGraw Hill New York (1964).

105. T.J. GOLDSACK; Ph.D Thesis, Imperial College London (1982).

106. F. AMIRANOFF, R. BENATTAR, R. FABRO, E. FABRE, C. GARBAN, M. WEINFIELD; Bull Am Phys Soc 24 1054 (1979).

107. W.C. MEAD, E.M. CAMPBELL, K.G. ESTABROOK, R.E. TURNER, W.C. KRUER, P.H.Y. LEE, B.P. PRUETT, V.C. RUPERT, K.G. TIRSELL, G.L. STRADLING, F. ZE, C.E. MAX, M.D. ROSEN; Phys Rev Lett 47 1289 (1981).

108. M.D. ROSEN, D.W. PHILLION, V.C. RUPERT, W.C. MEAD, V.W. SLIVINSKI, G. CAPOROSO, M.J. BOYLE, K.G. TIRSELL; Phys Fluids 22 2020 (1979).

109. C.L.S. LEWIS, R.F. CUNNINGHAM, L. PINA, A.K. ROY, J.M. WARD; J. Phys D 15 69 (1982).

110. G. LEPPELMAIER; Laboratory for Laser Energetics Report No. LLE 087 (1979).

111. N.G. BASOV et al; IPPLM Reort No. 3780 (57), S. KALISKI; Institute of Plasma Physics and Laser Microfusion, Warsaw (1980).

112. T.J. GOLDSACK, J.D. KILKENNY, P.T. RUMSBY; J. Phys D Appl. Phys 14 147 (1981).

113. J. GRUN, R. DECOSTE, B.H. RIPIN, J. GARDNER; Appl. Phys Lett 39 545 (1981).

114. F. AMIRANOFF, K. EIDMANN, R. SIGEL, R. FEDOSEJEVES, A. MAASWINKEL, YUNG LU TENG, J.D. KILKENNY, J.D. HARES, D.K. BRADLEY, B.J. MacGOWAN, T.J. GOLDSACK; J. Phys D 15 2463 (1982).

115. S.G. GITOMER, D.B. HENDERSON; Phys Fluids 22 (2) 364-6 (1979).

116. B. YAAKOBI, T. BOCKLEY, P. BOURKE, Y. CONTURIE, R.S. CRAXTON, J. DELETTREZ, J.M. FORSYTH, R.D. FRANKEL, L.M. GOLDMAN, R.L. McRORY, M.C. RICHARDSON, W. SEKA, D. SCHWARTZ, J.M. SOURES; Opt Comm 39 176 (1981).

117. A.P. THORNE; Spectrophysics, Chapman and Hall London (1974).

118. A.H. GABRIEL, C. JORDAN; Case Studies in Atomic Collision Physics 2 209 Eds. E.W. McDaniel, M.R.C. McDowell, North Holland Amsterdam (1972).

119. R.W.P. McWHIRTER; Spectral Intensities, Plasma Diagnostic Techniques, Eds. R.H. Huddlestone, S.C. Leonard, Academic Press New York (1965).

120. H. MARGENAU, M. LEWIS; Rev Mod Phys 31 569 (1959).

121. B.P. DUCLOS, A.B. CAMPBELL; Z. Naturf 16A 711 (1961).

122. G. ECKER, W. KROLL; Phys Fluids 8 354 (1965).

123. H.R. GRIEM; Phys Rev 131 (3) 1170 (1963).

124. C. JORDAN; Mon Not R. Astr. Soc. 142 501 (1969).

125. L.L. HOUSE; Astrophys J. Supp. Ser. 8 307 (1964).

126. D.R. BATES, A.E. KINGSTON, R.W.P. McWHIRTER; Proc Roy Soc A 267 (1130) 297 (1962).

127. D.R. BATES, A.E. KINGSTON, R.W.P. McWHIRTER; Proc Roy Soc A 270 (1341) 155 (1962).

128. H.P. SUMMERS; Mon Not R. Astr. Soc. 169 663 (1974).

129. R.W. LEE; Imperial College London, Unpublished.

130. A.V. VINOGRADOV, I.Yu. SKOBELEV, E.A. YUKOV; Sov. J. Plasma Phys (1977), (Fiz Plasmu USSR 3 (3) 686 (1977)).

131. A.V. VINOGRADOV, I.Yu. SKOBELEV, E.A. YUKOV; Sov. J. Quant Electron 5 (6) 630 (1975).

132. J.F. SEELY; Atomic Data and Nuclear Data Tables 26 137 (1981).

133. S.G. RAUTIN, T.T. SOBEL'MAN; Sov. Phys Uspekhi 9 (5) 701 (1967).

134. W. LOCHTE-HOLTGREVEN (Ed.); Plasma Diagnostics, North Holland Amsterdam (1968).

135. S.L. MANDELSHTAM, P.P.RASKININ, A.M. PROKHOROV, Yu.P. RAIZER, N.K. SUKHODREV; Sov. Phys JETP 22 91 (1966).

136. F.C. JOHODA, E.M. LITTLE, W.E. QUINN, G.A. SAWYER, T.F. STRATTON; Phys Rev 119 843 (1960).

137. B.V. ROBOUCH, J.P. RAGER; Appl. Phys 44 1527 (1973).

138. D.D. BURGESS, B.C. FAWCETT, N.J. PEACOCK; Proc. Phys Soc 92 805 (1967).

139. V.A. BOIKO, S.A. PIKUZ, A.Ya. FAENOV; Sov. J. Quant Elect. 5 658 (1975).

140. N.J. PEACOCK; Diagnostics Based on Electromagnetic Radiation, 20th Scottish Universities Summer School in Physics, Laser Plasma Interactions, St. Andrews 1979, SUSSP Publications Edinburgh (1980).

141. R.W. JAMES; The Optical Principles of Diffraction of X-rays, G. Bell and Sons (1948).

142. A.E. SANDSTROM; Experimental Methods of X-ray Spectroscopy, Handbuch der Physik 30 78, Ed. S. Fugge, Springer (1957).

143. M. De BROGLIE, E.A. LINDMAN; Compt Rend 158 944 (1914).

144. Rutherford Laboratory Laser Division Annual Report to the Laser Facility Committee RL-80-026 (1980).

145. K. EVANS, M. LEWIS; Report No. BDF/OCR 110, CLF, Rutherford Laboratory Contract No. N2B/29582/RL (1977).

146. R.W. LEE; J Phys B 12 1129 (1979).

147. R.W. LEE; J Phys B 12 1145 (1979).

148. R.W. LEE; Phys Lett 71A 224 (1979).

149. P.C. KEPPLE* H.R. GRIEM; NRL Memo No. 3382, Naval Research Labs. Washington DC (1976).

150. J.D. KILKENNY, R.W. LEE, M.H. KEY, J.G. LUNNEY; Phys Rev A 22 2746 (1980).

151. L.A. VAINSHTEIN, U.I. SAFRONOVA; Atomic Data and Nuclear Data Tables 21 (1) (1978).

152. V. FELDMAN, G.A. DOSCHEK, D.J. NAGEL, R.D. COWAN, R.R. WHITLOCK; Astrophys J 192 213 (1974).

153. J.G. LUNNEY, J.F. SEELY; J Phys B 15 (3) L121 (1982).

154. C.P. BHALLA, A.H. GABRIEL, L.P. PRAESNYAKOV; Mon Not R. Astr. Soc. 172 359 (1975).

ACKNOWLEDGEMENTS

I gratefully acknowledge the help of the following: my supervisor Dr. J.D. Kilkenny for all his help, guidance and encouragement; the members of the Plasma Physics Groups at Imperial College, London and Queens University, Belfast, for their help and collaboration; Dr. R.W. Lee, Imperial College, London, for use of his computer models and line broadening calculations; the staff of the Laser Division, Rutherford Laboratory, for all their technical assistance; Professor M.G. Haines for the provision of computing budgets; the Science and Research Council for financial support and provision of the Central Laser Facility at the Rutherford Laboratory; Mrs. Margaret McCoubrie for the typing; EASAMS Limited for use of facilities in their Technical Publications Department and help in production; and finally all my family and friends for their help and support, especially Anne Bell who helped with the proof-reading and diagrams.